BILINGUAL PUBLISHING CO.
Pioneer of Global Academics Since 1984

02

Hydro Science & Marine Engineering

Volume 2 | Issue 2 | 2020 October | ISSN 2661-331X (Online)

Volume 2 Issue 2 • October 2020 • ISSN 2661-331X (Online)

Hydro Science & Marine Engineering

BILINGUAL PUBLISHING CO.

Pioneer of Global Academics Since 1984

BILINGUAL PUBLISHING CO.
Pioneer of Global Academics Since 1984

Volume 2 | Issue 2 | October 2020 | Page 1-49
Hydro Science & Marine Engineering

Contents

Article

Review

BILINGUAL PUBLISHING CO.
Pioneer of Global Academics Since 1984

Hydro Science & Marine Engineering
https://ojs.bilpublishing.com/index.php/hsme

ARTICLE

Progressive Collapse Resistance Analysis of Secondary Shielding Installation Platform for A-type Tank

Qingfeng Wang Zhigang Miao Li Zhou*

School of Naval Architecture and Ocean Engineering, Jiangsu University of Science and Technology, Zhenjiang, 212003, China

ARTICLE INFO

Article history
Received: 7 February 2020
Accepted: 18 February 2020
Published Online: 30 October 2020

Keywords:
A-type tank
Installation platform
Progressive collapse

ABSTRACT

As a key supporting equipment for the construction of LNG carriers, the installation platform undertakes the support and guarantee of LNG carrier tank internal construction. This paper takes the secondary shielding installation platform of A-type tank as the object of study, the study firstly considers the semi-rigidity of the nodes and the material nonlinearity based on finite element software, and then the residual structure is calculated using static nonlinear method after single truss, two trusses and three trusses are invalid simultaneously. The research results show that the truss with higher components importance coefficient has greater impact on the residual structure when the truss is invalid; After the 2 trusses of installation platform become invalid completely, the further progressive collapse will not occur; When A1-HJ, A2-HJ and A2-HJ are dismantled at the same time, it will lead to the local progressive damage, which can cause the collapse of large-scale structures. The research findings can support the design and use of the installation platform.

1. Introduction

Progressive collapse refers to the local failure of structures under unconventional loads, including explosive explosion, gas explosion, vehicle impact and heavy impact. This damage expands and eventually leads to the collapse of the whole building or causes collapse out of proportion to the initial damage. Since the collapse of Ronan Point in 1968, progressive collapse has attracted the attention of designers at home and broad firstly. Taewam Kim and Jinkoo Kim [1] had analyzed the influencing factors of continuous collapse resistance of steel frame structures, the results show that: The risk of progressive collapse of steel frame structure increases with the decrease of floor number and the increase of beam span; Increasing the span number can significantly improve the anti-progressive collapse performance of the structure; With the increase of design seismic force, the anti-progressive collapse ability of the structure also increases. Hu Xiaobin [2] adopted finite element program LS-DYNA to complete progressive collapse simulation analysis of Multilayer Planar Steel Frame, the results show that: For steel structures, increasing failure strain of materials can improve their ability to resist progressive collapse. Xie Buying described the whole process of frame failure until it completely collapses on the ground by using the concept of Inertia, the relationship between force and acceleration and the principle of collision dy-

**Corresponding Author:*
Li Zhou,
School of Naval Architecture and Ocean Engineering, Jiangsu University of Science and Technology, Zhenjiang, 212003, China;
Email: zhouli209@hotmail.com

 DOI: https://doi.org/10.30564/hsme.v2i2.1691

namically. In addition, the general commercial software is used to carry out numerical simulation analysis of the structure in order to give some damage mechanisms or anti-collapse measures.

Secondary shielding installation platform for A-type tank is the new and lightweight scaffold which is used to support the installation engineering of the secondary shield. It is composed of several steel frames connected by connecting beams, and each steel frame is composed of trusses and suspension structures fixed by connecting with hull. At present, hanging structures are mostly used in high-rise buildings. It is it is seldom that large scaffolding construction uses hanging structures. It is difficult to judge whether the remaining structures will collapse continuously once the truss is damaged or invalidated in the installation platform structure. For the installation platform, the progressive collapse of the structure will cause extensive damage to the secondary shield and serious casualties, resulting in incalculable losses. Therefore, the analysis of its anti-progressive collapse has important engineering significance.

2. Analysis Model

2.1 Model Unit Selection

At present, the finite element method is usually used to simulate the progressive collapse process of structures, the accuracy of the analysis model has a great influence on the evaluation results of progressive collapse. The secondary barrier installation platform of A-type tank is mainly composed of frame, connecting beam and expansion beam [3]. The structures are connected with each other by linking pins for EC fasteners. From the point of view of connection mode, the installation platform is a hybrid connection mode. The components of the installation platform, such as the expansion beam structure and the connection beam, are connected by EC fasteners. The connection mode between the components is welding [4]. The internal nodes of components can be simulated by common nodes in finite element calculation, while the EC fastener connections between components can be considered as semi-rigid connections [5]. In the process of modeling using ANSYS Workbench, this paper simulates the connection of nodes between components by spring element, and simulates semi-rigidity of nodes by inserting three-direction non-linear rotating spring [6]. According to *Technical Specification for Safety of Portal Steel Tube Scaffold in Construction* (JGJ128-2000161), the tightening torque of fastener bolts should be 50-60 N.m, and not less than 40 N.m. Therefore, the initial stiffness of fastener connection is taken in the analysis of this chapter when the tightening moment is 60 N. M. The initial stiffness of the joint is 71.27 kN·M/rad at the connection of EC fasteners of the main components based on the research of Luzheng of Zhejiang University.

2.2 Components of Installation Platform

The trapezoidal truss of the installation platform is made of H-section steel with 23 longitudinal sections and 8 transverse sections. Hollow square tubes are used for hanging frames and connecting components. The type of steel used in the structure is Q235B, and the related parameters of the installation platform components are shown in Table 1.

Table 1. Section specification of installation platform

number	Sectional specification	Cross section area/mm^2	Plastic modulus of section/ mm^3	Plastic flexural capacity/ kN·m	Shear ultimate bearing capacity/kN
1	139×139×10×7	3613	98057.7	23	187.4
2	67×67×3	768	18445.5	4.34	172.8
3	52×52×2	400	7504	1.76	90.0
4	58×58×3	660	13626	3.20	148.5
5	37×37×2	280	3679	0.86	63.0
6	46×46×3	516	8127	1.91	116.1
7	90×48×4	1952	19040	4.47	439.2
8	41×41×2	312	4567	1.07	70.2
9	57×57×3	648	13135.5	3.09	145.8

2.3 Component Importance Evaluation

The installation platform belongs to large steel structure. If the whole structure is dismantled one by one to calculate the importance coefficient of each truss, the workload will be enormous [7]. Platform structure is symmetrical in the direction of captain, so only one half of the model of installation platform is used to evaluate the importance of truss. The steel frames of each truss are divided into three areas: A, B and C. The number of each steel frame is shown in Figure 1.

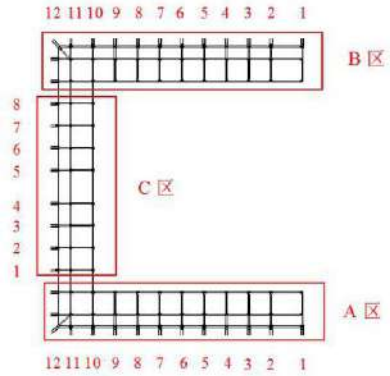

Figure 1. Frame number of Installation platform

For non-frame structures, it is necessary for designers

DOI: https://doi.org/10.30564/hsme.v2i2.1691

to evaluate the importance of components [8]. According to the relevant research results, the main methods of evaluating the importance of components are based stiffness-based, energy-based and strength-based [9]. In this paper, energy-based judgment method is used to evaluate the importance of components, calculate the importance coefficients of each truss, and ultimately determine the key truss. The importance coefficients of each truss are shown in Table 2.

2.4 The Number of Structure

In order to facilitate the follow-up analysis, the members of each steel frame are numbered in the form of steel frame number-member+layer number. For example, the fifth suspender of A1 frame is expressed as A1-DG5, and the fifth walkway beam of A1 frame is expressed as A1-ZD5.The connecting beams between the two frames are numbered in the form of steel frame number-steel frame number-connecting beams+layers. For example, the corridor connecting beams between A1 steel frame and A2 steel frame are named A1-A2-ZDLJ1, A1-A2-ZDLJ2, A1-A2-ZDLJ3, A1-A2-ZDLJ4, A1-A2-ZDLJ5 according to the number of layers. The fifth floor frame connecting beam between A1 steel frame and A2 steel frame near the aisle is named A1-A2-KJLJ5a, and the other side is named A1-A2-KJLJ5b. Since the installation platform is a plane symmetrical structure about A1 steel frame, the A2 steel frame about A1 steel frame is named A-2', and the other components are the same.

3. Analysis of Calculation Results

3.1 Structural Response to Failure of a Truss

3.1.1 Demolition of Truss A1-HJ

After removing the truss A1-HJ, the response of the structure is shown in Figure 2. It can be seen from the Figure that the maximum displacement of the surrounding structure after removing the truss is 29.9 mm (Figure (a)).The axial force of the suspender is greater than other tension members in the same steel frame. Therefore, the suspender is selected to judge the failure of the tension members. The maximum axial force of the adjacent suspender is A2'-DG5, and the axial stress is 122 MPa (Figure (b)).Through the analysis of the axial force of the members connected with the truss, it is found that the suspender in the expansion beam area has relatively large axial force among the steel frames. The failure judgment of A2 steel frame and A2 steel frame suspender in adjacent area of failure truss is made. As shown in Table 3, it shows that the progressive collapse of residual structure will not occur after A1-HJ is completely removed. The maximum shear force of beam section is 60.1kN at the connection of A2 truss and suspender (Figure (c)), which does not reach the failure limit of section. The results show that the shear force of the corridor connection beam is larger than that of the frame connection beam, and the shear ultimate bearing capacity of the section of the corridor connection beam is smaller than that of the frame connection beam. Therefore, the shear failure of the corridor connection beam is judged, as shown in Table 4.The plastic bending capacity of the frame linking beams connected with the dismantled truss is 1.91 kN m, and that of the walkway connection beams is 1.07 kN M. As shown in the bending moment diagram of Figure (d), the maximum bending moment of each connection beam is 1.02 kN m, and the section does not enter the plasticity, so there will be no plastic hinges. The maximum stress of the structure appears at the junction of A2_-HJ and A2_-DG5 (Figure (e)), and the maximum stress is 235.4 MPa.

Table 2. Important coefficient of trusses

Number of removed component	A1-HJ	A2-HJ	A3-HJ	A4-HJ	A5-HJ	A6-HJ	A7-HJ	A8-HJ
Coefficient of importance	0.1846	0.1057	0.0849	0.0839	0.0839	0.0839	0.0839	0.0832
Number of removed component	A9-HJ	A10-HJ	A11-HJ	A12-HJ	B1-HJ	B2-HJ	B3-HJ	B4-HJ
Coefficient of importance	0.0804	0.0784	0.1167	0.1174	0.1846	0.1057	0.0849	0.0839
Number of removed component	B5-HJ	B6-HJ	B7-HJ	B8-HJ	B9-HJ	B10-HJ	B11-HJ	B12-HJ
Coefficient of importance	0.0839	0.0839	0.0839	0.0832	0.0804	0.0784	0.1167	0.1174
Number of removed component	C1-HJ	C2-HJ	C3-HJ	C4-HJ	C5-HJ	C6-HJ	C7-HJ	C8-HJ
Coefficient of importance	0.0977	0.0813	0.0832	0.1267	0.1267	0.0826	0.0813	0.0977

 DOI: https://doi.org/10.30564/hsme.v2i2.1691

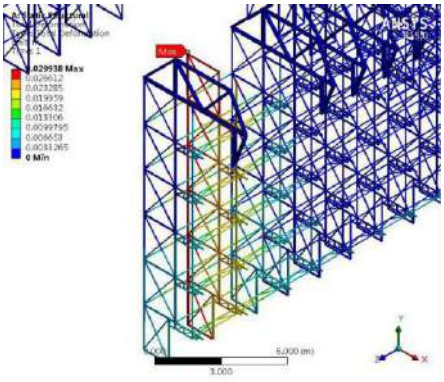

(a) Local structural deformation after removal of truss

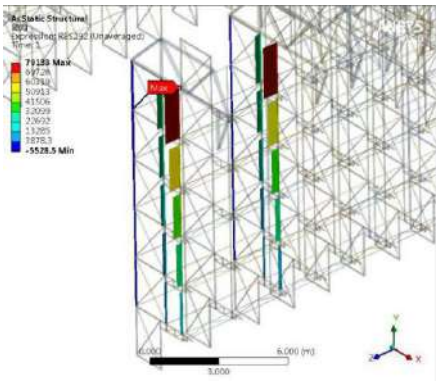

(b) Axis Force of Suspender after Removal of Truss

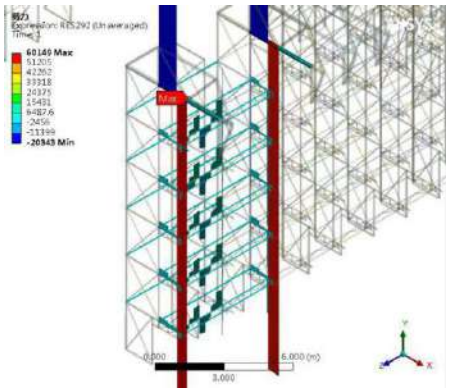

(c) Shear force of surrounding members after removal of truss

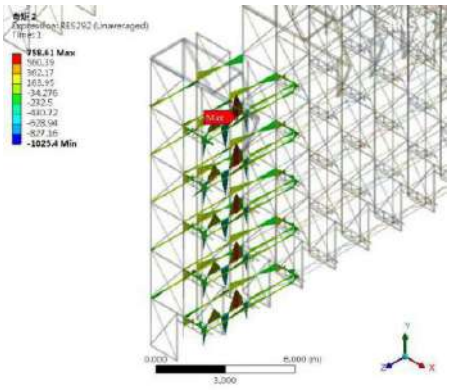

(d) Bending moment of connecting beam after removal of truss

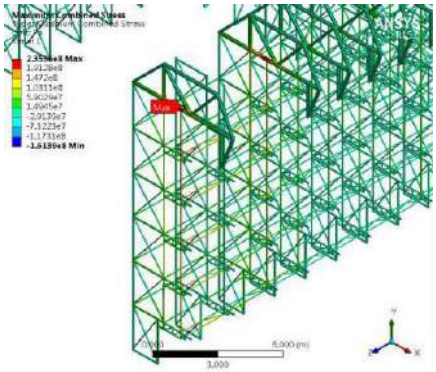

(e) Local structural stress after removal of truss

Figure 2. Local structure response after removing A1-HJ

Table 3. Boom damage judgment after removal of A1-HJ (Based on boom axial deformation)

Number of suspender	Displacement of upper end node of suspender/mm	Displacement of lower end node of suspender/mm	Axial Deformation of Suspender/mm	Deformation limit /mm	Component failure judgment
A2-DG1	-6.62	-6.83	0.21	215	unspoiled
A2-DG2	-6.15	-6.58	0.43	215	unspoiled
A2-DG3	-5.42	-6.07	0.65	215	unspoiled
A2-DG4	-4.37	-5.30	0.93	215	unspoiled
A2-DG5	-2.67	-4.19	1.52	250	unspoiled
A2´-DG1	-6.93	-7.15	0.22	215	unspoiled
A2´-DG2	-6.42	-6.87	0.45	215	unspoiled
A2´-DG3	-5.63	-6.33	0.70	215	unspoiled
A2´-DG4	-4.51	-5.50	0.99	215	unspoiled
A2´-DG5	-2.76	-4.34	1.58	250	unspoiled

Table 4. Beam failure analysis after removal of A1-HJ (Based on beam end shear)

number	Maximum shear force after removal of suspender/kN	Shear ultimate bearing capacity/kN	ratio	Component failure judgment
A1-A2-ZDLJ1	10.1	70.2	0.14	unspoiled
A1-A2-ZDLJ2	10.1	70.2	0.14	unspoiled
A1-A2-ZDLJ3	9.4	70.2	0.13	unspoiled
A1-A2-ZDLJ4	9.8	70.2	0.14	unspoiled
A1-A2-ZDLJ5	9.4	70.2	0.13	unspoiled
A1-A2´-ZDLJ1	6.0	70.2	0.09	unspoiled

DOI: https://doi.org/10.30564/hsme.v2i2.1691

A1-A2´-ZDLJ2	6.2	70.2	0.09	unspoiled
A1-A2´-ZDLJ3	7.2	70.2	0.10	unspoiled
A1-A2´-ZDLJ4	8.6	70.2	0.12	unspoiled
A1-A2´-ZDLJ5	9.8	70.2	0.14	unspoiled
A2-HJ	58.1	187.4	0.31	unspoiled
A2´-HJ	60.1	187.4	0.32	unspoiled

3.1.2 Demolition of Truss A11-HJ

After removing the truss A11-HJ, the response of the structure is shown in Figure 3. The maximum displacement of the surrounding structure after removing the truss is 11.8 mm (Figure (a)). Since A12-HJ links two suspenders, the number suffix of the suspender near the ship's side is added by "a". The maximum axial force in the adjacent suspender is A12-DG5a (Figure (b). The axial stress is 123.6 MPa. The failure analysis is carried out as shown in Table 5.The plastic bending capacity of the frame connection beams connected with the dismantled truss is 1.91 kN. M. The plastic bending capacity of the walkway connection beams and corner connection beams is 1.07 kN. M. The maximum bending moment of each connection beams is 0.48 kN. m (Figure (d)). The section does not enter into plasticity and plastic hinges will not appear. The maximum stress of the structure occurs in the corner connecting beam, and the maximum stress is 204.9 MPa (Figure (e)).The corner connection beams in A12-HJ plane are numbered A12-JQLJ1~A12-JQLJ5 according to the number of layers. According to Table 6, the maximum shear force of each steel beam section is less than the ultimate shear bearing capacity, and shear failure will not occur. Therefore, progressive collapse of the remaining structure will not occur after A11-HJ is completely invalidated.

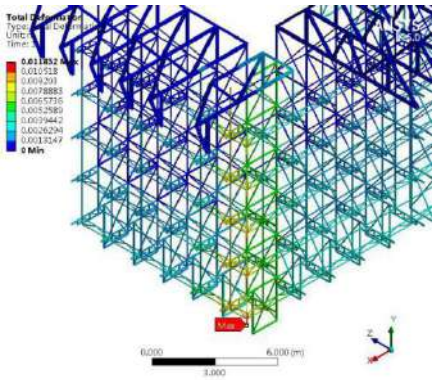

(a) Local structural deformation after removal of truss

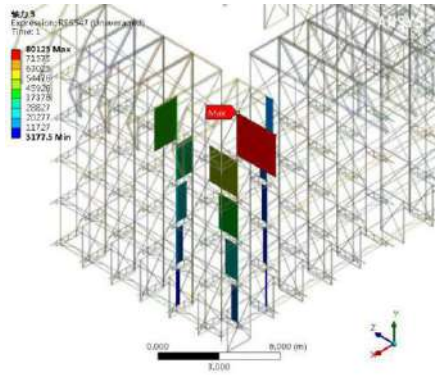

(b) Axis Force of Suspender after Removal of Truss

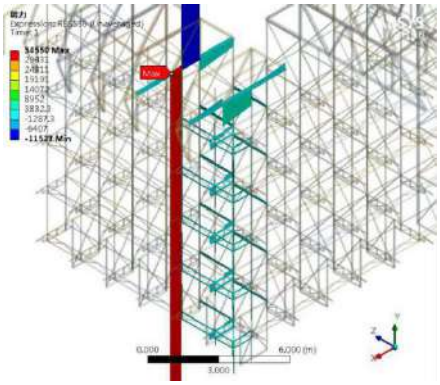

(c) Shear force of surrounding members after removal of truss

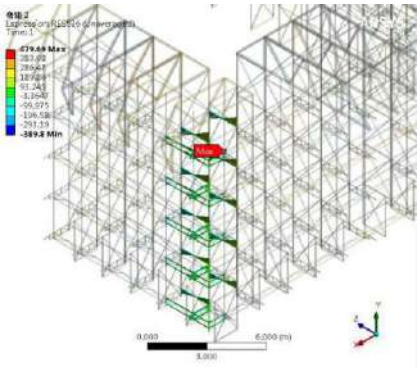

(d) Bending moment of connecting beam after removal of truss

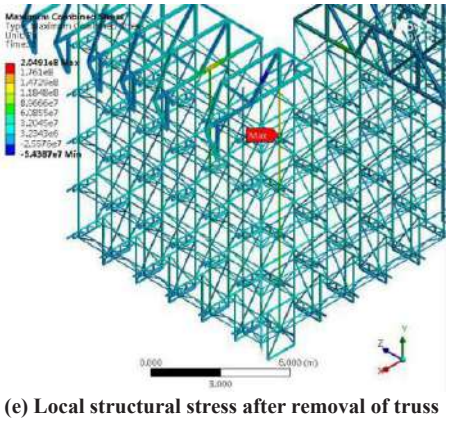

(e) Local structural stress after removal of truss

Figure 3. Local structure response after removing A11-HJ

 DOI: https://doi.org/10.30564/hsme.v2i2.1691

Table 5. Boom damage judgment after removal of A11-HJ (Based on bom axial deformation)

Number of suspender	Displacement of upper end node of suspender/mm	Displacement of lower end node of suspender/mm	Axial deformation of suspender/mm	Deformation limit /mm	Component failure judgment
A12-DG5	-1.99	-3.57	1.58	250	unspoiled

Table 6. Beam failure analysis after removal of A11-HJ (Based on beam end shear)

Number	Maximum shear force after removal of suspender/kN	Shear ultimate bearing capacity/kN	ratio	Component failure judgment
A10-A11-ZDLJ1	2.9	70.2	0.04	unspoiled
A10-A11-ZDLJ2	3.2	70.2	0.05	unspoiled
A10-A11-ZDLJ3	4.2	70.2	0.06	unspoiled
A10-A11-ZDLJ4	5.6	70.2	0.08	unspoiled
A10-A11-ZDLJ5	7.1	70.2	0.10	unspoiled
A12-JQLJ1	3.1	70.2	0.04	unspoiled
A12-JQLJ2	3.8	70.2	0.05	unspoiled
A12-JQLJ3	5.3	70.2	0.08	unspoiled
A12-JQLJ4	7.4	70.2	0.11	unspoiled
A12-JQLJ5	9.7	70.2	0.14	unspoiled
A10-HJ	34.5	187.4	0.18	unspoiled
A12-HJ	2.3	187.4	0.01	unspoiled

3.1.3 Demolition of Truss C4-HJ

After removing the truss C4-HJ, the response of the structure is shown in Figure 4. The maximum displacement of the surrounding structure after removing the truss is 16.4 mm (Figure (a)). The C3-DG5 has the largest axial force and the axial stress is 112.3 MPa (Figure (b). The failure analysis of C3-DG5 is carried out as shown in Table 7. The plastic bending capacity of the frame connection beam connected with the dismantled truss is 1.91 kN m, and the plastic bending capacity of the corridor connection beam is 1.07 kN m, while the maximum bending moment of each connection beam is 0.41 kN m (Figure (d)). The section does not enter into plasticity and no plastic hinge will appear. The maximum stress occurs at the junction of C3-HJ and C3-DG5, and the maximum stress is 214.5 MPa (Figure (e)). Table 8 shows the results of failure analysis of steel beams after removal of C4-HJ based on shear force. It shows that the maximum shear force of each section of steel beams is less than the ultimate shear bearing capacity, shear failure will not occur, and progressive collapse of remaining structures will not occur after complete failure of C4-HJ.

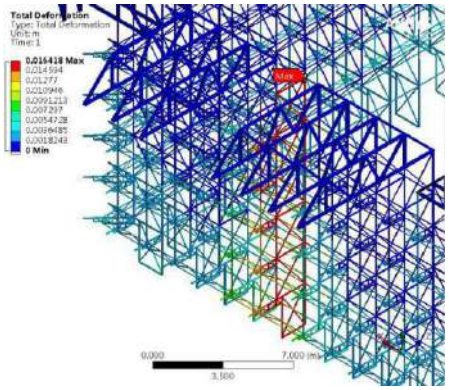

(a) Local structural deformation after removal of truss

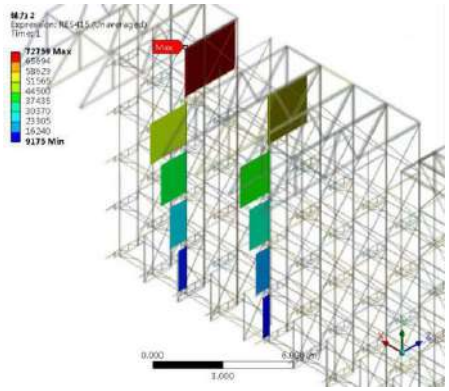

(b) Axis force of suspender after removal of truss

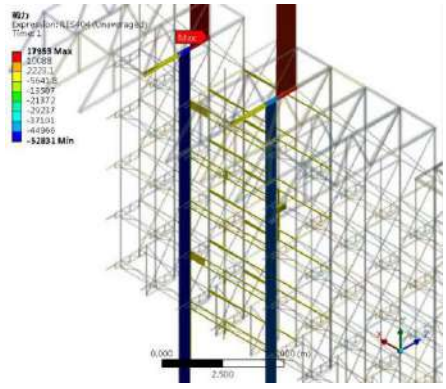

(c) Shear force of surrounding members after removal of truss

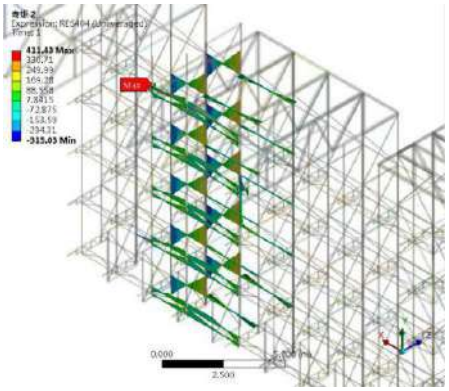

(d) Bending moment of connecting beam after removal of truss

DOI: https://doi.org/10.30564/hsme.v2i2.1691

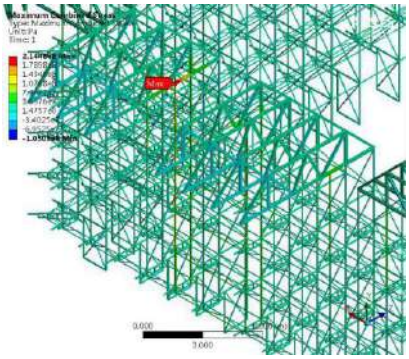

(e) Local structural stress after removal of truss

Figure 4. Local structure response after removing C4-HJ

Table 7. Boom damage judgment after removal of C4-HJ (Based on boom axial deformation)

Number of suspender	Displacement of upper end node of suspender/mm	Displacement of lower end node of suspender/mm	Axial deformation of suspender/mm	Deformation limit /mm	Component failure judgment
C3-DG1	-5.99	-6.17	0.18	215	unspoiled
C3-DG2	-5.57	-5.95	0.38	215	unspoiled
C3-DG3	-4.92	-5.50	0.58	215	unspoiled
C3-DG4	-3.96	-4.80	0.84	215	unspoiled
C3-DG5	-2.41	-3.80	1.39	250	unspoiled
C5-DG1	-5.08	-5.24	0.16	215	unspoiled
C5-DG2	-4.72	-5.05	0.33	215	unspoiled
C5-DG3	-4.16	-4.66	0.50	215	unspoiled
C5-DG4	-3.34	-4.07	0.73	215	unspoiled
C5-DG5	-2.06	-3.22	1.16	250	unspoiled

Table 8. Beam failure analysis after removal of C4-HJ (Based on beam end shear)

Number	Maximum shear force after removal of suspender/kN	Shear ultimate bearing capacity/kN	ratio	Component failure judgment
C3-C4-ZDLJ1	6.0	70.2	0.08	unspoiled
C3-C4-ZDLJ2	6.5	70.2	0.09	unspoiled
C3-C4-ZDLJ3	7.4	70.2	0.11	unspoiled
C3-C4-ZDLJ4	8.5	70.2	0.12	unspoiled
C3-C4-ZDLJ5	9.7	70.2	0.14	unspoiled
C4-C5-ZDLJ1	4.9	70.2	0.07	unspoiled
C4-C5-ZDLJ2	5.5	70.2	0.08	unspoiled
C4-C5-ZDLJ3	6.3	70.2	0.09	unspoiled
C4-C5-ZDLJ4	7.5	70.2	0.11	unspoiled
C4-C5-ZDLJ5	8.4	70.2	0.12	unspoiled
C3-HJ	52.8	187.4	0.28	unspoiled
C5-HJ	44.8	187.4	0.24	unspoiled

According to the above analysis, it can be found that only single truss failures, the remaining structure will not appear progressive damage, indicating that the installation platform structure has good anti-progressive collapse performance. Table 9 gives a comparison of the responses of the remaining structures after removing the three trusses at different locations. It is found that the importance coefficient of the trusses is large, the response of the remaining structures is more significant after removing them.

Table 9. Response of residual structure after removal of trusses

Number of truss	Coefficient of Importance	Maximum displacement of structure/mm	Maximum stress of structure/MPa	Maximum ratio of shear force to bearing capacity of beams	Maximum elongation of adjacent suspenders/mm
A1-HJ	0.1846	29.9	235.4	0.32	1.58
A11-HJ	0.1167	11.8	204.9	0.18	1.58
C4-HJ	0.1267	16.4	214.5	0.28	1.39

3.2 Structural Response to Simultaneous Failure of Two Adjacent Trusses

A1-HJ has the greatest importance, and it is located on the symmetrical plane of the captain direction of the installation platform. Therefore, the structural response of the truss A1-HJ and A2-HJ after simultaneous failure is analyzed, as shown in Figure 5. The maximum displacement of the local structure around the demolished member is 51.5mm (Figure (a)).The largest axial force of the suspender near the dismantled truss is A3-DG5, and the axial stress reaches 171 MPa (Figure (b)).The suspenders of A3 and A2 steel frames are judged. As shown in Table 10, all suspenders will not be damaged. The plastic bending capacity of frame connection beams is 1910N m, the cross-section plastic bending capacity of walkway connection beams is 1070N m, and the maximum bending moment of the connection beams around the dismantled truss is 604.8N m (Figure (d)). No plastic hinges will appear at the end of the beams. The maximum stress of the platform structure is 328.7 MPa (Figure (e)), which appears at the end of A3-A2-ZDLJ5.Table 11 shows the results of failure analysis of the beam after removing A1-HJ and A2-HJ according to the shear force at the end of the beam. It shows that the maximum shear force of the cross-section of the connecting beams and the walkway beams is less than the ultimate shear bearing capacity, and there will be no shear failure, so there will be no progressive collapse of the remaining structures after the truss A1-HJ and A2-HJ fail completely.

 DOI: https://doi.org/10.30564/hsme.v2i2.1691

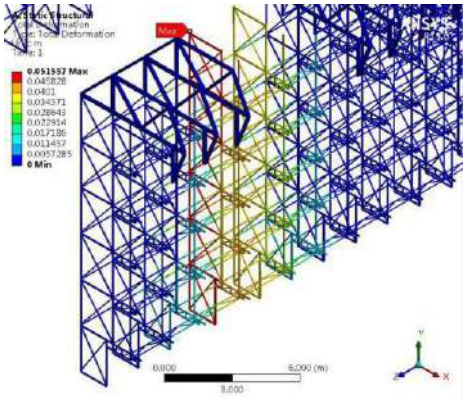

(a) Local structural deformation after removal of truss

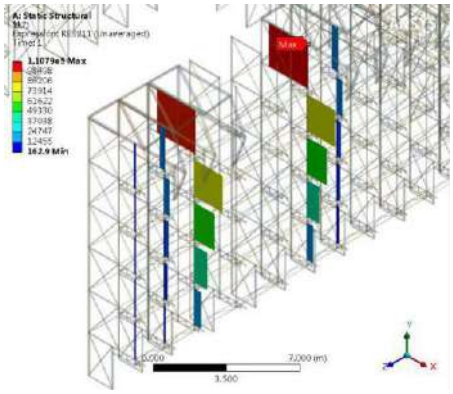

(b) Axis force of suspender after removal of truss

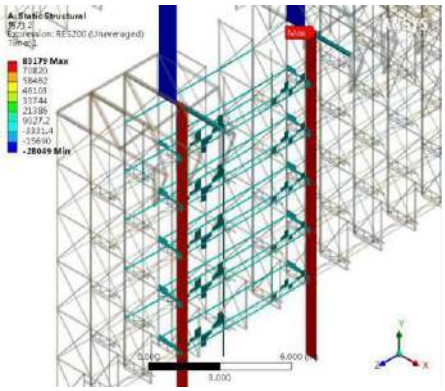

(c) Shear force of surrounding members after removal of truss

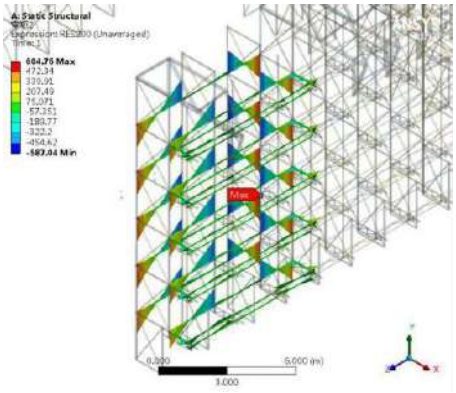

(d) Bending moment of connecting beam after removal of truss

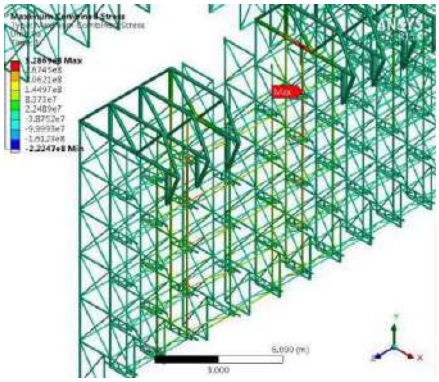

(e) Local structural stress after removal of truss

Figure 5. Local structure response after removing A1-HJ, A2-HJ

Table 10. Boom damage judgment after removal of A1-HJ, A2-HJ (Based on boom axial deformation)

Number of suspender	Displacement of upper end node of suspender/mm	Displacement of lower end node of suspender/mm	Axial deformation of suspender/mm	Deformation limit /mm	Component failure judgment
A3′-DG1	-9.93	-10.25	0.32	215	unspoiled
A3′-DG2	-9.23	-9.87	0.64	215	unspoiled
A3′-DG3	-8.11	-9.11	1.00	215	unspoiled
A3′-DG4	-6.51	-7.93	1.42	215	unspoiled
A3′-DG5	-3.99	-6.29	2.30	250	unspoiled
A2-DG1	-8.20	-8.47	0.27	215	unspoiled
A2-DG2	-7.61	-8.15	0.54	215	unspoiled
A2-DG3	-6.69	-7.52	0.83	215	unspoiled
A2-DG4	-5.38	-6.55	1.17	215	unspoiled
A2-DG5	-3.29	-5.18	1.89	250	unspoiled

Table 11. Beam failure analysis after removal of A1-HJ, A2-HJ (Based on beam end shear)

Number	Maximum shear force after removal of suspender/kN	Shear ultimate bearing capacity/kN	ratio	Component failure judgment
A3′-A2′-ZDLJ5	14.9	70.2	0.078	unspoiled
A3′-A2′-ZDLJ4	13.2	70.2	0.078	unspoiled
A3′-A2′-ZDLJ3	11.3	70.2	0.084	unspoiled
A3′-A2′-ZDLJ2	9.3	70.2	0.098	unspoiled
A3′-A2′-ZDLJ1	8.5	70.2	0.137	unspoiled
A2-A1-ZDLJ5	12.6	70.2	0.179	unspoiled
A2-A1-ZDLJ4	11.5	70.2	0.164	unspoiled

DOI: https://doi.org/10.30564/hsme.v2i2.1691

A2-A1-ZDLJ3	9.8	70.2	0.140	unspoiled
A2-A1-ZDLJ2	8.6	70.2	0.123	unspoiled
A2-A1-ZDLJ1	8.4	70.2	0.120	unspoiled
A3′-ZD5	16.3	148.5	0.110	unspoiled
A3′-ZD4	15.3	148.5	0.103	unspoiled
A3′-ZD3	13.2	148.5	0.089	unspoiled
A3′-ZD2	10.4	148.5	0.070	unspoiled
A3′-ZD1	7.3	148.5	0.049	unspoiled
A2-ZD5	13.6	148.5	0.092	unspoiled
A2-ZD4	12.7	148.5	0.086	unspoiled
A2-ZD3	10.8	148.5	0.073	unspoiled
A2-ZD2	8.5	148.5	0.057	unspoiled
A2-ZD1	6.0	148.5	0.041	unspoiled
A3′-HJ	86.5	187.4	0.46	unspoiled
A2-HJ	71.4	187.4	0.38	unspoiled

The sum of A1-HJ and A2-HJ importance coefficients is the largest in the adjacent two trusses. According to the conclusion of section 2.1, it can be concluded that the adjacent two trusses fail and the remaining structure will not collapse continuously.

3.3 Structural Response of Three Trusses to Simultaneous Failure

A1-HJ is of the greatest importance and it is located on the symmetrical plane in the direction of the captain of the installation platform. Therefore, the structural responses of three trusses in this area after simultaneous failure are analyzed, as shown in Figure 6. The steel frame area of hanging layer A1 has a large displacement, reaching 110 mm (Figure (a)).At the lower chord of A3'-HJ, the maximum shear force is 142 kN(Figure (c). The maximum shear force of the corridor connection beam is 24.2 kN. The ultimate shear force of the frame connection beam is 70.2 kN. The ultimate shear force of the frame connection beam is 0.98 kN. The ultimate shear force of the frame connection beam is 116.1 kN. No shear failure occurs. The maximum positive bending moment is 1.3kN m (Figure (d)) and the plastic bending capacity is 1.07kN m, which has entered the plasticity. The maximum negative bending moment occurs at the end of A3'-ZD5, which is 1.87kN M. The plastic bending capacity of the cross-section of the walkway beam is 3.2kN m, and bending failure will not occur. The maximum bending moment is 0.97 kN m and the plastic bending capacity is 1.91 kN m, so there will be no bending failure. The maximum stress of the structure is 576 MPa (Figure (e). It occurs at the end of A3-A2-ZDLJ5, far exceeding the material failure stress of 450 MPa. At the same time, the material failure stress is also exceeded by the lower chord of A3'-HJ and A3-HJ, the end of A3'-A2'-ZDLJ5 and the end of A3-A2-ZDLJ4.

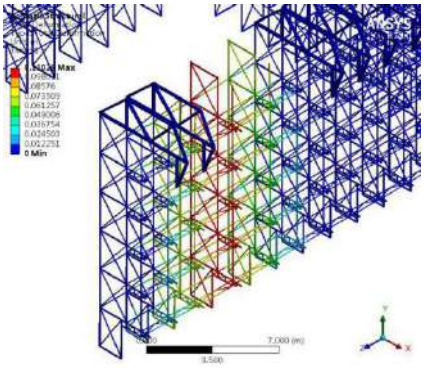

(a) Local structural deformation after removal of truss

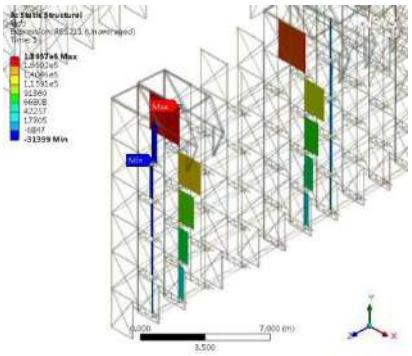

(b) Axis force of suspender after removal of truss

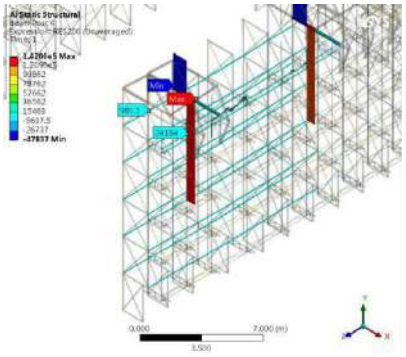

(c) Shear force of surrounding members after removal of truss

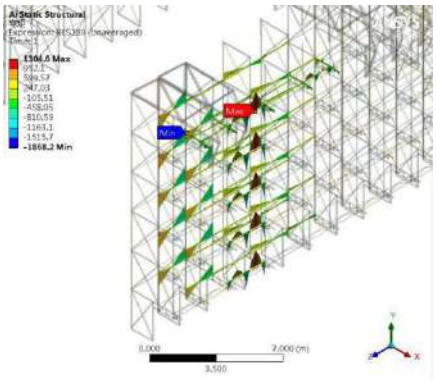

(d) Bending moment of connecting beam after removal of truss

 DOI: https://doi.org/10.30564/hsme.v2i2.1691

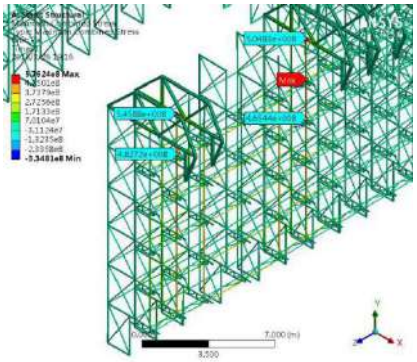

(e) Local structural stress after removal of truss

Figure 6. Local structure response after removing A1-HJ, A2-HJ, A2′-HJ

Due to the end failure of A3'-A2'-ZDLJ5, A3-A2-ZDLJ4, A3-A2-ZDLJ5 and the end failure of the connection between A3-HJ and A3'-HJ lower chord and suspender, the finite element corresponding to this location needs to be "killed" in the software. The remaining structures are further calculated and analyzed, as shown in Figure 7. A large displacement occurred in A1 steel frame area, the maximum displacement was 184.9 mm (Figure (a)). As shown in the stress diagram (b), except that the end of A3-ZD1 does not exceed the material damage stress limit, material damage occurs at the end of A3 steel frame and other aisle beams of A3' steel frame, and material damage occurs at the hangers connected with the aisle beams.

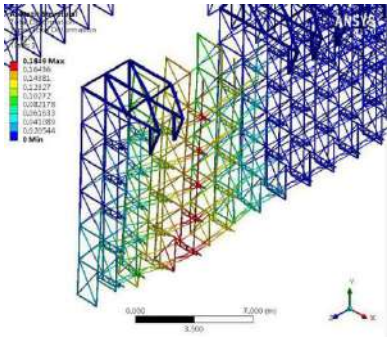

(a) Local structural deformation after removal of failure members

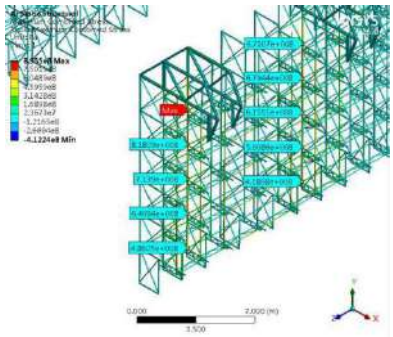

(b) Local structural stress after removal of failure components

Figure 7. Local structural response after removing the invalid component

The damage element is killed and the residual structure is analyzed. The calculation results are shown in Figure 8. The maximum displacement of the dismantled truss area is 542.5mm (Figure (a)); the minimum bending moment of the frame connection beam between A3' and A2' is 3.9kN.m (Figure (b)), forming plastic hinges. As shown in Table 12, the plastic hinge rotation angles at the ends of each frame connection beam exceed the limit of 6.0 plastic hinge angle of the steel beam. It can be judged that the end sections of each frame connection beam between A3' and A2' is destroyed. Large-scale collapse and destruction occurred in the region. Therefore, when A1-HJ, A2-HJ and A2'-HJ are demolished at the same time, progressive damage will be caused, leading to the collapse of large-scale structures. In the process of using the structure, it is necessary to pay attention to the truss in this area to prevent the simultaneous failure of A1-HJ, A2-HJ and A2'-HJ, and to avoid unnecessary losses.

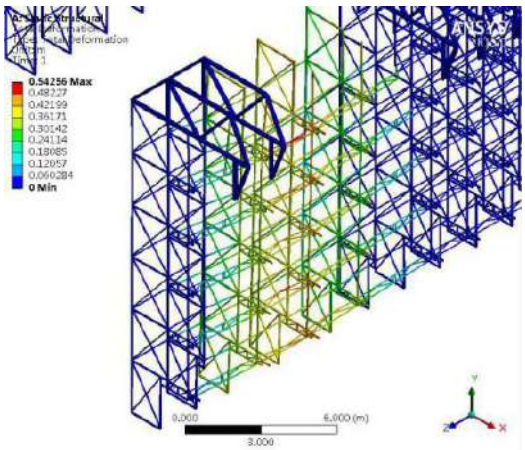

(a) Local structural deformation after removal of failure members

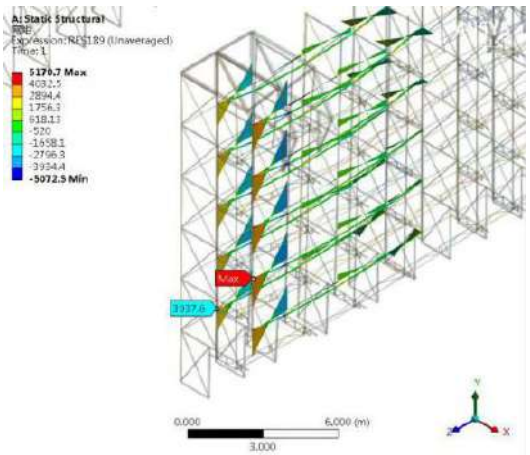

(b) Bending moment of connecting beam after removing failure members

Figure 8. Local structural response after removing the invalid component

DOI: https://doi.org/10.30564/hsme.v2i2.1691

Table 12. The angle of frame connection beam between A3′ and A2′

Number	Displacement Difference of Beam End Joints/mm	Beam length/ mm	Corner of beam end/°	Deformation limit/°
A3′-A2′-KJLJ5a	246	2000	7.1	6
A3′-A2′-KJLJ5b	286	2000	8.2	6
A3′-A2′-KJLJ4a	231	2000	6.6	6
A3′-A2′-KJLJ4b	280	2000	8.0	6
A3′-A2′-KJLJ3a	230	2000	6.6	6
A3′-A2′-KJLJ3b	270	2000	7.8	6
A3′-A2′-KJLJ2a	227	2000	6.5	6
A3′-A2′-KJLJ2b	275	2000	7.9	6
A3′-A2′-KJLJ1a	256	2000	7.4	6
A3′-A2′-KJLJ1b	304	2000	8.7	6

4. Conclusion

This paper simulates the response of the remaining structure after the failure of some trusses of the secondary shielding installation platform for A-type tank, and evaluates the anti-progressive collapse ability of the installation platform structure. The conclusions are as follows:

(1) The failure of three trusses with larger importance coefficient is simulated separately. It is found that the importance coefficient of components is larger, the influence of failure on the residual structure is greater, and the failure analysis of two trusses is also guided.

(2) No further progressive damage will occur after the two trusses of the installation platform completely are invalid.

(3) When A1-HJ, A2-HJ and A2'-HJ are demolished at the same time, progressive damage will be caused locally, which can lead to the collapse of large-scale structures. To prevent the failure of the suspenders ZD-1 and ZD-2 at the same time and avoid unnecessary losses, it is necessary to pay attention to the suspenders of this area.

(4) The vertical bearing components of the installation platform all bear tension which do not need to consider the instability, and the spatial arrangement of the structure is relatively flexible. Therefore, the installation platform is a relatively promising structural form.

References

[1] Kim J, Kim T. Assessment of progressive collapse-resisting capacity of steel moment frames[J]. Journal of Constructional Steel Research, 2009, 65(1): 169-179.

[2] Xiaobin Hu, jiaru Qian. Progressive Collapse Simulation of A Multi-story Steel Frame[J]. Mechanics and practice, 2008, 30(4): 54-57.

[3] Yue Wang, Yongzheng Li, Zhiyong Jiang. Analysis of Structural Strength of Scaffolding Platform for Liquid Tank of LNG Carrier[J]. Shipbuilding of China, 2011, 52(4): 161-168.

[4] Changde Tang, Qingfeng Wang, yong Li. Research on Key Technology of Structural Design of Scaffolding Platform of LNG Carrier[J]. Jiangsu Ship, 2013, 30(5): 15-16.

[5] Kaixuan Chen. Reliability Analysis of the Scaffolding Platform of the LNG Cargo Containment System under the Limit State[D]. Jiangsu University of Science and Technology, 2015.

[6] Fuzhe Xie, Ganping Shu. Research on The Mode Method of Progressive Collapse Analysis of Steel Frame Structures[J]. Engineering Mechanics, 2011, 28(10): 34-40.

[7] Yang Ding, Jian Sun. Progressive collapse analysis on the suspension structure of Tianjin Grand Theatre [J]. Building Structure, 2013(10): 16-20.

[8] Gege Zhang. The study on Progressive collapse of Multistory frame structure [D]. AnHui University of Science and Technology, 2014.

[9] Yang Zheng. A study of critical element of the structure during the progressive collapse and sensitivity analysis[D]. Zhejiang University, 2013, 39(5): 746-750.

 DOI: https://doi.org/10.30564/hsme.v2i2.1691

BILINGUAL PUBLISHING CO.
Pioneer of Global Academics Since 1984

Hydro Science & Marine Engineering
https://ojs.bilpublishing.com/index.php/hsme

ARTICLE

Stilling and its Aerodynamic Effects on Pan Evaporation

Qiang Liu [1,2] Sirui Yan [1,2] Liqiao Liang [3,4] Liya Su [1,2*]

1. Key Laboratory for Water and Sediment Sciences, Ministry of Education, School of Environment, Beijing Normal University, Beijing 100875, China
2. State Key Laboratory of Water Environment Simulation, School of Environment, Beijing Normal University, Beijing, 100875, China
3. Key Laboratory of Tibetan Environment Changes and Land Surface Processes, Institute of Tibetan Plateau Research, Chinese Academy of Sciences, Beijing 100101, China
4. Center for Excellence in Tibetan Plateau Earth Sciences, Chinese Academy of Sciences, Beijing 100101, China

ARTICLE INFO

Article history
Received: 7 August 2020
Accepted: 30 September 2020
Published Online: 30 October 2020

Keywords:
Wind speed
Pan evaporation
Stilling
PenPan model
Aerodynamic effect

ABSTRACT

Declines in wind speed (u) (termed as "stilling") has been reported in many regions of the world. To explore the temporal trends of u and its aerodynamic effects is vital to understand the changes in water resources. This study analyzed the changes of temporal trends for u and its aerodynamic effects using the data during 1959-2000 at 266 stations across China. The improved PenPan model was used to estimate pan evaporation (E_{pan}) and quantify the contribution of radiative and aerodynamic components (aerodynamic component separated into wind speed u, vapour pressure deficit D, and air temperature Ta). Climate factors include E_{pan} measured with the standard Chinese 20 cm diameter pan, u, Ta, relative humidity (rh) and sunshine hours (sh). The results showed: stilling occurred in most of stations (206 among 266) and 105 stations presented significant decreasing trends at 99% confidence level; stilling was the main cause for controlling the trends in E_{pan} in most part of China, especially in the west and north of China. The results indicated that decreasing trends in E_{pan} due to stilling would inevitably alter water resources, and should be put further investigation incorporation other factors.

1. Introduction

Declining rates of observed near-surface wind speed (u) (termed a "stilling", [1] are usually on the order of -0.010 m s^{-1} a^{-1} [2]. Stilling has been reported in many regions around the world, summarized by McVicar *et al*. [3] in Table 2, e.g., Australia [1], China [4], and North America [5]. Stilling alters the aerodynamic condition, which is the key factor in the fully physical-

**Corresponding Author:*
Liqiao Liang,
Key Laboratory of Tibetan Environment Changes and Land Surface Processes, Institute of Tibetan Plateau Research, Chinese Academy of Sciences, Beijing 100101, China;
Center for Excellence in Tibetan Plateau Earth Sciences, Chinese Academy of Sciences, Beijing 100101, China;
Email: liangliqiao@itpcas.ac.cn;
Liya Su,
Key Laboratory for Water and Sediment Sciences, Ministry of Education, School of Environment, Beijing Normal University, Beijing 100875, China;
State Key Laboratory of Water Environment Simulation, School of Environment, Beijing Normal University, Beijing, 100875, China;
Email: liya@bnu.edu.cn

DOI: https://doi.org/10.30564/hsme.v2i2.2266

ly-based models to assess the evaporation demand [6,7], such as potential evaporation (E_p), references evapotranspiration (ET_0) and pan evaporation (E_{pan}). Due to its simplicity and cost effectiveness, E_{pan} has been widely used to reflect the evaporation demand of the atmosphere when estimating terrestrial evaporation [8] and crop water requirement [9].

The "evaporation paradox" phenomenon, that is decline trend in pan evaporation with increasing trend in air temperature, has drawn great attention to explore causes for changes in pan evaporation and its application for global hydrological cycle [2, 10]. Different from the empirical method used to estimate pan evaporation [11-15], Rotstayn *et al*. [16] combined the works of Linacre [17] and Thom *et al*. [18] to develop a steady state pan evaporation model for a US Class A pan called the "PenPan model, which has been used to assess the cause of pan evaporation (e.g., Roderick *et al*., [1]). Improved by Yang and Yang [19], PenPan model also was used to simulate the changes in pan evaporation for the standard Chinese 20 cm diameter pan (D20 pan). According to Yang and Yang [19] and Xie *et al*. [20], the declines in u were the main causes for changes in pan evaporation in most parts of China. As pointed out by Thom *et al* [18], vapour transfer function- $f_q(u)$ depends not only on wind speed but also on the difference between surface temperature for water and air temperature [18]. Thom *et al*., (1981) [18] deduced the wind function f_q(u) (unit: mm d^{-1} mb^{-1}) as:

$$f_q(u) = 0.12 \times (1 + 1.35u) \tag{1}$$

where, u (m s^{-1}) is the mean wind speed at two meters above the ground. Yang and Yang (2012) [19] deduced the $f_q(u)$ using the data in Beijing stations as:

$$f_q(u) = 5.4 \times (1 + 0.40u) \tag{2}$$

Vapour transfer function should be an attractive approach to establish a physical model and derive its differential to analyze the attribution of changes in E_{pan} [19]. Consequently, the objectives of the present study are: (*i*) to explore the temporal trends for u across China, and explain where can found the stilling; and (*ii*) to improve the PenPan model using vapour transfer function, and to explain aerodynamic effects of declines of u. To address these objectives the remainder of this paper is structured as followed: section 2 presented the physical model for analyzing the aerodynamic effects of stilling; section 3 explained the materials and method; section 4 explored the temporal trends for u; and section 5 gave the aerodynamic effects of the stilling.

2. Materials and Method

2.1 Assessing the Aerodynamic Effects of Stilling Using PenPan Model

The PenPan model is based on Penman's combination equation, using Linacre [17] and Thom *et al*. [18] models to describe the radiative and aerodynamic components [16], respectively. The PenPan model can be represented as:

$$E_p = E_{p,R} + E_{P,A} = \left(\frac{s}{s+a\gamma}\frac{R_n}{\lambda}\right) + \left(\frac{a\gamma}{s+a\gamma}\frac{f_q(u)D}{\lambda}\right) \tag{3}$$

where, s (P$_a$ K^{-1}) is the change in saturation vapour pressure (e_s, Pa) with temperature evaluated at the air temperature (T_a, K) two meters above the ground, R_n (W m^{-2}) is the net radiation on the pan, λ (J kg^{-1}) is the latent heat of vaporization, α is the ratio of effective surface area for heat and vapour transfer (α=5 for D20 pan) [19], γ (~67 Pa K^{-1}) is the psychrometric constant, D (= e_s-e_a, Pa) is the vapour pressure deficit at two meters, and $f_q(u)$ (mm d^{-1} mb^{-1}) is the vapour transfer function.

Following Roderick *et al*. [1], changes in pan evaporation can result from radiative and aerodynamic components and be given by differentiating equation,

$$\frac{\mathrm{d}E_p}{\mathrm{d}t} = \frac{\mathrm{d}E_{p,R}}{\mathrm{d}t} + \frac{\mathrm{d}E_{p,A}}{\mathrm{d}t} \tag{4}$$

Then $\mathrm{d}E_{p,A}/\mathrm{d}t$ is partitioned into three components, denoted U*, D* and T* for changes in u, D and T_a respectively. The components are defined by,

$$\frac{\mathrm{d}E_{p,A}}{\mathrm{d}t} \approx \frac{\mathrm{d}E_{p,R}}{\mathrm{d}u}\frac{\mathrm{d}u}{\mathrm{d}t} + \frac{\mathrm{d}E_{p,R}}{\mathrm{d}u}\frac{\mathrm{d}D}{\mathrm{d}t} + \frac{\mathrm{d}E_{p,R}}{\mathrm{d}T_a}\frac{\mathrm{d}T_a}{\mathrm{d}t} = \mathrm{U}^* + \mathrm{D}^* + \mathrm{T}^* \tag{5}$$

As u trends present different patterns, we get $f_q(u)$~u from 266 stations using 1959-1969 monthly data. According to the $f_q(u)$, the improved PenPan model based on Yang and Yang's [19] equation is used to assess the aerodynamic effects of u changes across China.

2.2 Meteorological Data

In order to test the temporal trends for u and its aerodynamic effects on E_{pan}, data were collected from China Meteorological Administration (CMA), including monthly E_{pan}, u, T_a, relative humidity (rh) and sunshine hours (sh) from 266 stations across China (Figure 1). Considering the data integrity and continuity, 266 stations were selected to do this work during 1959-2000 (Figure 1).

 DOI: https://doi.org/10.30564/hsme.v2i2.2266

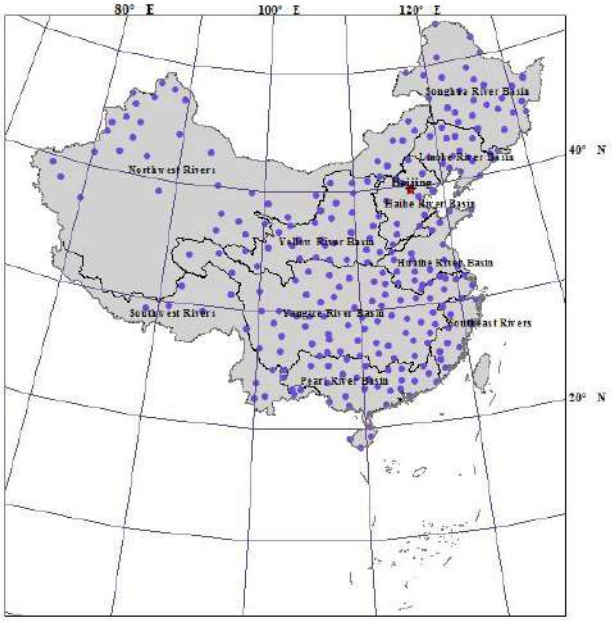

Figure 1. Locations of meteorological stations across China used in this study. Furthermore, basins also presented in the Figure, such as Songhua River Basin (SRB), Liaohe River Basin (LRB), Haihe River Basin (HHRB), Yellow River Basin (YRB), Huaihe River Basin (HuaiRB), Yangtze River Basin (YzRB), Pearl River Basin (PRB), Southwest Rivers Basin (SWRB), Northwest Rivers Basin (NWRB) and Southeast Rivers Basin (SERB)

Due to that radiation component was not observed at most stations, net radiation (R_n) was calculated at monthly scale using the equation as follows:

$$R_n = (1-\alpha_p)R_{sp} + R_{l,in} - R_{l,out} \quad , \tag{6}$$

where, R_{sp} is the incoming shortwave radiation on a pan, $R_{l,in}$ is the incoming longwave radiation, $R_{l,out}$ is the outgoing longwave radiation, estimated by assuming that the pan is a black body radiating at T_a, α_p is constant (=0.14).

$$R_{sp} = \left[f_{dir}P_{rad} + 2.0*(1-f_{dir}) + 2.0*A_s\right]R_s \quad , \tag{7}$$

where R_s is the downward solar irradiance at the surface, f_{dir} is the fraction of R_s that is direct, A_s (=0.23) is the albedo of the ground surrounding the pan, and P_{rad} is the pan radiation factor, which accounts for the extra direct irradiance intercepted by the walls of the pan when the sun is not directly overhead.

$$R_{l,in} = \sigma T_a^4 (1-(0.34-0.14\sqrt{e_a/1000}) \cdot (1.35R_s/(R_o(0.75+2\times10^{-5}z))-0.35)) \quad , \tag{8}$$

where σ is Stefan-Boltzmann constant (4.903*10^{-9} MJ m^{-2} K^{-4}day^{-1}), e_a is the actual vapor pressure (P_a), R_o is solar radiation on the top of the atmosphere, and z (m) is the station elevation [9].

3. Results

3.1 The Trends Pattern of Wind Speed Over China

As showed in Figure 2, stilling phenomena has experienced across China. The average u trend of -0.012 m s^{-1} a^{-1} was in agreement with results presented for other mid-latitude site. Furthermore, temporal trends for u in mid-latitude basins (i.e. HuaiRB: -0.023 m s^{-1} a^{-1}; NWRB: -0.022 m s^{-1} a^{-1}) presented obviously downward trends, followed by north basins (i.e. SHRB: -0.015 m s^{-1} a^{-1}, LHRB: -0.013 m s^{-1} a^{-1}) and south regions (i.e. YzRB: -0.008 m s^{-1} a^{-1}, PRB: -0.008 and SWRB: -0.001 m s^{-1} a^{-1}).

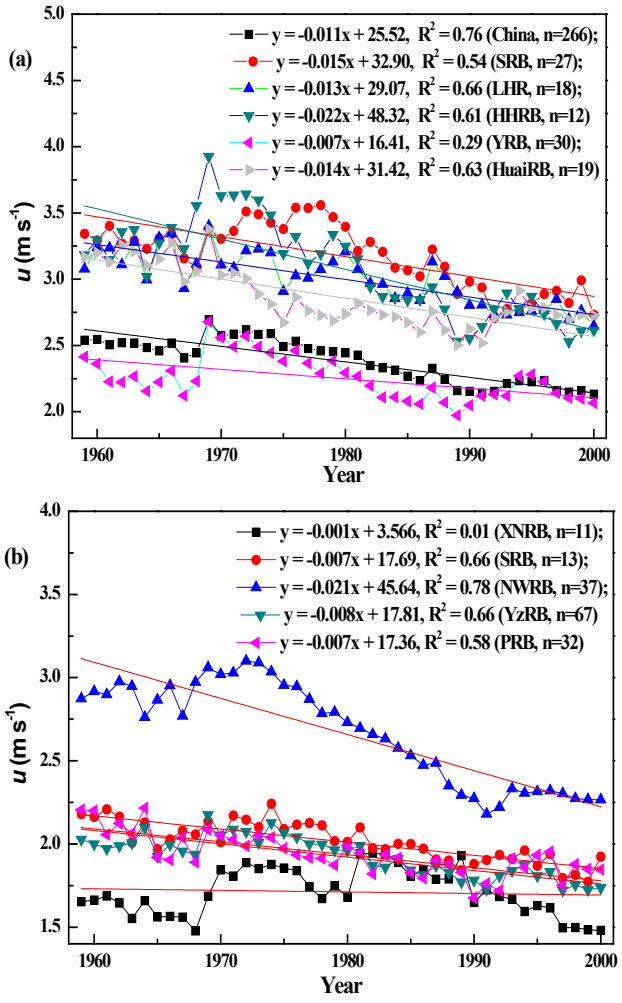

Figure 2. The temporal trend of u in different regions of China. Furthermore, number of stations used in different basin also presented in the bracket

DOI: https://doi.org/10.30564/hsme.v2i2.2266

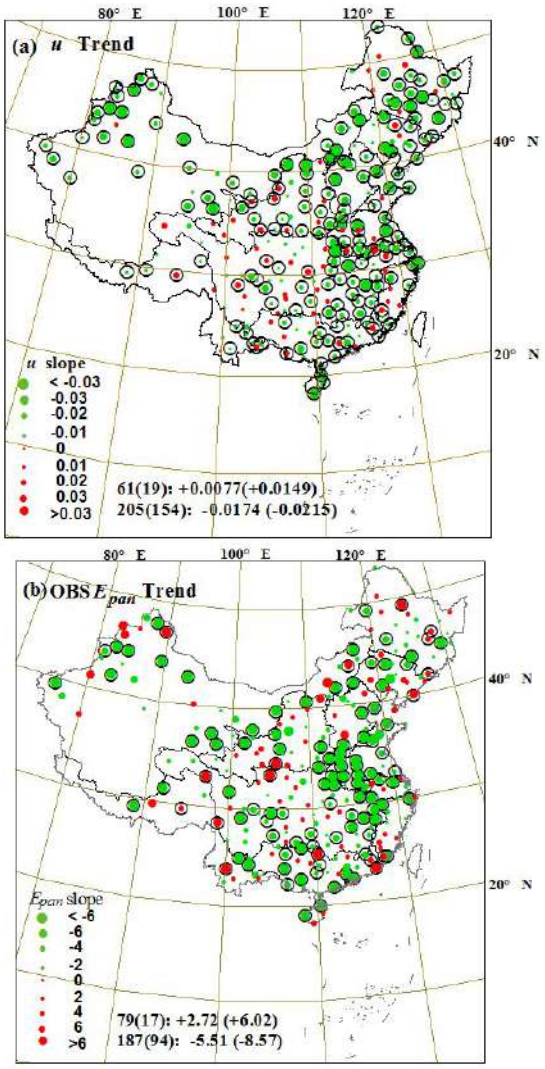

Figure 3. Temporal trends for u (a) and E_{pan} (b) across China during 1959-2000. If the trend is significant ($P < 0.01$), a ring is placed around the dot; units is m $s^{-1}a^{-1}$ for u and mm a^{-2} for E_{pan}. The values located in the bottom of plot are interpreted as follows. The first line shows in order from left to right: (1) the number of stations with positive u and E_{pan} trends; (2) in parenthesis the number of stations with significant ($P < 0.01$) positive u and E_{pan} trends; (3) the u and E_{pan} trend (units = mm a^{-2}) calculated for all stations with positive trends; and (4) in parenthesis the u and E_{pan} trend (units = mm a^{-2}) calculated for all stations with significant ($P < 0.01$) positive u and E_{pan} trends. The second line presents the same four statistics except for stations exhibiting negative u and E_{pan} trends

The temporal trends for u (Figure 3a) presented that: (1) most of stations (205 among 266) presented negative trends with an average slope of -0.0174 m s^{-1} a^{-1}, while only 61 stations showed positive trends with an average slope of 0.0077 m s^{-1} a^{-1}; (2) especially, there were 154 stations showing significant negative trends at 99% confidence level with an average slope of -0.0215 mm a^{-2}, and only 19 stations showed significant positive trends at 99% confident level with an average slope of 0.0149 mm a^{-2}. Stilling in u altered the E_{pan} trends. As showed in Figure 3b, E_{pan} presented similar trends with the changes in u trends: (1) most of stations (187 among 266) showed negative trends, while only 79 stations presented positive trends; (2) the numbers of stations showing negative and positive significant trends at 99% confident level were 94 and 17, respectively.

3.2 Aerodynamic Effects of Stilling on the E_{pan}

Using data from 266 stations during 1959-1969, $f_q(u)$~u equation can be recalibrated from equation (9):

$$f_q(u) = 9.58\times(1+0.40u)\ R^2 = 0.27. \quad (9)$$

The equation was used to simulate the E_{pan} across China. The calculated E_{pan} was compared with observed E_{pan} in 266 stations (Figure 4). Compared with results using Yang and Yang's equation [19] (y=2.54+1.62x, R^2=0.91, RMSE=107 mm mth^{-1}), the agreement between improved modeled and observed E_{pan} at 266 stations (y=8.73+0.99x, R^2=0.94, RMSE=23 mm mth^{-1}) was excellent.

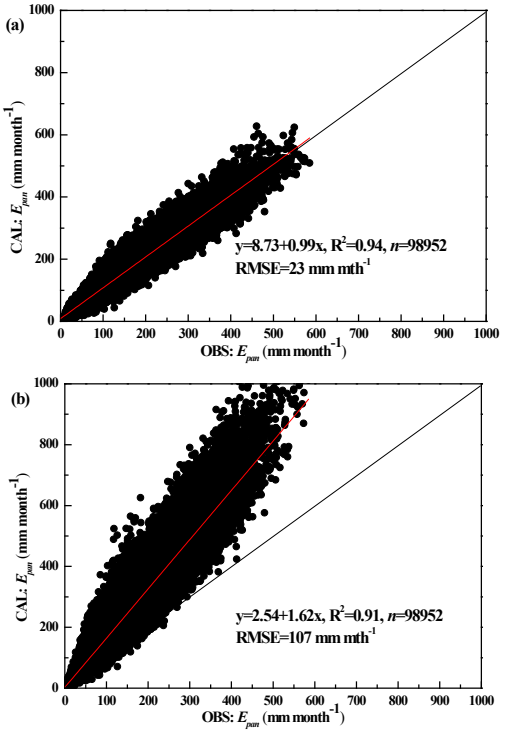

Figure 4. Comparison of the observed (OBS) and calculated (CLAC) monthly E_{pan} during 1970-2000 from 266 stations across China. (a) using $f_q(u)$ from Eq. (9), (b) using $f_q(u)$ from Eq. (2) for Yang and Yang[19]'s equation. Best fit regression and 1:1 line were also showed. Furthermore, the R^2 and RMSE were showed for the 98952 data between observed and calculated monthly E_{pan}.

 DOI: https://doi.org/10.30564/hsme.v2i2.2266

Following the method provided by Roderick *et al*. [1], we separated the E_{pan} rate into radiative and aerodynamic components, and then aerodynamic component was separated into three individual components (U*, D* and T*) (showed in Table 1 and Figure 5). The results showed: (1) changes in aerodynamic component controlled the trends in E_{pan} (Figure 5.c), and changes in u contributed majority of changes in E_{pan} trends (Figure 5d); (2) the changes in D (Figure 5e) and T_a (Figure 5f) attributed a minor changes in E_{pan} trends; (3) as expected, E_{pan} trends and its radiative and aerodynamic components showed spatial variations, i.e, u contributed negative effects in E_{pan} trends, especially in NWRB and middle and lower regions of YRB and Upper reaches of HuaiRB. The downward trends in u resulted in two regions showing large decreasing trends in E_{pan}, NWRB, and the regions in Middle-lower regions YRB and upper HuaiRB (Table 1 and Figure 5), that consistent with the trends in OBS E_{pan} (Figure 3b); and (4) as showed in Table 1 and Figure 5, u and T_a played negative effect in $E_{pan,A}$ trends, while changes in D contributed a positive effect in $E_{pan,A}$ trends, which resulted in an increasing E_{pan} trends in YRB, PRB, SWRB and SERB and opposite trends showed in others basins (Table 1).

Table 1. Observed (OBS) and model-calculated (CACL) trends in E_{pan} rate (dE_{pan}/dt, in mm a^{-2}) in different regions of China for 1959-2000

Regions	OBS	CAL-C=Rad+Aero	Rad	Aero	Aero Partition		
	dE_{pan}/dt	dE_{pan}/dt	$dE_{pan,R}/dt$	$dE_{pan,A}/dt$	U^*	D*	T*
China	-3.06	-1.11	-0.06	-1.06	-2.51	1.69	-0.33
SRB	-1.21	0.36	0.39	-0.03	-2.39	2.84	-0.42
LRB	-0.89	-0.30	0.17	-0.47	-2.76	2.90	-0.44
HHRB	-4.41	-1.45	0.21	-1.66	-4.79	3.53	-0.53
YRB	-2.82	1.13	0.30	0.83	-1.80	2.80	-0.44
HuaiRB	-7.48	-2.25	-0.44	-1.81	-2.74	0.63	-0.25
YzRB	-3.00	-1.61	-0.51	-1.10	-1.49	0.24	-0.11
PRB	-3.10	0.77	-0.35	1.12	-1.59	2.97	-0.23
NWRB	-4.38	-5.42	0.41	-5.83	-5.86	0.83	-0.64
SWRB	0.02	1.13	0.44	0.69	-0.43	1.50	-0.28
SERB	-1.83	-0.23	-0.57	0.33	-1.34	1.79	-0.15

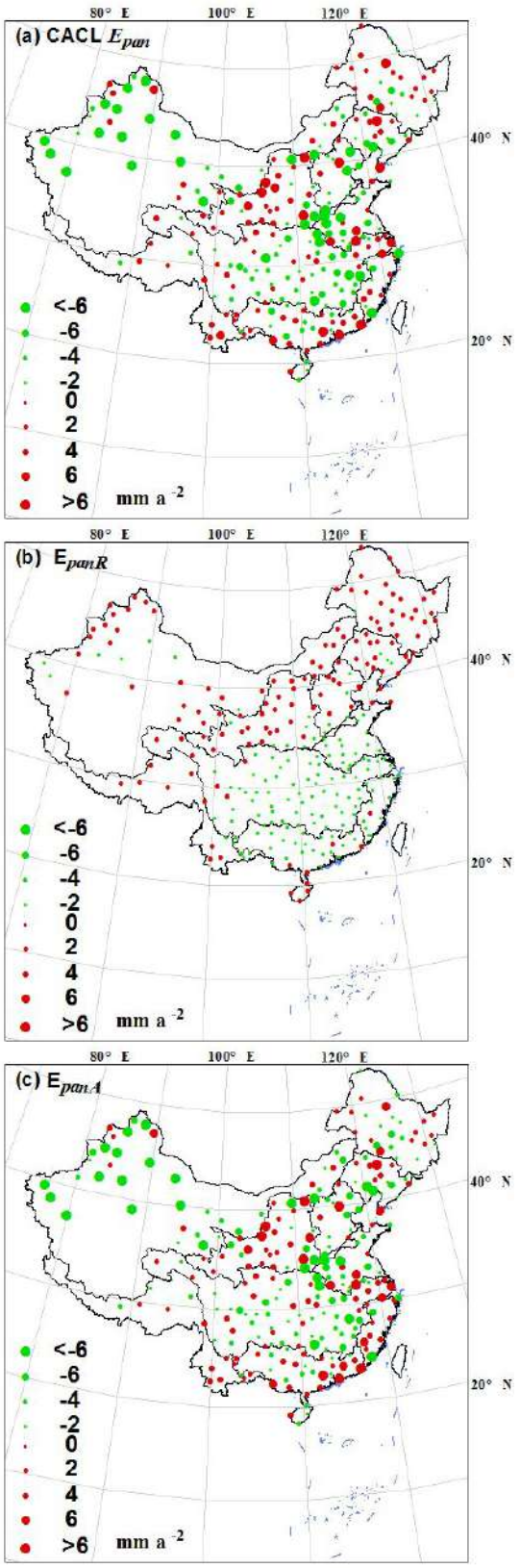

DOI: https://doi.org/10.30564/hsme.v2i2.2266

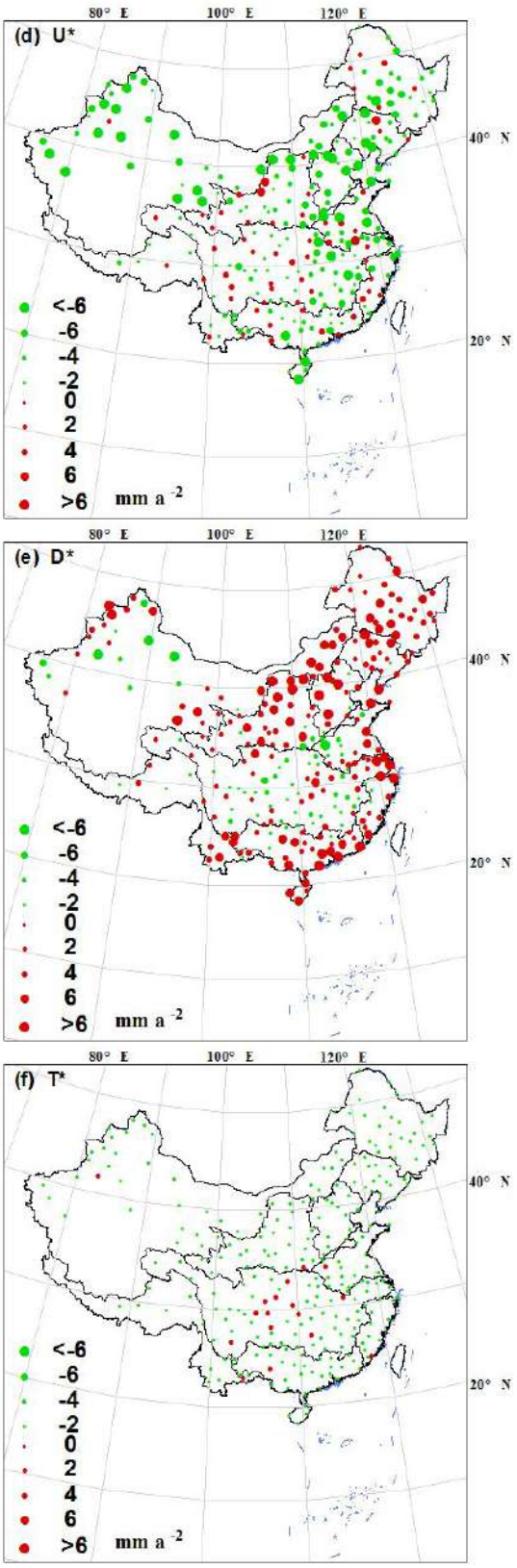

Figure 5. Trends in simulated pan evaporation and its components at 266 stations for the period 1959-2000. (a) Calculated E_{pan} rate. (b) Radiative component of pan evaporation ($E_{pan,R}$) rate. (c) Aerodynamic component of pan evaporation ($E_{pan,A}$) rate. The trends in the aerodynamic component are further partitioned into the change due to (d) U*, (e) D*, and (f) T*. The change in each panel, averaged across all 266 stations is (a) -1.11 mm a^{-2}, (b) -0.06 mm a^{-2}, (c) -1.06 mm a^{-2}, (d) -2.51 mm a^{-2}, (e) +1.69 mm a^{-2}, and (f) -0.33 mm a^{-2}

4. Discussion

4.1 Changes in Temporal Trends in Wind Speed

As addressed in Figure 3a, wind speed presented stilling phenomenon at 77% (205/266) stations across China with an average temporal trends at -0.011 m s^{-1} a^{-1}. Across China, in agreement with our study, downward trends in *u* [4,19-23] have been widely reported. Similar decreasing trends from -0.004 m s^{-1} a^{-1} to -0.017 m s^{-1} a^{-1} in near-surface *u* have been widely observed across the globe over the last 30-50 years (i.e., since ~1960s to ~1980s) for a range of mid-latitude regions (McVicar *et al*. [3] their Table 4). As showed in Figure 2 and Figure 3a, large declines were found in northern China, while central and south-central China have the least change in *u*. Except for Tibetan Plateau, the results are consistent with report by Guo *et al*. [4]. The precise cause of the stilling is uncertain [5], the explained for this phenomena lies in two aspects: (1) changes of land surface roughness (e.g., increasing vegetation cover and urbanization); and (2) influences resulting from the climate changes (e.g., weakening of the East Asian winter and summer monsoons). E.g., Guo *et al*. [4] stratified China 652-station database into rural and large-urban cases, and deduced that urbanization strengthened *u*. While Li *et al*. [24], using 12 stations to study the greater Beijing Area during 1960-2008, suggested that urbanization contributed one-fifth of the regional mean declining trend about −0.05 m s^{-1} $(10\ a)^{-1}$, and also noted that changes in strong winds (i.e., wind extremes and winter winds) are influenced by large-scale climatic change. As pointed by Chen *et al*. [25], the warm and cold Arctic Oscillation and El Nino-Southern Oscillation phases have significant influence on probability distribution of wind speeds, and thus internal climate variability is a major source of both interannual and long-term variability. The weakening of the East Asian winter and summer monsoons is the cause for the distinct decreases of wind speed over the whole China [21,23]. Furthermore, sharp step in *u* correspond well with the positive and negative phases of the interdecadal Pacific oscillation [22].

 DOI: https://doi.org/10.30564/hsme.v2i2.2266

4.2 Aerodynamic Effects of the Stilling in Wind Speed

Changes in E_{pan} caused by aerodynamics changes are larger than that caused by radiative components in most of regions of China (8 of 10) (Table 1). Declines in *u* play an important role in controlling the changes in $E_{pan,A}$ than that resulting from vapour pressure deficit and air temperature (Showed in Figure 5 and Table 1). Consistent with our results, changes in *u* is the main cause for changes in $E_{p,}$ [26], E_{pan} [19] and ET_0 [27] in China due to its significant downward trend and high sensitivity. Stilling reduced E_{pan} [1, 28, 29], ET_0 [30] and ET_p [31] rate, and has been regarded as important factor in explaining E_{pan} paradox [1,3], which means it is important to consider all four primary meteorological variables (being *u*, atmospheric humidity, radiation and T_a) [3]. As *u* exerting greater influence on energy-limited water yielding catchments than water-limited ones, it is vital to incorporate other factors to assess the impacts of evaporation demand on long term water resources [3]. Changes in *u* combining with other meteorological variables led to larger changes in E_{pan} in water-limited regions in northwest and North China (i.e., NWRB, SRB, LRB and HHRB) than that in energy-limited regions in South and central China (i.e., YzRB, PRB, SWRB and SERB) (showed in Table 1 and Figure 5). That indicated it is really hard to define the influence for the changes in *u* on water resources when involving the actual evapotranspiration and streamflow in different regions. As pointed by McVicar *et al*. [32], impacts of stilling on actual evapotranspiration and streamflow are situation dependent.

5. Conclusion

Changes of *u* during 1959-2000 from 266 stations across China presented an average decreasing trend of -0.012 m s^{-1} a^{-1}. There are 154 (among 205 negative trends stations) stations presenting significant decreasing trends at 99% confidence level while only 19 (among 61 positive trends stations) stations presenting significant increasing trends at 99% confidence level. Stilling in China was similar to the decrease reported over other terrestrial surface, which can explain the evaporation paradox.

Using a fully physical model (the improved Penpan model), we assessed the E_{pan} trends, and then quantified the aerodynamic effects resulting from the *U**, *D** and *T**. Stilling was the main cause for controlling the trends in E_{pan} in most of part of China, especially in the west and north of China. Our results suggest that stilling can reduce evaporation demand, and inevitably alter the water resources especially in the energy-limited regions, which should be put to further investigation incorporating with other factors.

Acknowledgments

This research was supported by the National Key Basic Research and Development Project (No. 2017YFC0404505, 2016YFC0500402), and the National Natural Science Foundation of China (No. 51579008), and Beijing Municipal Science and Technology Project (No: 217300011). Thanks to the National Meteorological Information Center, China Meteorological Administration, for offering the meteorological data.

References

[1] Roderick, M.L., Rotstayn, L.D., Farquhar, G.D., Hobbins, M.T. On the attribution of changing pan evaporation. Geophysical Research Letters, 2007, 34: L17403.
DOI: 10.1029/2007GL031166

[2] McVicar, T.R., Van Niel, T.G., Roderick, M.L., Li, L.T., Mo, X.G., Zimmermann, N.E., Schmatz, D.R. Observational evidence from two mountainous regions that near-surface wind speeds are declining more rapidly at higher elevations than lower elevations: 1960-2006. Geophysical Research Letters, 2010, 37: L06402.
DOI: 10.1029/2009GL042255

[3] McVicar, T.R., Roderick, M.L., Donohue, R.J., Li, L.T., Van Niel, T.G., Thomas, A., Grieser, J., Jhajharia, D., Himri, Y., Mahowald, N.M., Mescherskaya, A.V., Kruger, A.C., Rehman, S., Dinpashoh, Y. Global review and synthesis of trends in observed terrestrial near-surface wind speeds: Implications for evaporation. Journal of Hydrology, 2012a, 416-417: 182-205.

[4] Guo, H., Xu, M., Hu, Q. Changes in near-surface wind speed in China: 1969-2005. International Journal of Climatology, 2011, 31(3): 349-358.

[5] Vautard, R., Cattiaux, J., Yiou, P., Thépaut, J.-N., Ciais, P. Northern hemisphere atmospheric stilling partly attributed to increased surface roughness. Nature Geoscience, 2010, 3 (11): 756-761.

[6] Lim, W.H., Roderick, M.L., Hobbins, M.T., Wong, S.C., Groeneveld, P.J., Sun, F.B., Farquhar, G.D. The aerodynamics of pan evaporation. Agricultural and Forest Meteorology, 2012, 152: 31-43.

[7] Lim, W.H., Roderick, M.L., Farquhar, G.D. A mathematical model of pan evaporation under steady state conditions. Journal of Hydrology, 2016, 540: 641-658.

[8] Kohler, M.A., Noredenson, T.J., Fox, W.E. Evaporation from Pans and Lakes. US Weather Bureau Research Paper 38. US Weather Bureau, Washington, D.C, 1955.

DOI: https://doi.org/10.30564/hsme.v2i2.2266

[9] Allen, R.G., Pereira, L.S., Raes, D., Smith, M. Crop evapotranspiration-Guidelines for computing crop water requirements. FAO Irrigation and Drainage Paper 56, Rome, Italy, 1998.

[10] Roderick, M.L., Farquhar, G.D. The cause of decreased pan evaporation over the past 50 years. Science, 2002, 298: 1410-1411.
DOI:10.1126/science.1075390-a

[11] Qian, Y., Kaiser, D.P., Leung, L.R., Xu, M. More frequent cloud-free sky and less surface solar radiation in China from 1955 to 2000. Geophysical Research Letters, 2006, 33: L01812.
DOI: 10.1029/2005GL024586

[12] Shen, Y.J., Liu, C.M., Liu, M., Zeng, Y., Tian, C.Y. Change in pan evaporation over the past 50 years in the arid region of China. Hydrological Processes, 2010, 24(2): 225-231.

[13] Liu, X.M., Luo, Y.Z., Zhang, D., Zhang, M.H., Liu, C.M. Recent changes in panevaporation dynamics in China. Geophysical Research Letters, 2011a, 38: L13404.
DOI: 10.1029/ 2011GL047929

[14] Liu, X.M., Zheng, H.X., Zhang, M.H., Liu, C.M.. Identification of dominant climate factor for pan evaporation trend in the Tibetan Plateau. Journal of Geographical Sciences, 2011b, 21(4): 594-608.

[15] Zhang, Q., Qi, T.Y., Li, J.F., Singh, V.P., Wang, Z.Z. Spatiotemporal variations of pan evaporation in China during 1960-2005: changing patterns and causes. International Journal of Climatology, 2015, 35: 903-912.

[16] Rotstayn, L.D., Roderick, M.L., Farquhar, G.D. A simple pan-evaporation model for analysis of climate simulations: Evaluation over Australia. Geophysical Research Letters, 2006, 33: L17715.
DOI: 10.1029/2006GL027114

[17] Linacre, E.T. Estimating United States Class-A pan evaporation from few climate data. Water International, 1994, 19(1): 5-14.

[18] Thom, A. S., Thony, J. L., Vauclin, M. On the proper employment of evaporation pans and atmometers in estimating potential transpiration, Quarterly Journal of the Royal Meteorological Society, 1981, 107: 711-736.

[19] Yang, H., Yang, D. Climatic factors influencing changing pan evaporation across China from 1961 to 2001. Journal of Hydrology, 2012, 414-415:184-193.

[20] Xie, H., Zhu, X., Yuan, D.Y. Pan evaporation modelling and changing attribution analysis on the Tibetan Plateau (1970-2012). Hydrological Processes, 2015, 29: 2164-2177.

[21] Xu, M., Chang, C.P., Fu, C.B., Qi, Y., Robock, A., Robinson, D., Zhang, H.M. Steady decline of East Asian monsoon winds, 1969-2000: evidence from direct ground measurements of wind speed. Journal of Geophysical Research-Atmospheres , 2006c, 111: D24111.
DOI: 10.1029/2006JD007337

[22] Fu, G.B., Yu, J.J., Zhang, Y.C., Hu, S.S., Ouyang, R.L., Liu, W.B. Temporal variation of wind speed in China for 1961-2007. Theoretical and Applied Climatology, 2011, 104(3-4): 313-324.

[23] Jiang, Y., Luo, Y., Zhao, Z.C. Maximum wind speed changes over China. Acta Meteorologica Sinica,, 2013, 27(1): 63-74.

[24] Li, Z., Yan, Z.W., Tu, K., Liu, W.D., Wang, Y.C. Changes in wind speed and extremes in Beijing during 1960-2008 based on homogenized observations. Advances Atmospheric Sciences, 2011, 28(2): 408-420.

[25] Chen, L., Li, D., Pryor, S.C. Wind speed trends over China: quantifying the magnitude and assessing causality. International Journal of Climatology, 2013, 33(11): 2579-2590.

[26] Zhang, C., Liu, F., Shen, Y. Attribution analysis of changing pan evaporation in the Qianghai-Tibetan Plateau, China. International Journal of Climatology, 2018, 38 (Suppl. 1): e1032-e1043.

[27] Yin, Y. H., Wu, S. H., Chen, G., Dai, E. F. Attribution analyses of potential evapotranspiration changes in China since the 1960s. Theoretical and Applied Climatology, 2010, 101(1-2): 19-28.

[28] Rayner, D.P. Wind run Changes: Dominant factor affecting pan evaporation trends in Australia. Journal of Climate, 2007, 20(14): 3379-3394.

[29] Roderick, M.L., Hobbins, M.T., Farquhar, G.D. Pan evaporation trends and the terrestrial water balance, I. Principles and observations. Geography Compass 3/2, , 2009: 746-760.

[30] Liu, Q., Yang, Z.F., Cui, B.S., Sun, T. The temporal trends of reference evapotranspiration and its sensitivity to key meteorological variables in the Yellow River Basin, China. Hydrological Processes, 2010, 24: 2171-2181.

[31] Donohue, R.J., McVicar, T.R., Roderick, M.L.. Assessing the ability of potential evaporation formulations to capture the dynamics in evaporative demand within a changing climate. Journal of Hydrology, 2010, 386: 186-197.

[32] McVicar, T.R., Roderick, M.L., Donohue, R.J., Van Niel, T.G. Less bluster ahead? Ecohydrological implications of global trends of terrestrial near-surface wind speeds. Ecohydrology, 2012b, 5(4): 381-388.

 DOI: https://doi.org/10.30564/hsme.v2i2.2266

BILINGUAL PUBLISHING CO.
Pioneer of Global Academics Since 1984

Hydro Science & Marine Engineering
https://ojs.bilpublishing.com/index.php/hsme

ARTICLE

Numerical Simulation of Flow over Stepped Spillways with Varying Step-Angle

Mohsen Nasrabadi[1*] Younes Aminpour[2]

1. Department of Water Science and Engineering, Arak University, Iran
2. Department of Hydraulic and Hydro-Environmental Engineering, Water Research Institute, Ministry of Energy, Tehran, Iran

ARTICLE INFO

Article history
Received: 1 September 2020
Accepted: 16 September 2020
Published Online: 30 October 2020

Keywords:
Stepped spillway
Numerical method
Step angle
Cavitation index

ABSTRACT

In the present study, the flow over the stepped spillway was numerically investigated by using Flow3D model. The effect of step angle on different properties of Nappe flow regime such as the water surface profile, location of free-surface aeration inception, Froude number at the spillway's toe, and pressure, flow velocity, air concentration and cavitation index were evaluated. The realizable k–ε was applied as the turbulence model, and Volume of Fluid (VOF) model was used to determine the free surface flow profiles of the spillway. The model was verified using experimental data. In order to investigate the different characteristics of Nappe flow regime, 17 numerical runs was designed, in which, four step angles, four flow discharge were considered to investigate the flow characteristics over the stepped spillway. The results indicated that the numerical model is well suited with the experimental data over the stepped spillway (RMSE = 0.147 and ARE = 6.9%). In addition, with increasing the step angles, the aeration inception point is generally moved downstream. By increasing the step angles from zero to 10 degrees, the Froude number does not change significantly, however, at the angle of 15 degrees, the Froude number decreases by about 42 percent.

1. Introduction

Stepped spillways are the direct spillways that the weir crest is connected by successive steps to the spillway's toe. These spillways have a unique structure that results in a different flow structure than that of smooth spillways [1-4]. In general, the flow pattern over a stepped spillway can be divided into nappe flow, transition flow, and skimming flow. One of the important issues in the design of these type of spillways is the energy dissipation. Stepped spillways are used for dissipating the generated energy through the spillway, which reduces the dimensions of the stilling basin. In this regards, different researchers, including Sorensen (1985).[1], Christodoulou [5], Chen et al. [6], Chinnarasri and Wongwises [7], Gonzalez et al. [8], Felder and Chanson [9], Zare and Doering [10], Otun et al. [11], Aras and Berkun [12], and Munta and Otun [13] have studied the effect of the flow pattern, step roughness, step size, and slope of a stepped spillway on the energy dissipation.

One of the important issues in the design of stepped spillways is the cavitation phenomenon. Typically, in dif-

**Corresponding Author:*
Mohsen Nasrabadi,
Assistant Prof., Department of Water Science and Engineering, Arak University, Iran;
Email: m-nasrabadi@araku.ac.ir

DOI: https://doi.org/10.30564/hsme.v2i2.2341

ferent types of spillways and weirs, as the flow velocity exceeds a critical value, the structure is subject to the cavitation, in which, the evaporation is occurred due to the reduction in the local pressure at a constant temperature. Cavitation is one of the important issues that has always been of interest to designers and researchers in the design of hydraulic structures, either in closed systems (including pumps and turbines) or in open-flow systems (such as tunnels, dams, spillways, etc.). In order to prevent the cavitation, it is necessary to identify the locations of the points, in which, by increasing the flow velocity the pressure can be reduced up to the vapor pressure. Cavitation damage is associated with many factors and parameters, including cavitation index (σ), flow velocity (V), surface strength of structural materials (S), operation period, air concentration (C). In this regard, a criterion, called the cavitation index (σ_c), is used, as follows:

$$\sigma_c = \frac{p_0 - p_v}{\rho u^2 / 2} \tag{1}$$

where, p_0 is local pressure, p_v is the vapor pressure at a given temperature, u is the flow velocity. The cavitation occurs when σ is smaller or equal to σ_c. This critical value depends largely on the flow geometry, shape, and height of the surface roughness. According to Falvey (1990)'s study [14], the cavitation will not occur over the stepped spillways until $\sigma > 1.8$. In addition, the cavitation is considered as a serious problem when the flow velocity reaches 25 m/s. According to previous studies, there is a risk of cavitation for flow rates greater than 80 m^2/s. In principle, the cavitation index in the stepped spillways is high, and if it is not protective against cavitation, its critical discharge is more than 15 m^2/s.

The complex nature of the flow over the spillways has made it difficult to conduct a comprehensive numerical analysis. Numerous researchers have numerically investigated flow over the stepped spillways. Savage and Johnson [15] used Reynolds's averaged equations for flow analysis using Flow3D software. They used the FAVOR method for rigid boundary modelling and the VOF model for the free surface. Tabara et al. [16] simulated the flow over the stepped spillways by ADINA software. In this study, two types of step sizes and four different layouts were considered. The parameters of velocity, measured pressure and free surface profile were simulated using Volume of Fluid (VOF) method. Chinnarasri and Wongwises [7] investigated the flow over a stepped spillway with sloping steps and developed some equations for minimum critical depth for formation of a continuous flow and maximum critical depth for skimming flow regime in a simple and sloping stepped spillways. Kositgittiwong et al. [17] analysed the velocity profiles over the stepped spillways using CFD simulations and large-scale laboratory experiments. They considered five different turbulence models of the Standard k-ε, the Realizable k-ε, the Renormalization group k-ε, the Standard k-ω and the shear stress transport k-ω model. The results showed that the numerical model involving any of these turbulence models can satisfactorily simulate the velocity profiles. All five turbulence models performed satisfactorily well on large-scale stepped spillways. The k-ω models may be slightly better suited in the lower region, while the realizable k-ε model provided slightly better results in the upper part of the velocity profile. Rafi et al. [18] evaluated the effects of increased reservoir conservation level on velocities, discharge capacity, and cavitation risk of the spillway. They used mathematical model to estimate the flow velocities and cavitation risk. Shahheydari et al. [19] investigated numerically the flow over the stepped spillway using Flow3D software. They used RNG k-ε model as the turbulence model, and Volume of Fluid (VOF) model to determine the free surface flow profiles. They designed 112 numerical spillway models (96 stepped spillway models and 16 smooth spillway models (i.e., WES profile)) in order to investigate the various features of skimming flow regime. They considered two step sizes, six configuration, four discharge and four profile slopes (15, 30, 45, and 60 degrees) with various relative discharges to investigate the energy dissipation and discharge coefficient. Their results indicated that the discharge coefficient and energy dissipation have inverse relationship. Also by increasing the relative discharges, the energy dissipation decreased and discharge coefficient increased. Dursun & Ozturk [20] studied the energy dissipation ratio and inception point location of stepped spillways with and without end sills using computational fluid dynamic (CFD) methods. Flow characteristics and air inception points were determined for slope angles of 30°, 40° and 50°. It was found that the length of the non-aerated flow region was closely related to energy dissipation. In addition, the flow characteristics of the stepped spillways can be reliably determined by using CFD analysis. Bai et al. [4] studied the pressure distributions of three types of stepped spillways with different horizontal face angles in fully developed skimming flow regions. They used horizontal surfaces of V-shaped steps and inverted V-shaped steps. They concluded that negative pressures on the vertical surfaces of V-shaped, inverted V-shaped and traditional stepped spillways occurred near the sidewalls, near the axial plane and along the entire cross-section, respectively. For all the stepped spillways studied. They found that the minimum pressure decreased

 DOI: https://doi.org/10.30564/hsme.v2i2.2341

with increasing Froude number and increasing absolute values of the horizontal face angles.

Chinnarasri et al. [21] simulated numerically the flow behaviour through smooth and stepped spillways using a multiphase flow model with the realizable k-ε model. Bayon et al. [22] developed the numerical models of the flow in the non-aerated region of stepped spillways using diverse turbulence closures and discretization schemes implemented in two CFD codes of Open FOAM and FLOW-3D. They employed partial VOF (Volume of Fluid) and "True" VOF (TruVOF) approaches to simulate the free surface. The standard, RNG and Realizable k-ω, in addition to the SST k-ω model, were used for turbulence closure. They concluded that the models with turbulence closures of the k-ω family provide nearly the same predictions for the mean flow velocity with maximum differences on average smaller than 1%. Regarding discretization schemes, the first-order upwind method provides predictions for the mean flow velocity which are not significantly different (within 6%) than those obtained with second-order counterparts. However, these differences can be larger when maximum values of turbulent kinetic energy (TKE) and dissipation rate of TKE at the step edges are compared. In spite of the fact that the TruVOF (FLOW-3D®) method does not account for the tangential stresses at the air-water interface, the differences in the tracking of the free surface position among this method and the Partial VOF method (OpenFOAM) were found to be smaller than 3% along the stepped spillway. Bai et al. [4] evaluated the pressure distribution of V-shaped stepped spillway using five turbulence models. They found a good agreement with physical values, however, the - model is slightly better than other turbulence models in simulating the pressure distribution of V-shaped stepped spillway. In addition, Wan et al. [23] evaluated the application of SPH method to investigate hydrodynamics and re-aeration over the stepped spillways. In the SPH method, the entrainment of dissolved oxygen (DO) was studied using a multiphase mass transfer SPH method for re-aeration. The numerical results were compared with the hydrodynamics data from Chanson and DO data from Cheng. Their simulation results showed that the velocity distribution and the location of free-surface aeration inception agree with the experimental results. Compared with the experimental results, the distribution of DO concentration over the stepped spillway is consistent with the experimental results. Their results showed that the two-phase DO mass transfer SPH model is reliable and reasonable for simulating the hydrodynamics characteristics and re-aeration process. Bai et al. [4] studied experimentally the flow pattern in a V-shaped stepped spillway. Their results indicated that the flow structure is completely different from that of a traditional stepped spillway. They used the k-ε turbulence model to investigate the flow structure.

Many previous studies have focused on stepped spillways, most of them considered the step size and arrangement, among other factors; few studies have investigated the variations in the step shape, especially, the step angle. Therefore, in this paper, the flow pattern of a stepped spillway with different step angle was numerically studied. Furthermore, important flow characteristics such as the water surface profile, location of free-surface aeration inception, Froude number at the spillway's toe, and pressure, flow velocity, air concentration and cavitation index were investigated based on a detailed comparison with a traditional stepped spillway. The results of the present study will help the engineers encountering with the design of the stepped spillways with high efficiency.

2. Materials and Methods

The geometry of the model includes a stepped spillway with the height of 4.5 m, crest length of 1.4 m, step height of 30 cm, step length of 50 cm and the number of 15 steps. To study the step angles, four different slopes of 0, 5, 10 and 15 degrees were created (Figure 1). Figure 1 shows the structure of the stepped spillway along with the location of free-surface aeration inception.

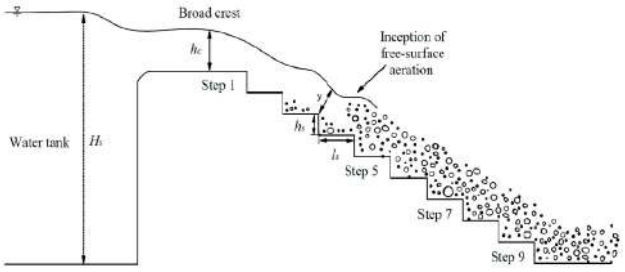

Figure 1. Structure of the stepped spillway [26]

In order to ensure the accuracy of the model results, one type of spillway made at the University of Ottawa's Lab Modeling was used and the results of a physical model were compared with a numerical model. To design the spillway, the USACE-WES design tables have been used in the Tabbara et al. (2005)'s study [16].

As an accurate and robust free-surface CFD package, FLOW-3D is an ideal tool for modeling the dam and spillway structures. FLOW-3D makes it easy to generate rating curves and detailed velocity profiles for complex spillways, including the effects of air entrainment and transport. This model also enables the quantification of structural stresses (pressure and shear forces) during normal and extreme operations, including transient effects due to gate operation. FLOW-3D is widely used to

DOI: https://doi.org/10.30564/hsme.v2i2.2341

confirm the hydraulic performance of proposed spillway designs and to help professionals meet dam safety requirements. The realizable k–ε turbulence model developed by Shih et al. [24] was used in this study, because it is useful for simulating the flow over the stepped spillways [25-26]. In addition, the air-water interface was simulated by the volume of fluid (VOF) method.

3. Verification Using Experimental Data

After obtaining the outputs of the numerical model for the flow discharge and water surface profile over the spillway, the numerical results were compared with the experimental data of Tabara et al. (2005) [16]. In this study, the water surface profile was determined using the Volume of Fluid method (VOF).

The values of the root mean squared error and average relative error were calculated using the Eqs. 2 and 3. Accordingly, the values of RMSE and MARE were equal to 0.147 and 6.9%, respectively, indicating that Flow-3D model has an appropriate ability to estimate the hydraulic parameters of the flow over the stepped spillways.

$$RMSE = \sqrt{(1/n)\sum_{i=1}^{n}\left(y_{i(\exp)} - y_{i(cal)}\right)^2} \tag{2}$$

$$\%MARE = 100/n\sum_{i=1}^{n}\left|\left(y_{i(\exp)} - y_{i(cal)}\right)/y_{i(\exp)}\right| \tag{3}$$

4. Results and Discussion

In order to investigate the effect of flow discharge, the simulations of this study were carried out with flow discharges (in unit width) of 1.157, 1.542, 1.928 and 2.313 m^2/s. Also, to ensure occurring the cavitation, the simulations were performed for two discharges of 6 and 12 m^2/s. In this study, in order to compare the results, the flow regime has been considered to be the same in all simulations. Table 1 shows the results of these analyses. According to the Essery and Horner (1978)'s [26] criteria, $(y_c/h > (y_c/h)_{onest}$, the flow regime is considered as Nappe flow in all the simulations.

$$\left(\frac{y_c}{h}\right)_{onest} = 1.57 - 0.465\frac{h}{l} \tag{4}$$

Figures 2 and 3 show the results of simulations performed on the stepped spillway with varying step angles of 0, 5, 10, and 15 degrees and different flow discharges. In these figures the fraction of entrained air are observed over the stepped spillway.

Table 1. The results of the analysis of the flow regime over the stepped spillway in this study

Run No.	Θ (degree)	Q (m^2/s)	y_{cp} (m)	H (m)	L (m)	(y_c/H)	$(y_c/H)c$
1	0	1.16	0.51	0.30	0.50	1.72	1.29
2		1.54	0.62	0.30		2.08	1.29
3		1.93	0.72	0.30		2.41	1.29
4		2.31	0.82	0.30		2.72	1.29
5		6.00	1.54	0.30		5.14	1.29
6	5	1.16	0.51	0.34		1.50	1.25
7		1.54	0.62	0.34		1.81	1.25
8		1.93	0.72	0.34		2.11	1.25
9		2.31	0.82	0.34		2.38	1.25
10	10	1.16	0.51	0.39		1.33	1.21
11		1.54	0.62	0.39		1.61	1.21
12		1.93	0.72	0.39		1.86	1.21
13		2.31	0.82	0.39		2.11	1.21
14	15	1.16	0.51	0.43		1.19	1.17
15		1.54	0.62	0.43		1.44	1.17
16		1.93	0.72	0.43		1.67	1.17
17		2.31	0.82	0.43		1.88	1.17

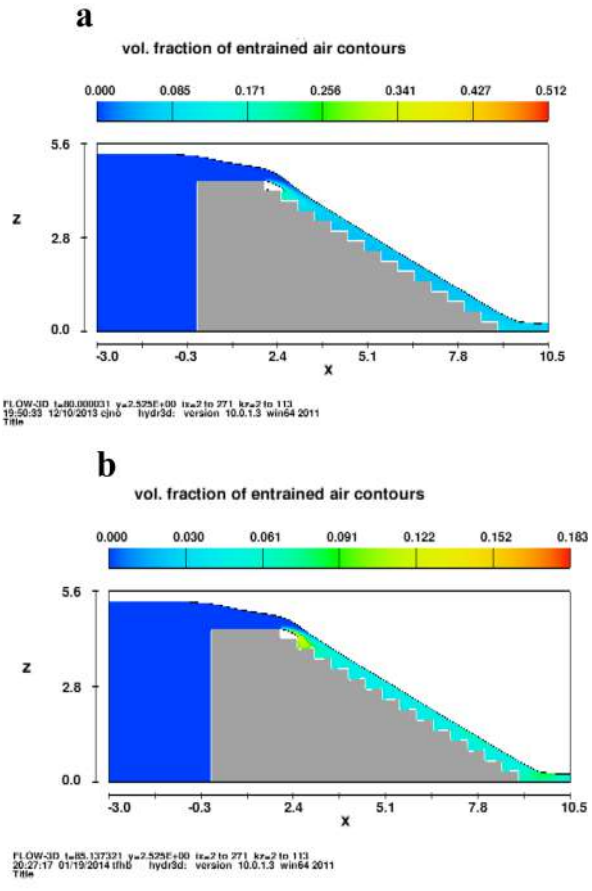

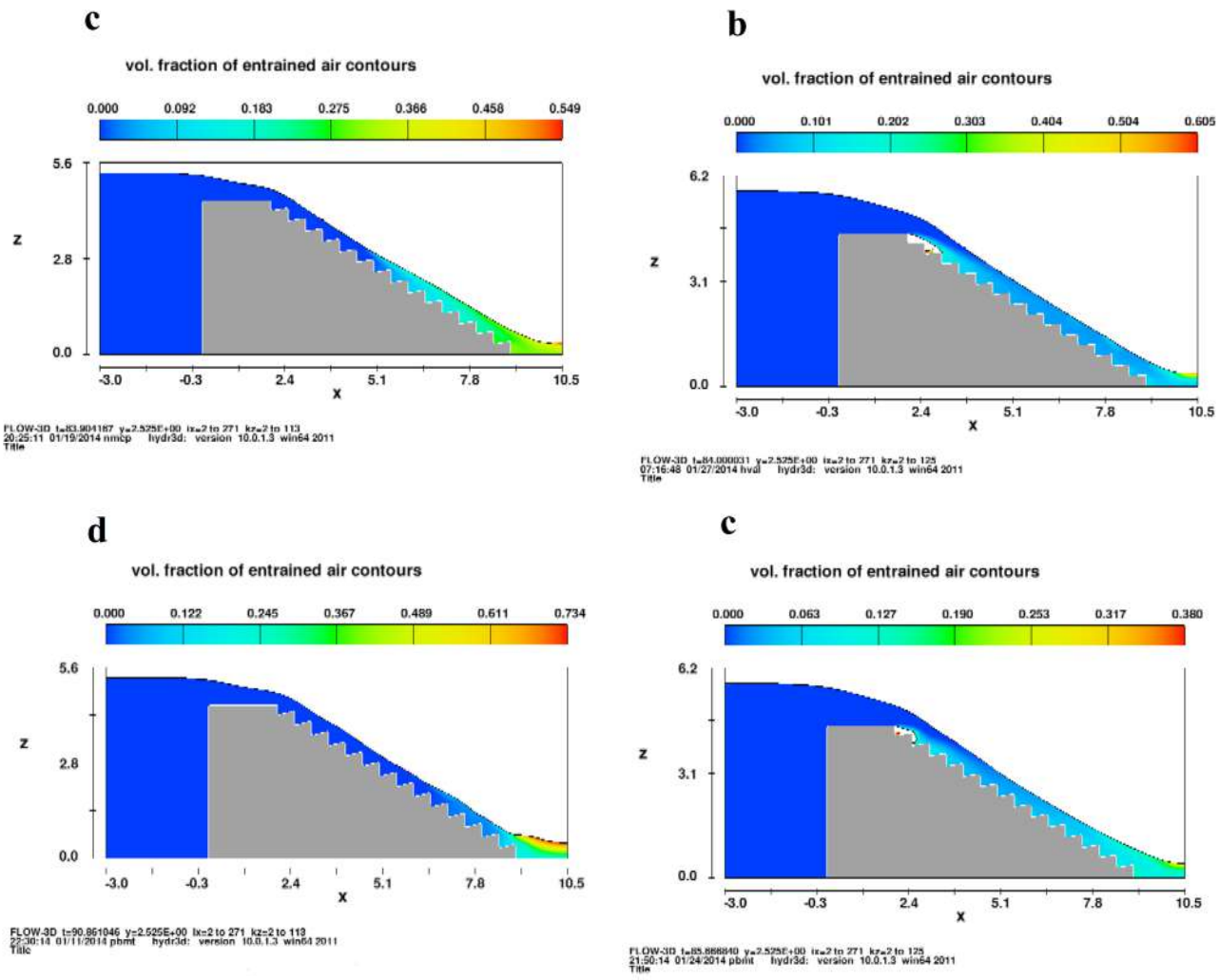

Figure 2. The results of numerical simulations for flow discharge of 1.157 m^2/s (a) θ = 0 (degree) (b) θ= 5 (degree) (c) θ = 10 (degree) (d) θ = 15 (degree)

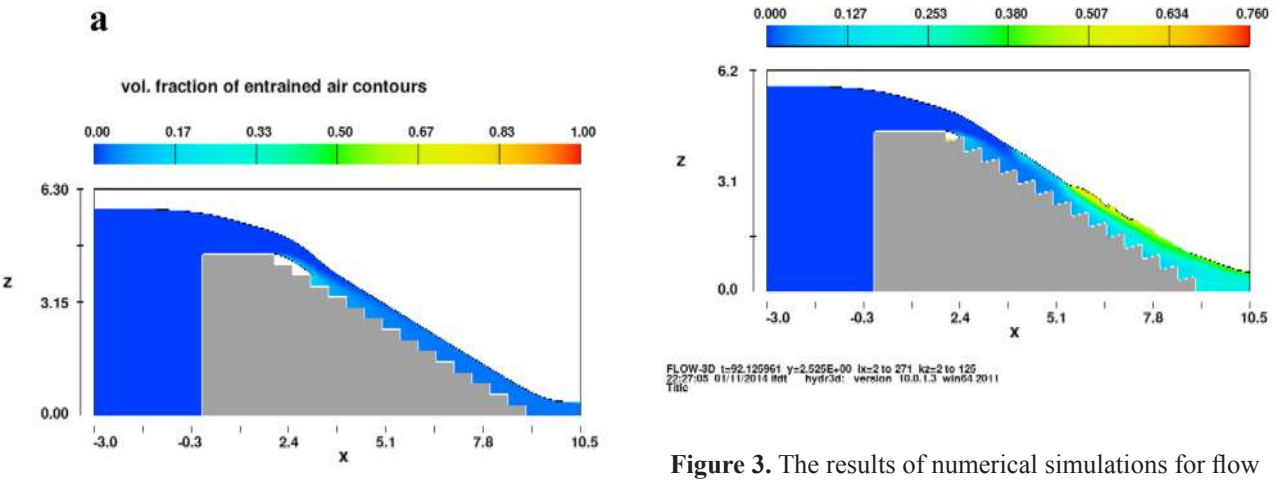

Figure 3. The results of numerical simulations for flow discharge of 2.313 m2/s (a) θ = 0 (degree) (b) θ= 5 (degree) (c) θ = 10 (degree) (d) θ = 15 (degree)

DOI: https://doi.org/10.30564/hsme.v2i2.2341

Using the simulation results, the effect of step angle are evaluated on such characteristics of the flow as the water surface profile, location of free-surface aeration inception, Froude number at the spillway's toe, and pressure, flow velocity, air concentration and cavitation index.

4.1 Water Surface Profile over the Stepped Spillway

The free surface of the flow are presented for the different step angles of 0, 5, 10, and 15 degrees in figure 4a and the flow discharge of 1.157 m^2/s (step angle of 15 degree) in figure 4b. As can be seen, the change in the step angles have a significant effect on the water surface profile in the middle steps and aerated region of the flow over the spillway. Increasing the step angles may increase the pseudo-bottom of the stepped spillway, and accordingly, this bottom will be rougher than the zero-degree step (Figure 4a-d).

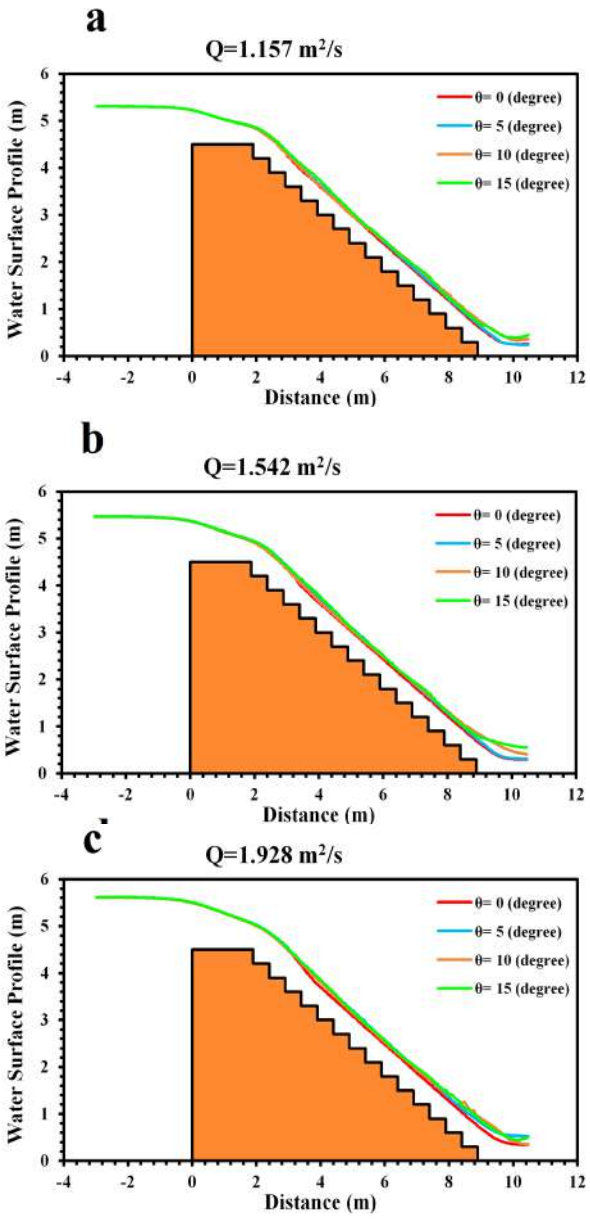

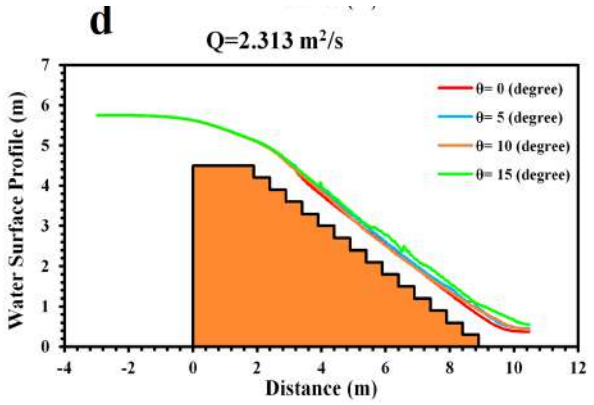

Figure 4. The effect of step angles on the water surface profile over the stepped spillway (a) Q= 1.157 m^2/s (b) Q= 1.542 m^2/s (c) Q= 1.928 m^2/s and (d) Q= 2.313 m^2/s

In addition, Figure 5 shows the simulated water surface profiles over the stepped spillway for a given step angle and different flow discharges.

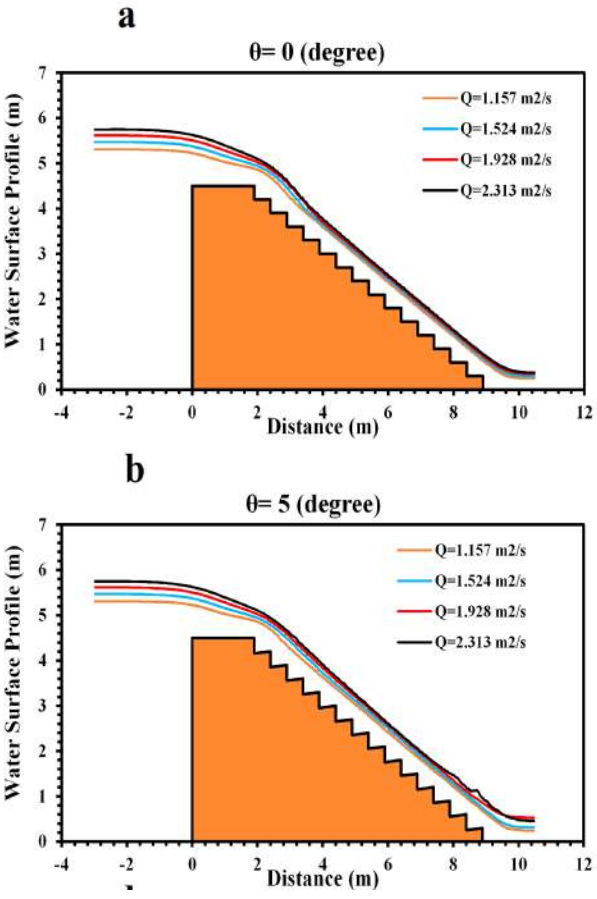

 DOI: https://doi.org/10.30564/hsme.v2i2.2341

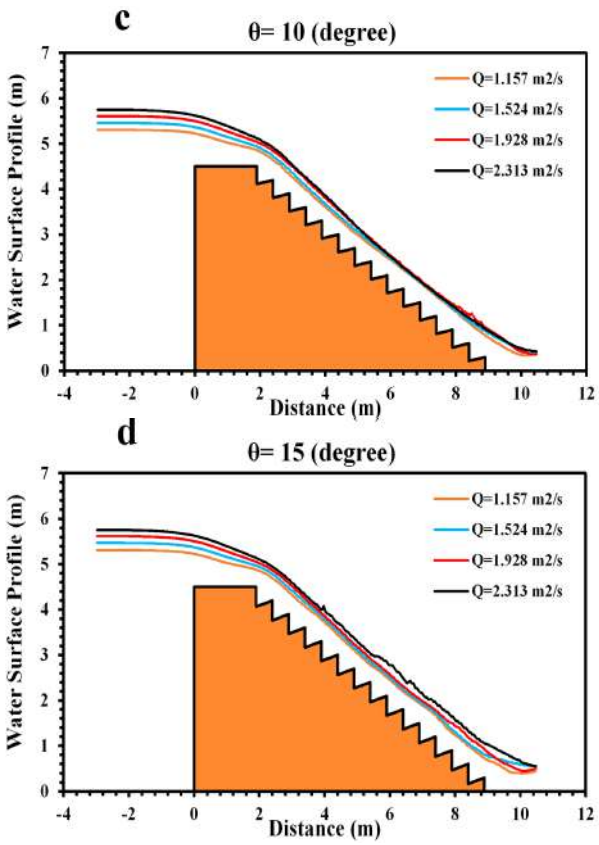

Figure 5. The effect of flow discharges on the water surface profile over the stepped spillway (a) θ = 0°, (b) θ = 5°, (c) θ = 10°, and (d) θ = 15°

4.2 Location of Free-Surface Aeration Inception

In this study, the location of free-surface aeration inception was recorded and determined by measuring the water surface level at the starting point of aeration along the centerline of the stepped spillway. The results showed that with the increase of the step angles, the aeration inception point is generally moved downstream. The reason for these changes is that by increasing the aeration inception, the effect of the steps is exacerbated as roughness elements and aeration process is intensified.

4.3 Froude Number at the Spillway's Toe

Given that the Froude number is an important factor in determining the dimensions of the stilling basin at the downstream of the spillway, the values of Fr_{dw} are plotted against the step angle for different flow discharges in Figure 6. As shown in this figure, by increasing the step angles from zero to 10 degrees, the Froude number does not change significantly, however, at the angle of 15 degrees, the Froude number decreases by about 42 percent. It can be stated that the angle, in which the lowest Froude number is observed, is about 15 degree for stepped spillway. In addition, it can be concluded that increasing the step angle may increase the dissipated energy at the downstream of the stepped spillways.

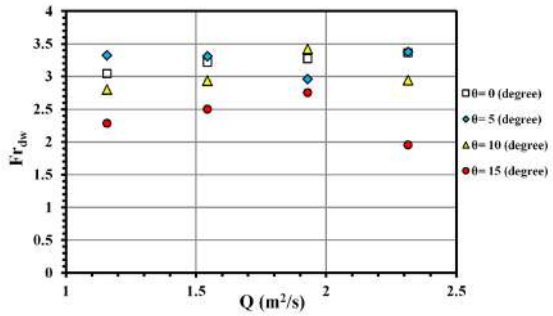

Figure 6. The values of Froude number at the toe of the stepped spillway for different flow discharges and step angles

4.4 Pressure Distribution

In order to investigate the effect of the step angle on the pressure variations on the spillway, the values of pressure over the spillway are plotted in Figure 7. As can be seen, the value of pressure on the initial steps is high, however, with increasing distance from the beginning of the spillway, the pressure decreases and reaches a constant value. In addition, increasing the flow discharge does not affect these changes, significantly.

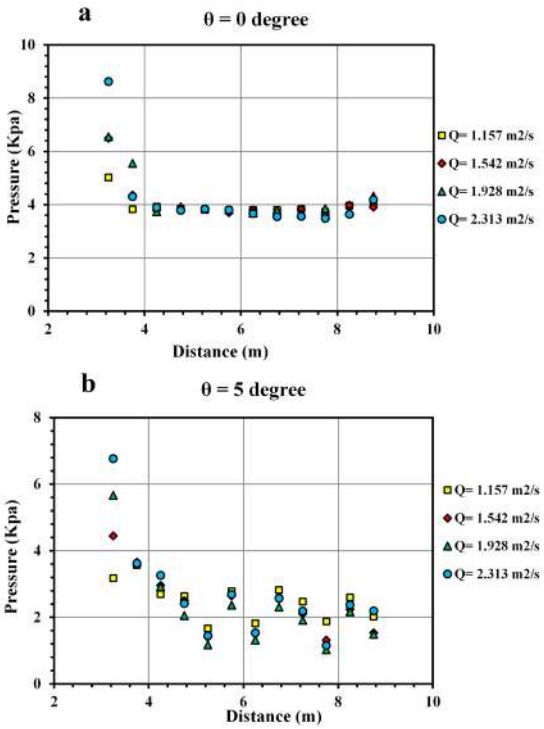

Figure 7. Pressure changes through the stepped spillway (a) θ = 0 (degree) (b) θ = 5 (degree)

DOI: https://doi.org/10.30564/hsme.v2i2.2341

4.5 Flow Velocity

Figure 8 shows the variations of mean velocity against the distance from the beginning of the spillway by increasing the step angle for two flow discharges of 1.157 to 2.313 m^2/s. It can be seen that with increasing the step angle, the average flow velocity for a given flow discharge will reduce the velocity will be disrupted and non-uniform. It can be concluded that increasing the step angle may lead to an increase in the height of the bed roughness, which will cause a loss and thus reduce the flow velocity. It is also observed in this figure that with increasing the step angle increase the bed roughness of the pseudo-bottom of the stepped spillway, and therefore, increase the flow resistance compared with the zero-degree stepped spillways.

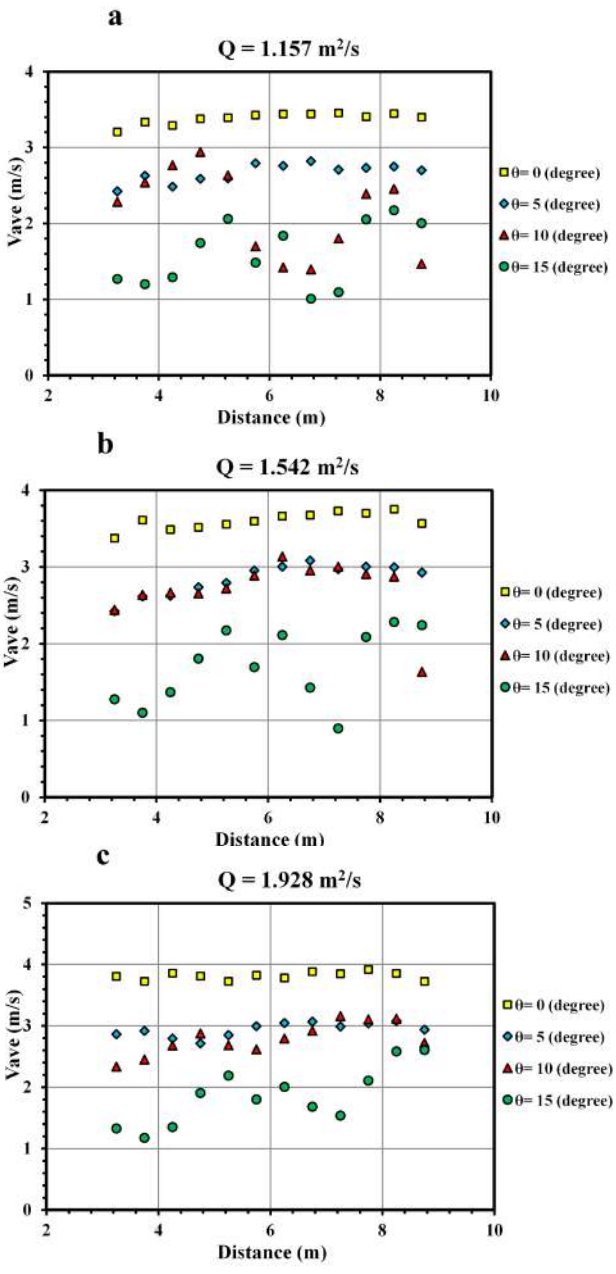

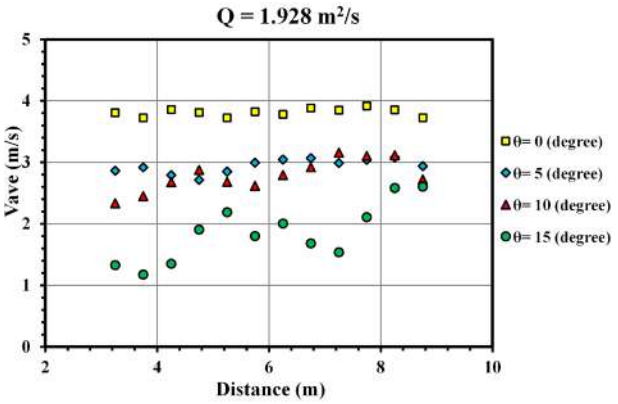

Figure 8. Changes in the mean flow velocity over the stepped spillway by increasing the step angles (a) Q = 1.157 m^2/s (b) Q = 1.542 m^2/s (c) Q = 1.928 m^2/s (d) Q = 2.313 m^2/s

4.6 Air Concentration

In order to investigate the effect of the step angles on the average air concentration over the stepped spillway, the air concentrations are plotted against the distance from the beginning of the spillway in figure 9. As can be seen, as the step angle increases, the air concentration in the initial steps decreases and for the end steps increases. The results showed that the average air concentrations increase significantly with the increase of distance from the beginning of the stepped spillway. So that the air concentration on the tenth step is about 4 to 8 percent and is 99 percent more than that of on the first step. This increase in air concentrations is associated with a reduction in the local pressure. It is also observed that the average air concentrations on the tenth step is about 36%, which increases by about 78% of the mean air concentration, compared to a concentration of 7.5% on the step with zero angle.

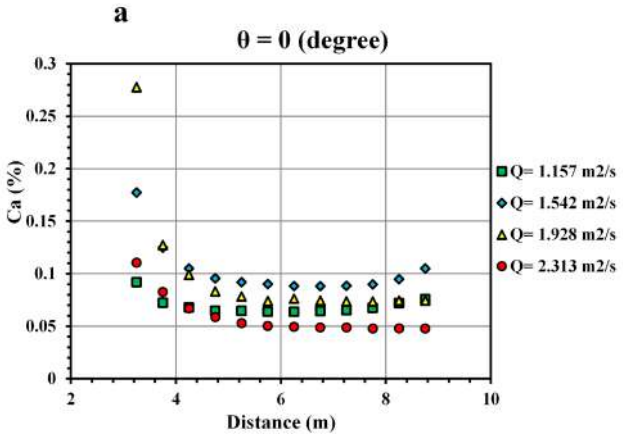

 DOI: https://doi.org/10.30564/hsme.v2i2.2341

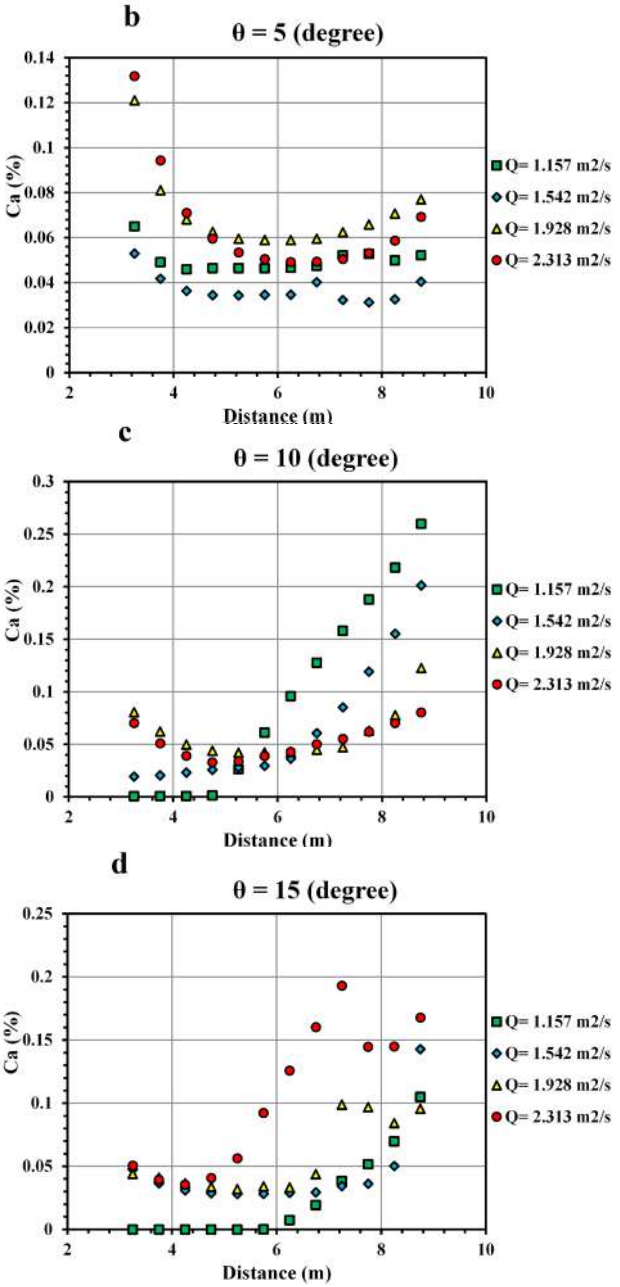

Figure 9. Variations of average air concentration over the stepped spillway by increasing step angles and flow discharges (a) θ= 0 degree (b) θ= 5 degree (c) θ= 10 degree (d) θ= 15 degree

4.7 Cavitation Index

In this study, the Falvey (1990)'s [14] criterion is used to investigate the occurrence of the cavitation phenomenon. Thus, the cavitation index was calculated using pressure and velocity values at different points in the stepped spillway. According to the Falvey (1990)'s [14] study, the cavitation will occur if the cavitation index is less than 1.8.

Figure 10 shows the values of the cavitation index against the distance from the beginning of the stepped spillway. As can be seen, the cavitation phenomenon does not occur in all the discharges and step angles, because this index is greater than 1.8. In general, with the changes in the index, it is possible to consider the occurrence of the cavitation phenomenon.

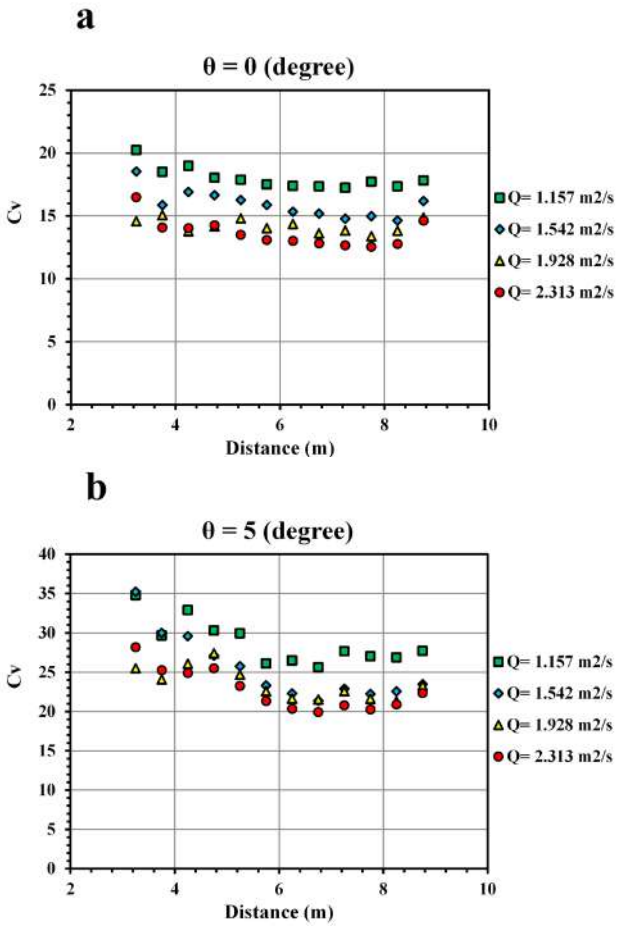

Figure 10. Variations of cavitation index over the stepped spillway

In the above figures, it is observed that as the flow discharge increases, the cavitation index decreases, therefore, the occurrence of the cavitation phenomenon can be increased. It can be concluded that by increasing the flow discharge and, as a result, the velocity, the amount of pressure decreases. Therefore, the value of cavitation index decreases.

In addition, figure 11 shows the variation of the cavitation index against the distance from the beginning of the stepped spillway by increasing the step angle. It can be seen that with increasing the step angle, the cavitation index increases. Accordingly, it can be concluded that increasing the step angle reduces the occur-

DOI: https://doi.org/10.30564/hsme.v2i2.2341

rence of the cavitation phenomenon. It can be said that with increasing the step angle, the flow velocity over the stepped spillway decreases and the flow pressure increases. These changes increase the amount of cavitation index.

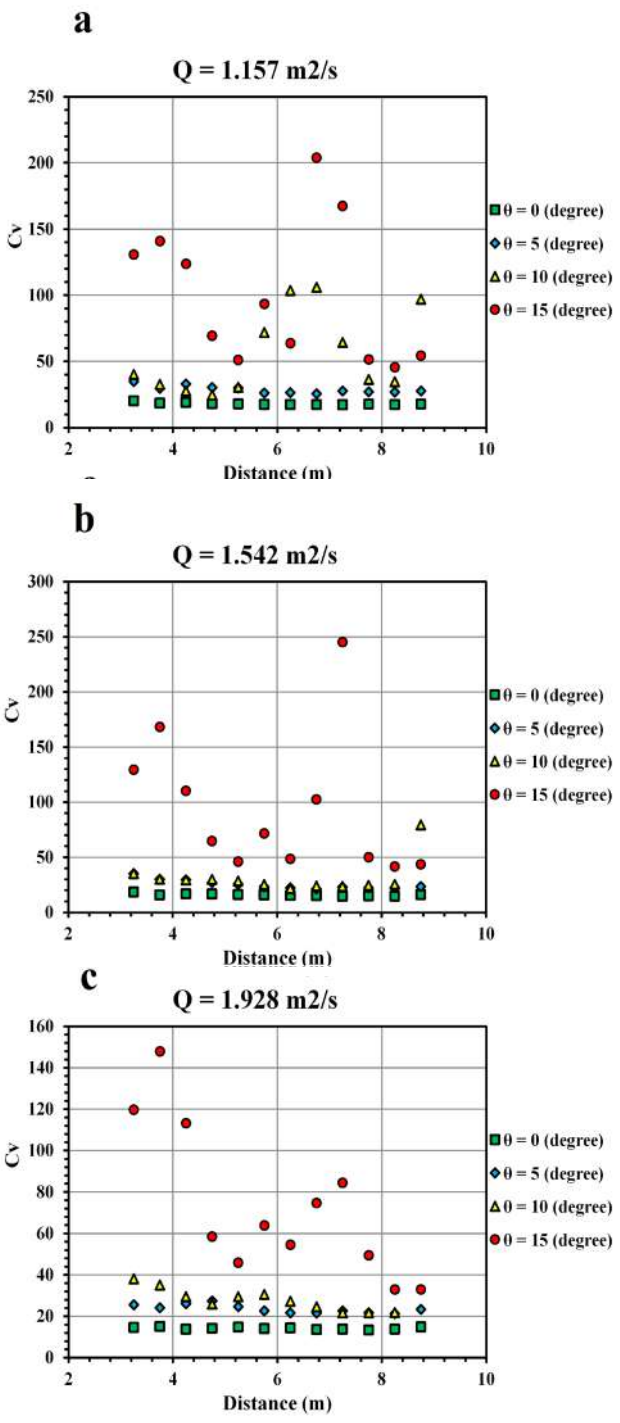

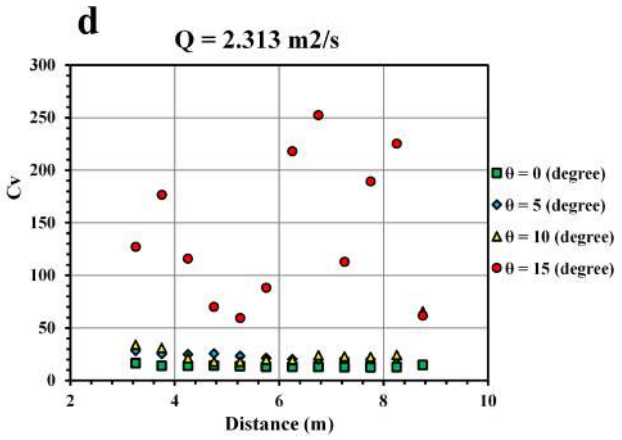

Figure 11. Changes in the cavitation index during the spillway by increasing the step angles (a) Q = 1.157 m^2/s (b) Q = 1.542 m^2/s (c) Q = 1.928 m^2/s (d) Q = 2.313 m^2/s

5. Conclusion

In this numerical study, the effect of step angle on the characteristics of the flow over the stepped spillways, consisting of water surface profile, location of free-surface aeration inception, Froude number at the spillway's toe, and pressure, flow velocity, air concentration and cavitation index, has been investigated. The major results of this study are:

(1) Validation of the results showed that the Flow3D model is very good in estimating hydraulic parameters, so that there was observed up to 7% error in the simulated water surface profile over the stepped spillway.

(2) The changes in the step angles have a significant effect on the water surface profile in the middle steps and aerated region of the flow over the stepped spillway.

(3) With the increase of the step angles, the aeration inception point is generally moved downstream. The reason for these changes is that by increasing the aeration inception, the effect of the steps is exacerbated as roughness elements and aeration process is intensified.

(4) By increasing the step angles from zero to 10 degrees, the Froude number does not change significantly, however, at the angle of 15 degrees, the Froude number decreases by about 42 percent.

(5) The value of pressure on the initial steps is high, however, with increasing distance from the beginning of the spillway, the pressure decreases and reaches a constant value. In addition, increasing flow discharge does not affect these changes, significantly.

(6) Increasing the step angle may lead to an increase in the height of the bed roughness, which will cause a loss and thus reduce the flow velocity.

(7) With increasing the step angles, the average air con-

 DOI: https://doi.org/10.30564/hsme.v2i2.2341

centration over the stepped spillway decreases.

(8) The cavitation phenomenon does not occur in all the discharges and step angles, because this index is greater than 1.8.

(9) As the flow discharge increases, the cavitation index decreases, therefore, the occurrence of the cavitation phenomenon can be increased. It can be concluded that by increasing the flow discharge and, as a result, the velocity, the amount of pressure decreases. Therefore, the value of cavitation index decreases.

References

[1] Sorensen, R. M. Stepped spillway hydraulic model investigation. Journal of Hydraulic Engineering, 1985, 111(12): 1461-72. https://doi.org/10.1061/(ASCE)0733-9429(1985)111:12(1461)

[2] Chen, Q., Guangqing, D., Haowu, L. Volume of fluid model for turbulence numerical simulation of stepped spillway overflow. Journal of Hydraulic Engineering, 2002, 128(7): 683-688. https://doi.org/10.1061/(ASCE)0733-9429(2002)128:7(683)

[3] Amador, A. M. S. J., Josep, D. Characterization of the nonaerated flow region in a stepped spillway by PIV. J. Fluids Eng., 2006, 128(6): 1266-1273. https://doi.org/10.1115/1.2354529.

[4] Bai, Z., Yurong, W., Jianmin, Z. Pressure distributions of stepped spillways with different horizontal face angles. the Proceedings of the Institution of Civil Engineers- Water Management, 2018, 171(6): 1-12. https://doi.org/10.1680/jwama.16.00093

[5] Christodoulou, G. C. Energy dissipation on stepped spillways. Journal of Hydraulic Engineering, 1993, 119(5): 644-650. https://doi.org/10.1061/(ASCE)0733-9429(1993)119:5(644)

[6] Chen, Q., Guang-Qing, D., Fen-Qin, Z. Influencing factors for the energy dissipation ratio of stepped spillways. Journal of Hydrodynamics, Series B, 2005, 17(1): 50-57.

[7] Chinnarasri, C., Wongwises, S. Flow patterns and energy dissipation over various stepped chutes. Journal of irrigation and drainage engineering, 2006, 132(1): 70-76. https://doi.org/10.1061/(ASCE)0733-9437(2006)132:1(70)

[8] Gonzalez, C. A., Masayuki, T., Hubert, C. An experimental study of effects of step roughness in skimming flows on stepped chutes. Journal of Hydraulic Research, 2008, 46(sup1), 24-35. https://doi.org/10.1080/00221686.2008.9521937

[9] Felder, S., Hubert, C. Closure to "Energy Dissipation down a Stepped Spillway with Nonuniform Step Heights. by Stefan Felder and Hubert Chanson", Journal of Hydraulic Engineering, 2012, 138(10): 921. https://doi.org/10.1061/(ASCE)HY.1943-7900.0000611

[10] Zare, H. K., John, C. D. Energy dissipation and flow characteristics of baffles and sills on stepped spillways. Journal of Hydraulic Research, 2012, 50(2): 192-9. https://doi.org/10.1080/00221686.2012.659840

[11] Otun, J. A., Munta, S., Adie, D.B. Modelling flow over stepped spillway with varying chute geometry. Nigerian Journal of Technology, 2012, 31(2): 206-12.

[12] Aras, E., Mehmet B. Effects of tailwater depth on spillway aeration. Water SA, 2012, 38(2): 307-12. https://doi.org/10.4314/wsa.v38i2.16

[13] Munta, S., Otun, J. A. Study of the Inception Length of Flow over Stepped Spillway Models. Nigerian Journal of Technology, 2014, 33(2): 176-83. https://doi.org/10.4314/njt.v33i2.6

[14] Falvey, H. T. Cavitation in chutes and spillways. US Department of the Interior, Bureau of Reclamation Denver, 1990.

[15] Savage, B. M., Michael, J. Flow over ogee spillway: Physical and numerical model case study. Journal of Hydraulic Engineering, 2001, 127(8): 640-9. https://doi.org/10.1061/(ASCE)0733-9429(2001)127:8(640)

[16] Tabbara, M., Jean C., Rita A. Computational simulation of flow over stepped spillways. Computers & Structures, 2005, 83(27): 2215-24. https://doi.org/10.1016/j.compstruc.2005.04.005

[17] Kositgittiwong, D., Chinnarasr, C., Julien, P. Y. Numerical simulation of flow velocity profiles along a stepped spillway. Proceedings of the Institution of Mechanical Engineers, Part E: Journal of Process Mechanical Engineering, 2013, 227(4): 327-35. https://doi.org/10.1177%2F0954408912472172

[18] Rafi, M., Akhtar, A., Ghulam, Q., Rafaquat, A. Modeling the Mangla dam spillway for cavitation and aerators optimization. Journal of Water Resource and Protection, 2012, 4(12): 1051. http://dx.doi.org/10.4236/jwarp.2012.412121

[19] Shahheydari, H., Jafari Nodoshan, E., Barati, R., Azhdary Moghadam, M. Discharge coefficient and energy dissipation over stepped spillway under skimming flow regime", KSCE Journal of Civil Engineering, 2015, 19(4), 1174-82. doi 10.1007/s12205-013-0749-3

DOI: https://doi.org/10.30564/hsme.v2i2.2341

[20] Dursun, O. F., Ozturk, M. Determination of flow characteristics of stepped spillways. The Proceedings of the Institution of Civil Engineers-Water Management, 2016, 169(1): 30-42. https://doi.org/10.1680/wama.14.00120

[21] Chinnarasri, C., Kositgittiwong, D., Julien, P. Y. Model of flow over spillways by computational fluid dynamics. The Proceedings of the Institution of Civil Engineers-Water Management, 2014, 167(3): 164-175. https://doi.org/10.1680/wama.12.00034

[22] Bayon, A., Toro, J. P., Bombardelli, F. A., Matos, J., and López-Jiménez, P. A. Influence of VOF technique, turbulence model and discretization scheme on the numerical simulation of the non-aerated, skimming flow in stepped spillways. Journal of hydro-environment research, 2018, 19: 137-49. https://doi.org/10.1016/j.jher.2017.10.002

[23] Wan, H., Li, R., Gualtieri, C., Yang, H., Feng, J. Numerical simulation of hydrodynamics and reaeration over a stepped spillway by the SPH method. Water, 2017, 9(8): 565. https://doi.org/10.3390/w9080565

[24] Shih, T. H., Liou, W. W., Shabbir, A., Yang, Z., Zhu, J. A new k-epsilon eddy viscosity model for high Reynolds number turbulent flows: Model development and validation. Computers & Fluids, 1994, 24(3): 227-238.

[25] Qian, Z. D., Hu X. Q., Huai W. X., Amador A. Numerical simulation and analysis of water flow over stepped spillways. Science in China Series E: Technological Sciences, 2009, 52(7): 1958-65. doi: 10.1007/s11431-009-0127-z

[26] Essery, I. T. S., Horner, M. W. The hydraulic design of stepped spillways, Report 33 Constr. Industry Res. and Information Assoc., London, England, 1978.

 DOI: https://doi.org/10.30564/hsme.v2i2.2341

BILINGUAL PUBLISHING CO.
Pioneer of Global Academics Since 1984

Hydro Science & Marine Engineering
https://ojs.bilpublishing.com/index.php/hsme

REVIEW

Impact of Past Mining Activities on Water Resources Around Active and Abandoned Mines and Quarries in Ebonyi State, South-Eastern Nigeria - A Mini Review

Moses Oghenenyoreme Eyankware* **Nnabo Paulinus Nwankwo** **Christopher Ogwah**

Department of Geology, Ebonyi State University, Abakaliki Ebonyi State, Nigeria

ARTICLE INFO

Article history
Received: 21 September 2020
Accepted: 13 October 2020
Published Online: 30 October 2020

Keywords:
Groundwater
Surface water
Southern Benue Trough
Acid mine drain
Nigeria

ABSTRACT

This paper presents a review on previous activities of mining on water resources around active and abandoned mines/quarries across Ebonyi State, South-Eastern, Nigeria. As high demand for water increases due to population growth and rapid development across the state, it is of upmost importance to periodically review water quality and also monitor water resources. However, less information is available on evaluation of impact on mining activities on water resources. For the purpose of this research, related articles were downloaded from Google, published article on effect of mining on water resources was download and thoroughly studied to evaluate effect of mining on water resources of the study area. Findings revealed that past mining activities has lead to chains of complex chemical reactions that has altered the quality of water resources.

1. Introduction

The southern portion of Benue Trough is richly blessed with various mineral deposits. These mineral deposits cuts across each zone of the study area ranges from: (1) lead-zinc at Abakaliki, Ameka, Amorie, Mkpuma Akpatakpa, Amanchara and Alibaruhu and Enyigba in the form of their ores of sphalerite and galena respectively often associated with barytes mineralization of the southern Benue Trough sediments that it is primarily made up of four lodes namely; Ishiagu, Ameri and Ameki Enyigba (Figure 1a) (2). the abandoned limestone quarry at Nkalagu area that occur within the Turonian age of the Eze-Aku Formation (Figure 1b) (3) Salt/Brine that occur within Cretaceous rocks at Uburu, Okposi and Abakaliki (4) limestone quarry that occur at Umuoghara and others. The open cast and underground mining is used in mining of the above listed minerals, the presence of these mineral has attracted attention of both local and international investors. Mining of these minerals date back to 1925 [1], for example, lead-zinc mineral was exploited by a German mining company before the Nigerian civil war. The company employed open cast mining and the galena and sphalerite were beneficiated at the site by differential floatation using xanthate collector [2]. Mining within the study area occur in large and small scale, these activities has left most mining areas with abandoned mines pits, whose ephemeral runoffs are captured by short-lived streams that flows into the river and infiltrate into aqui-

**Corresponding Author:*
Moses Oghenenyoreme Eyankware,
Department of Geology, Ebonyi State University, Abakaliki Ebonyi State, Nigeria;
Email: geomoses203@gmail.com

DOI: https://doi.org/10.30564/hsme.v2i2.2412

fer system. In the same vein, it has also caused series of ecohydrological and environmental problems, which have drawn attention from the public, the government and academia [3]. Previous scholar were of the view that mining activities within the study area has altered the quality of water resources and that of soil [4-10]. The effect of mining activities on water resources arise at different phase of the mining cycle, the mining processes, the mineral processing and operational stage. Globally, mining activities is one of the major activities that cause decline in water quality and most of the mining areas are faced with seious problems related to potable water both in terms of quantity and quality [11]. Generally, in the course of mining operation, huge quantities of water are generated and discharged into natural drainages without any beneficial use, leaving these areas as water deficit. In most cases, the discharged mine water were considered unsuitable for drinking purpose with presence of heavy metals that are in high concentrations, these mine water is referred to Acid Mine Drainage (AMD). [12] describe AMD as a chemical process developed due to oxidation of sulfide minerals under humid conditions, though it involves range of complex chemical reactions, geochemical, biochemical and physiochemical processes determined by local geology and geomorphology features. These processes often lead to acid mine generation alongside with several preventive and enhancing factors. [12] further pointed out that AMD is accepted as the principle water contaminant facing the mining industry. It is like a household name associated with different kind of mines. AMD can easier travel long distances causing a range of e ects that may persist for decades [8]. AMD in abandoned and active mine are influenced by several factors such as the hydrology, hydrogeology, mineralogy, geology, climate conditions and topography. It is related to the geographical conditions within the mine and is site specific. Research carried out within the area suggested that mining activities has greatly affected water quality within the mine and quarries areas [13-17], for more on this see Table 1. Although different scholar have carried out research around active and abandoned mines in Ebonyi, to best of our knowledge larger percentage of their research were geared towards assessment of effect of mining activity on soil and heavy metals released from mining activities with emphasis on its absorption/intake in human and its effect on human. The aim of this paper is to discuss a synoptic overview of effect of past mining activities on water resources of study area.

Figure 1a. Lead-zinc mine at Enyigba mining site

Figure 1b. Limestone quarry site at Nkalagu

Table 1. Previous research on mining activities and its effect on water resources around mines across the study area

Author(s)	Location	Geology	Field of study	Geochemical Characterization/Water type
[17]	Nkalagu	Asu River Group (ARG) / Eze Aku Formation (EAF)	Groundwater Analysis	(Cl^{-}-SO_4^{2-}) is the dominant facies
[8]	Ebonyi state	ARG/EAF	Groundwater Analysis	Ca^{2+} +Mg^{2+} + Cl^{-} (Water type)

 DOI: https://doi.org/10.30564/hsme.v2i2.2412

[18]	Umuoghara	ARG	Groundwater Analysis	$Ca^{2+}+Mg^{2+}+Cl^{-}$ (Water type)
[19]	Ameka	ARG/EAF	Groundwater and surface water analysis	Not specified
[13]	Mkpuma Ekwaoku	ARG	Groundwater and surface water analysis	Not specified
[15]	Mkpuma Ekwaoku	ARG	Groundwater Analysis	TH classification (Soft and hard water type)
[20]	(1)Akpala, Ohinya Ezza and Eziekwu river (2)Groundwater sample was collected at Ebia, Ogboji and Akaeze areas	ARG/EAF	Groundwater and surface water analysis	Not specified
[21]	(1)Okposi (2) Uburu	ARG/EAF	Groundwater and surface water analysis	Water resources were classified into three group: (1)Calcium bicarbonate (2) Sodium chloride and (iiii)Sodium/potassium bicarbonate
[23]	Amachara	ARG	Groundwater and surface water analysis	Rock water interaction (mineral dissolution)
[17]	Umuoghara	ARG	Groundwater	(1)Rock water intraction (2)$Ca^{2+}>Mg^{2+}>-Cl->SO_4^{2-}>Na^{+}+K+>HCO_3^{-}$ water trend (3)$Na^{+}-SO_4^{2-}$ **water type**
[10]	Enyigba, Mkpuma Akpatakpa, Ameka, Amorie, Amanchara and Alibaruhu.	ARG/EAF	Groundwater and surface water analysis	
[23]	Enyigba	ARG		Not specified

2. Location and Physiography

The study area is accessible through various networks of roads see Figure 2. The two major seasons that exist in the study area is the wet and dry seasons. The wet season spans from March to ending of October, while the dry season spans from October to ending of February, with temperature range of 25 and 29°C between the dry season and 16° and 28°C during the rainy season. While the average monthly rainfall ranges from 3.1 mm in January and 270 mm in July [8].The annual rainfall of the study area ranges from 1750 to 2250 mm. [8] was of the view that the climate of the area tends to support pollution from the mining and quarry activities. It was observed that surface runoff that transport the pollution and also assist infiltration of water is caused by high amount of rainfall. The study area lies within the rainforest region of southeastern Nigeria, with evergreen vegetation and humid climate. The area comprises of vegetation with underground creepers and thick trees in most rural areas [8]. Most of the trees are tall in some locations, with buttress roots around river bodies, while the vegetation is influenced by various factors these include; geology, drainage, rainfall and topography. [24], further pointed out that the study area lies within the low land rainforest region. The drainage system of the study area is dendritic, the major river that drain the study area is the Ebonyi River with other tributaries such as the Iyiodu and Ngada rivers control the drainage with the underlying lithology [8,16].

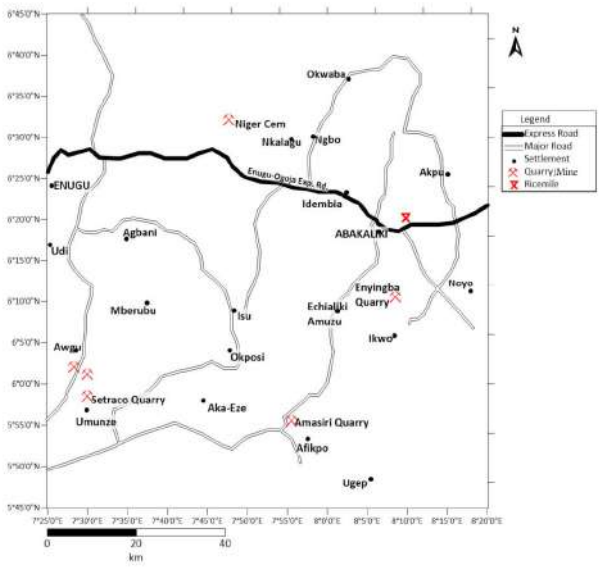

Figure 2. Location Map of Showing active and abandoned mine in the study area

3. Geology of the Study Area

The study area is lies within the southern Benue Trough with a sedimentary succession of pre-Santonian periods that span from Albian and Turonian age see Figure 3 and Table 1. The Asu River Group of the Albian age is represented by [25] with two formations Abakaliki and Ebonyi Formations that underlie it [26]. [26] stated that the lithofacies of Asu River Group consists of alternating shales and siltstones with presences of fine grained micaceous and feldspathic sandstones, mudstones, and limestones. [28]

DOI: https://doi.org/10.30564/hsme.v2i2.2412

were of the view that there have been reports of intrusions of magmatic rocks ranging from basic/intermediate igneous rock within the Ishiagu area. [29,30] also reported pyroclastic intrusions within the Abakaliki area. The Eze Aku Group is Turonian in age, according to [31] it unconformably overlies the Asu River Group in the study area. It includes all the lithostratigraphic units deposited in the late Cenomanian to Turonian age of the southern Benue Trough [31] which includes the the Nkalagu limestone, Eze-Aku shales and Amasiri sandstone. [32,33] were of the view that integration of magmatism, tectonism and diagenesis trigged major alteration of chemical constituents of rocks within the area, thereby baking them and leading to their common use as construction materials [34-36]. [37,38] stated that lead-zinc minerals occur in veins as open space-fillers within en echelon, tensional, and steeply dipping fracture systems and that in the dark-gray to black shales of the Asu River Group also encouraged their rampant excavation.

Table 1. Stratigraphic table of the study area (Modified after, [39])

Period	Age	Group	Formation	Member
Cretaceous	Tournian	Eze-Aku	Nkalagu Eze Aku shales	
	Albian	Asu River	Abakaliki Volacnics	Pycroclastics Dolerites/doiorities
			Asu River shales	Shales and sandstones
Precambrian Basement Complex				

4. Method of Investigation

Articles published within the last 4-10 years were reviewed to assess the effect of past mining activities around active and abandoned mines on water resources of the study area, and also to reduce water resource pollution. [40,41] methods was adopted for this study. Article related to this study were searched by google search engines, open access journal sites (SCOPUS, Pub-Med, Taylor Francis, Elsevier and Springer etc.). These relevant articles and papers were studied in full and information gotten was stored in the database with details of publication particulars, study location, period, approach, methodology for assessing past impact of mining activities as shown in Table 1. The results of impact past mining activities on water resources was captured, and conclusion drawn out. And further, to interpret the status and quality of research carried out within the study area, [40] method was employed for this study with some modifications to suit the aim and objectives of this paper. The steps that were adopted to evaluate the effect of mining and quarrying on water resource quality included the following;

(1) Evaluation of AMD/hydrogeochemical processes that influence water resource

(2) The type of water facies that exist within the study area.

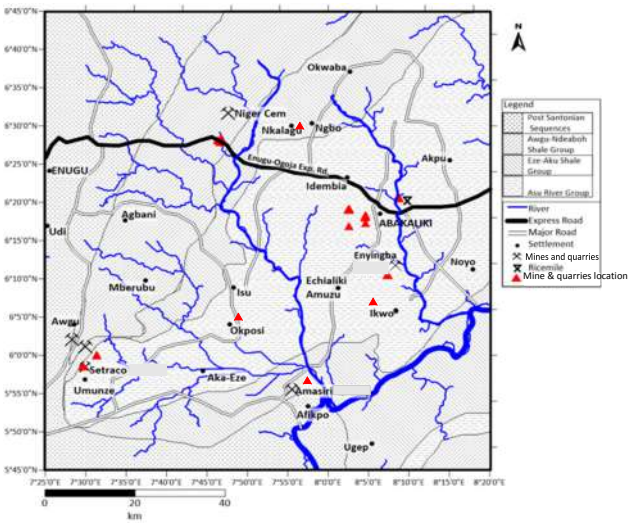

Figure 3. Geology Map of the Study Area

Source: [8]

5. Result and Discussion

The impact of past mining activities was evaluated by reviewing previous published literature within the area, with emphasis on hydrochemical processes and water quality.

5.1 Acid Mine Drainage and Hydrogeochemical Processes

For better understanding of impact of past mining activities/AMD on water resources within the study area, it is of upmost importance to first discuss briefly the geochemical processes that generate and neutralize acid drainage (summarized by [42], and references therein). [10] conducted a study on impact of lead-zinc mining on water resources of Enyigba, Mkpuma Akpatakpa, Ameka, Ameri, Amanchara and Alibaruhu. Water sample was collected within the area with the aim of evaluating its health risks on inhabitant of the area. Findings from their research revealed that lead concentration was high around active mines and they further attributed the high concentration of lead to mineralization process of lead. They also stated that pH fell within acidic to basic range, and that acidic water exist around the mine area and in turn contribute to AMD within the area. They were of the view that water resources of the area are considered unfit for domestic

 DOI: https://doi.org/10.30564/hsme.v2i2.2412

use. [8] investigated groundwater quality around active and abandoned mine across Ebonyi state, they stated that mining and quarrying activities generate AMD within active and abandon mines. Their findings pointed out that pH of groundwater within the area were considered more acidic than basic especially around mines, and that groundwater was of $Ca^{2+}+Mg^{2+}+Cl^{-}$ water type which means that groundwater is considered to be permanently hard. The permanent hardness of groundwater was attributed to high concentrations of Mg and Ca ions in groundwater. [8] further pointed out that values obtained from TDS showed that groundwater fell within fresh water category. [16] studied groundwater quality within abandoned Nkalagu limestone quarry, Ebonyi state Nigeria. A total of 13 groundwater sample was evaluated to carefully assess the influence of past mining activities on groundwater suitability for irrigation. From their findings, it was observed that 53.85% of groundwater samples were of (Cl^{-}-SO_4^{2-}) dominant, 15.38% were of (SO_4^{2-}- Cl^{-}-HCO_3^{-}) and (SO_4^{2-}-Cl^{-}) dominant, while 7.69% were of (Mg^{2+}-SO_4^{2-}-Cl^{-}-HCO_3^{-}) and (Cl^{-}-SO_4^{2-}-HCO_3^{-}) dominant type. Ionic contents revealed that Mg^{2+} dominant and SO_4^{2-}-Cl^{-} were the dominant ions in groundwater. [17] used geochemical and Source Rock Deduction (SRD) in evaluating and characterization of groundwater quality around Umuoghara limestone quarry, their findings revealed that groundwater were of $Ca^{2+}>Mg^{2+}>Cl^{-}>SO_4^{2-}>Na^{+}+K^{+}>HCO_3^{-}$ water trend. SRD showed that groundwater were of various origin, and Soltan classification revealed that groundwater were of Na^{+} - SO_4^{2-} water type.

5.2 Related Article on Water Type and Their Facies

The water resources of Ohaozara was studied by [21] their findings revealed that water facies evolution were of different types namely; calcium bicarbonate, sodium chloride and sodium/potassium bicarbonate facies that exist within the northern and southern parts respectively and that the geochemical facies of the area were linked to bedrocks. [21] were of the view that the origin of HCO_3^{-} facies were linked to carbonate rich sandstone, sandstone/siltstones that underlie the northern part of the area, while Nacl facies were linked to brine loaded bedrocks, weathered/fractured shale that lies within Okposi/Uburu area. They further stated that the dominant anions are HCO_3^{-} and Cl^{-} and dominant cation are Ca^{2+} and Na^{+}.

6. Conclusion

Mining activities around active and abandoned mines pose threat to the quality and quantity of water resources around the world. Findings from reviewed papers revealed that mining activities in the past has negatively influence water resources of the study area. It was also observed that most research carried out around the mines within Ebonyi State were based on assessment/studies of effect of mine on soil with emphasis on heavy metals. To the best of our knowledge, published research on impact of mining on water resource is limited. Emphasis is not placed on assessment of mining activities on water resources and also to determine the water facies/hydrogeochemical process around these mines sites across the study area. There is no proper water management plan around active and abandoned mine site across the Ebonyi state, Nigeria, water from these mines are often discharged without any treatment or beneficial use. However, if proper water management is adopted, the water generated during and after mining operations can be harnessed and used for domestic, industrial and irrigation purpose.

References

[1] Nnabo, P. N. Surface Water Contamination by Heavy Metals from Enyigba Pb-Zn Mine District, Southeastern Nigeria Using Metal Enrichment and Pollution Indices. International Journal of Science and Technology, 2016, 5(1): 8-16.

[2] Nwokemodo, E.C. Evaluation of Heavy Metal Contamination of Soil and Water by Abandoned Mine-Pits and Waste Rocks from Lead-Zinc Mining at Enyigba. Published MS.c Dissertation, 2009.

[3] Moses, O.E., Ruth, O.E. Environmental degradation on land in Enyigba with reference to Artisan Lead-Zinc miner in south eastern Nigeria. J Multidiscip Sci Res., 2015, 3(3):32-34

[4] Igwe, O., Adepehin, E. I., Iwuanyanwu, C. Environmental effects of the mining of lead-zinc minerals in Enyigba and its suburbs, southern Benue Trough, Nigeria. Nigeria Journal of Education, Heath and Technology Research, 2012, 3(2): 30-44.

[5] Nnabo, P. N. Environmental impacts of lead/zinc mining in Enyigba area, SE of Abakaliki, SE Nigeria. Unpublished Ph.DThesis, Ebonyi State University, Abakaliki, Nigeria, 2011: 322.

[6] Nnabo, P. N. Assessment of heavy metal distribution in rocks from Enyigba Pb-Zn district, southeastern Nigeria. International Journal of Innovation and Scientific Research, 2015a, 17(1): 175-185

[7] Nnabo, P. N. Heavy Metal Distribution and Contamination in Soils around Enyigba Pb-Zn Mines District, South Eastern Nigeria. Journal of Environment and Earth Science. 2015b, 5(16): 38-49.

[8] Eyankware, M. O.,Obasi, P. N., Omo-Irabor, O. O. Akakuru, O. C. Hydrochemical characterization of

DOI: https://doi.org/10.30564/hsme.v2i2.2412

abandoned quarry and mine water for domestic and irrigation uses in Abakaliki, southeast Nigeria. Modeling Earth Systems and Environment, 2020a. https://doi.org/10.1007/s40808-020-00827-5

[9] Ezeh, H. N, Anike, O. L., Egboka B.C.E. The distribution of some heavy metals in soil around the derelict Enyigba mines and its implications. J.Current World Envir., 2007, 2: 99-106.

[10] Obasi, P.N., Akudinobi, B.B. Potential health risk and levels of heavy metals in water resources of lead-zinc mining communities of Abakaliki, southeast Nigeria. Applied Water Science, 2020, 10: 184. https://doi.org/10.1007/s13201-020-01233-z

[11] Mondal, G.C., Singh,K.A., Singh,B.A., Tewary, B.K., Amalendu, S. Hydrogeochemistry and Quality Assessment of Mine Water of West Bokaro Coalfields, Hazaribag, Jharkhand, India. Journal of Materials Science and Engineering, 2013, 3(8): 540-549

[12] Deniz, S. Y. Characterization and comparison of mine wastes in Can Coal Basin, northwest Turkey: a case study. Environmental Earth Sciences, 2019, 78: 154. https://doi.org/10.1007/s12665-019-8160-0

[13] Obasi, P.N., Eyankware, M.O., Akudinobi, B.B.E., Nweke, M.O. Hydrochemical investigation of water resources around Mkpuma Ekwaoku mining district, Ebonyi State Southeastern Nigeria. Afr J Geo-sci Res., 2015a, 3(3): 01-07.

[14] Ezeh, V. O., M. O. Eyankware, O. O. Irabor, P. N. Nnabo. Hydrochemical Evaluation of Water Resources in Umuoghara and its Environs, Near Abakaliki, South Eastern Nigeria. Intern. Jour. of Sci. and Healthcare Res. India, 2016, 1(2): 23-31.

[15] Eyankware, M. O., Obasi, P.N., Akakuru, O.C. Use of Hydrochemical Approach in Evaluation of Water Quality around the Vicinity of Mkpuma Ekwaoku Mining District, Ebonyi State, SE. Nigeria for Irrigation Purpose. Indian Journal of Science, 2016, 23(88): 881-895.

[16] Eyankware, M.O., Nnajieze, V.S., Aleke, C.G. Geochemical Assessment of Water Quality for Irrigation Purpose, in Abandoned Limestone Quarry pit at Nkalagu area, Southern Benue Trough Nigeria. Environ Earth Science, 2018a, 77: 66. https://doi.org/10.1007/s12665-018-7232-x

[17] Eyankware, M. O., Ogwah, C., Okeke, G.C. Geochemical evaluation of groundwater origin using source rock deduction and hydrochemical facies at Umuoghara Mining Area, Lower Benue Trough, SE Nigeria. Int Res J Earth Sci., 2018b, 6(10): 1-11.

[18] Eyankware, M. O. Hydrogeochemical Evaluation of Groundwater for Irrigation Purposes in Mining Areas of Umuoghara Near, Abakaliki, SE. Nigeria. Science & Technology, 2017, 3(9): 1-19

[19] Aloh, O. G., Obasi, N. A., Chukwu K. E., Agu, A. N. Effects of Lead-Zinc Mining Activities on Water and Soil Quality in Ameka Mining Area of Ezza South, Ebonyi State, Nigeria. International Research Journal of Natural and Applied Sciences, 2016, 3(7): 194-222.

[20] Ekpe I.I, Ibiam J.A, Nwankwo V.C., Asagwara S.C., Oludare C.G., Anyanwu N.J., Okere S. Salinity And Elemental Properties of Irrigation Water Supplies of Ebonyi State Southeast Nigeria. FUTO Journal Series, 2015, 1(2): 119-123.

[21] Obasi, P.N., Akudinobi, B.E.B. Geology, Water Types and Facie Evolution of the Ohaozara Saline Lake Areas of Ebonyi State, Nigeria. International Journal of Scientific and Research Publications, 2015b, 5(9): 1-7.

[22] Obasi, P. N., Obini, N. Ani, C. C., Okolo, C. M. Evaluation of Hydrochemical Attributes of the Amachara Mining Area, Lower Benue Trough, International Journal of Scientific Engineering and Science, 2018, 2(1): 60-65.

[23] Okolo, C.C., T. D. T. Oyedotun, T.D.T., Akamigbo, F. O.R. Open cast mining: threat to water quality in rural community of Enyigba in southeastern Nigeria. Applied Water Science, 2018, 8: 204. https://doi.org/10.1007/s13201-018-0849-9

[24] Igbozuruike, M. U. Vegetation types. In: Oformata GEK (ed) Nigeria in maps, eastern state. Ethiope Publ, Benin, 1975: 30-31.

[25] Reyment, R. A. Aspects of geology of Nigeria. Ibadan University Press, Ibadan, 1965.

[26] Agumanu, A.E. The Abakaliki and Ebonyi formations: subdivisions of the Albian Asu River Group in the southern Benue Trough, Nigeria. J Afr Earth Sci., 1989, 9: 195-207.

[27] Hoque, M. Petrographic differentiation of tectonically controlled Cretaceous sedimentary cycles, southern Nigeria. Sediment Geol., 1977, 17: 235-245.

[28] Chukwu, A., Obiora, S. C. Whole-rock geochemistry of basic and intermediate intrusive rocks in the Ishiagu area: further evidence of anorogenic setting of the Lower Benue rift, southeastern Nigeria. Turk J Earth Sci., 2014, 23: 427-443.

[29] Olade, M. A. The Abakaliki pyroclastics of Southern Benue Trough, Nigeria: their petrology and tectonic significance. J Min Geol., 1979, 16(1): 17-24.

[30] Chukwu, A., Obiora, S. C. Geochemical constraints on the petrogenesis of the pyroclastic rocks in Abakaliki basin (Lower Benue Rift), southeastern Nigeria. J Afr Earth Sci., 2018, 141: 207-220.

 DOI: https://doi.org/10.30564/hsme.v2i2.2412

[31] Murat, R. C. Stratigraphy and Paleogeography of the Cretaceous and lower Tertiary in Southern Nigeria. In Proc. of the Conf. on African Geology held at Ibadan, Nigeria, 1972: 251-266

[32] Obiora SC, Umeji AC. Petrographic evidence for regional burial metamorphism of the sedimentary rocks in the lower Benue Rift. J Afr Earth Sci., 2004, 38: 269-277.

[33] Obiora SC, Charan SN. Geochemistry of regionally metamorphosed sedimentary rocks from the lower Benue Rift: implicationsfor provenance and tectonic setting of the Benue Rift sedimentary suite. S Afr J Geol., 2011, 114: 25-40.

[34] Okogbue, C.O., Aghamelu, O.P. Performance of pyroclastic rocks from Abakaliki Metropolis (southeastern Nigeria) in road construction projects. Bull Eng Geol Environ., 2013, 72: 433-446. https://doi.org/10.1007/s10064-013-0489-0

[35] Aghamelu, O.P., Okogbue, C.O. Some geological considerations and durability analysis on the use of crushed pyroclastics from Abakaliki (Southeastern Nigeria) as concrete aggregate. Geotech Geol Eng, 2013, 31(2): 699-711.

[36] Okogbue, C. O., Nweke, M. The 226Ra, 232Th and 40K contents in the Abakaliki baked shale construction materials and their potential radiological risk to public health, southeastern Nigeria. J Environ Geol, 2018, 2(1): 13-19.

[37] Farrington, J. L. A preliminary description of Nigerian lead - zinc field. Econ Geol., 1952, 47: 485-508.

[38] Akande SO, Muck A Umeji AC. Mineralogical, textural and paragenetic studies of the lead-zinc- copper ore in the lower Benue Trough and their genetic implications. Journal of Mining Geology, 1990, 26(2): 157-163.

[39] Obasi, A.I., Ogwah, C., Selemo, A.O.I., Afiukwa, J.N., Chukwu, C. G. In situ measurement of radionuclide concentrations (238U, 40K, 232Th) in middle Cretaceous rocks in Abakaliki-Ishiagu areas, southeastern Nigeria. Arabian Journal of Geosciences, 2020, 13: 374. https://doi.org/10.1007/s12517-020-05360-4

[40] Eyankware, M. O. Igwe, E.O., Ogwah, C., R. O. E.U. Review: Achievable sustainable use and management of water resources for irrigation in Nigeria. Int Res J Earth Sci, In Press view, 2020b.

[41] Omlin, S., Bauer, G.F., Brink, M. Effects of noise from non-traffic related ambient sources on sleep: review of the literature of 1990 - 2010. Noise Health, 2011, 13: 299-309.

[42] Nordstrom, D.K., Alpers, C.N. Geochemistry of acid mine waters; in Plumlee, G.S., and Logsdon, M.J. (eds.), The Environmental Geochemistry of Mineral Deposits, Part A. Processes, Techniques, and Health Issues: Society of Economic Geologists, Reviews in Economic Geology, 1999, 6A: 133-160.

DOI: https://doi.org/10.30564/hsme.v2i2.2412

BILINGUAL PUBLISHING CO.
Pioneer of Global Academics Since 1984

Hydro Science & Marine Engineering
https://ojs.bilpublishing.com/index.php/hsme

ARTICLE

Stream Monitoring and Preliminary Co-Treatment of Acid Mine Drainage and Municipal Wastewater along Dunkard Creek Area

Dongyang Deng [1*] Lian-shin Lin[2] Andrea Nana Ofori-Boadu[3]

1. Built Environment, Center of Excellence in Product Design and Advanced Manufacturing (CEPDAM), North Carolina Agricultural and Technical State University, Greensboro, NC 27411, USA
2. Civil and Environmental Engineering, West Virginia University, Morgantown, WV 26506-6103, USA
3. Department of Built Environment, North Carolina A&T State University, Greensboro, NC, 27411, USA

ARTICLE INFO

Article history
Received: 10 October 2020
Accepted: 26 October 2020
Published Online: 30 October 2020

Keywords:
Combined treatment
Mixing experiments
Anaerobic batch reactor treatment

ABSTRACT

This study investigated coal-mine drainage (AMD) and municipal wastewater (MWW) contaminant concentrations and conducted the combined treatment in phases I and II: phase I, evaluating the effects of mixing the two based on the extent of acid neutralization and metals removal; phase II: conducting anaerobic batch reactor treatment of AMD and MWW under varying COD/sulfate ratios (0.04-5.0). In phase I, acid mine drainage water quality conditions are as follows: pH 4.5, acidity 467.5 mg/L as $CaCO_3$, alkalinity 96.0 mg/L as $CaCO_3$, Cl^- 11.8 mg/L, SO_4^{2-} 1722 mg/L, TDS 2757.5 mg/L, TSS 9.8 mg/L, BOD 14.7 mg/L, Fe 138.1 mg/L, Mg 110.8 mg/L. Mn 7.5 mg/L, Al 8.1 mg/L, Na 114.2 mg/L, and Ca 233.5 mg/L. Results of the mixing experiments indicated significant removal of selected metals (Fe 85~98%, Mg 0~65%, Mn 63~89%, Al 98~99%, Na 0~30%), acidity (77~95%) from the mine water and pH was raised to above 6.3. The Phase II results suggested under the wide range of COD/sulfate ratios, COD and sulfate removal varied from 37.4%-100% and 0%-93.5% respectively. During biological treatment, alkalinity was generated which leads to pH increase to around 7.6-8.5. The results suggested feasibility of the proposed technology for co-treatment of AMD and MWW. A conceptual design of co-treatment system which is expected to remove a matrix of pollutants has been provided to utilize all the locally available water resources to achieve the optimum treatment efficiency. The technology also offers an opportunity to significantly reduce capital and operating costs compared to the existing treatment methodologies used.

Featured Application: In this study, we have measured the concentrations of contaminants in acid mine drainage (AMD) and municipal wastewater (MWW) and conducted the combined treatment in phases I and II. This is significant because in previous years there was a massive fish kill that is linked to the high total dissolved solids (TDS) and salinity content in the water. With the current proposed combined treatment technology, it shows high potential in reducing TDS and salinity content in the combined wastewater which will prevent similar accident (Dunkard creek fish kill in 2019) happening again.

**Corresponding Author:*
Dongyang Deng,
Built Environment, Center of Excellence in Product Design and Advanced Manufacturing (CEPDAM), North Carolina Agricultural and Technical State University, Greensboro, NC 27411, USA;
Email: ddeng@ncat.edu

 DOI: https://doi.org/10.30564/hsme.v2i2.2448

1. Introduction

Acid mine drainage (AMD) originates from oxidation of mine rocks exposed to air and water during mineral extraction which leads to the generation of sulfate, dissolved metals (mainly iron) and low pH [1,2]. It degrades water quality in rivers near mining regions. It is estimated that over 3,000 miles of streams are impaired in the Appalachia due to acid mine drainage [3]. As such, the remediation of these bodies is of primary environmental importance in watersheds with historical mining practices. The key focus on treating AMD is pH neutralization, metals precipitation, and sulfate reduction. In order to remediate AMD, a variety of treatment and prevention methods have been utilized throughout different stages of AMD formation process [4]. Generally, these treatments can be grouped into passive or active systems. Passive treatment generally includes biological activities in systems such as bioreactors, lagoons and wetlands [5]. Based on the sulfate concentration in AMD, one of the widely utilized passive treatment methods is sulfidogenic process (utilizing sulfate-reducing bacteria (SRB)) to reduce sulfate to sulfide, and to promote alkalinity production and metal sulfides formation [6,7]. For biotic sulfate reduction, it generally requires electron donors from organic sources [8-13]. A previous study from applied various organic sources (e.g., wood chips, sawdust, leaf mulch and sheep manure) for sulfate reduction and suggested higher sulfate reduction rates with addition of sewage sludge compared to no sludge addition [7]. Additional studies also showed that diversified sources of electron donors from municipal wastewater (MWW) were more preferable for sulfate reducing bacteria growth [12,14]. Active systems are often required for higher flow rates or more complex treatment requirements. This approach offers enhanced treatment flexibility to adapt to fluctuations in contaminant concentration, flow rate, and other environmental conditions. After treatment, any number of separation methods can be employed, with common applications including sedimentation, filtration through granular media, and membrane filtration [15]. Although active chemical treatment can effectively treat AMD, it is generally associated with high operational costs and massive amounts of sludge being produced [16].

Municipal wastewater (MWW) generally features high pH, TSS, alkalinity, COD and the typical range is: pH of 7-8, alkalinity from 200-250 mg/L as $CaCO_3$ [17,18]. Generally, MWW treatment needs to reduce the suspended solids, phosphorus, nitrogen and biochemical oxygen demand concentrations to certain limits in order to maintain receiving water bodies from water quality degradation and negative human health impact. Traditional MWW treatment consumes significant amount of economic, material and energy resources. Sludge scraping, mechanical aeration, sludge and effluent pumping, ultraviolet disinfection, clarifier skimming, and other conventional MWW treatment methods consume substantial amount of energy [18-20]. Among the various treatment processes, aeration of activated sludge is the most energy consuming process, typically accounting for 45% of total energy consumption [21], and energy usage is around 0.28-0.71 kWh/m^3 [22].

In MWW, suspended solids are generally removed by either filtration, flocculation, biodegradation, or settling [18]. Phosphorus are often removed by ferric iron or aluminum salt dosing [23]. However, these chemical dosing can be considerably expensive and consumption of these flocculants has increased over recent years [24,25]. This indicated that AMD which contain high amount of ferric iron salts can be utilized for phosphorus adsorption [26]. In anaerobic treatment of AMD which contains sulfate reducing bacteria, nutrients (nitrogen, phosphorus) can be supplied from MWW for cost-effective operation [5,27]. Organics (Biochemical oxygen demand) in MWW can also be lowered by bacterial respiration through sulfidogenic reaction. So MWW and AMD serve as perfect combination to remediate the overall water quality.

Co-treating AMD and MWW could be cost-effective and mitigate infrastructure challenges of building two separate treatment systems in places where these two wastewaters are existing but financial resources are limited. The study of co-treatment of AMD and municipal wastewater (MWW) has long been explored. A paper first discussed mixing of AMD and MWW has great potentials in reducing pathogens by low pHs and high metal concentrations in AMD, but has not studied the combined treatment potentials [28]. Another paper discovered that Escherichia coli population was significantly decreased when adding AMD to MWW which indicated combined treatment has promoted disinfection effect [29]. Another study investigated varying pH impact on sewage related microbes and found a rapid decreasing trend in bacteria concentration with lowering pH values [30].

The AMD can be added directly to the activated sludge tank, either as a raw stream or after a pre-treatment such as mixing with digested sludge or screened MWW. The effect is a mutual benefit to both wastes while maintaining the integrity of the parent wastewater treatment facility. A combination of dilution by and alkalinity of the MWW and anaerobic digester sludge neutralized the acidic discharge, which in turn causes metal ions to precipitate from the solution. The AMD, meanwhile, aids in removing MWW constituents such as phosphorus, which adsorb and

DOI: https://doi.org/10.30564/hsme.v2i2.2448

co-precipitate with the metal (oxy) hydroxides in a loose sludge as with the previous processes.

The AMD and MWW sampling sites (supplementary Figure S1) are located around a Dunkard river network affected by AMD associated with the intensive mining of metal sulfides. Releases of AMD have low pH, high concentrations of iron, calcium, aluminum, sodium and manganese, high sulfate and chloride, high specific conductivity, high total dissolved solids, and low concentrations of toxic heavy metals. Currently the lower Dunkard Creek water quality is found to be affected by three sources: AMD discharges from abandoned mines: high metal loadings; wastewater from approximately 1,000 residents which is treated to various degrees; alkaline mine drainage discharge via Steele Shaft treatment plant: high TDS. This study is to evaluate an innovative process for addressing all of these problems in a single, comprehensive treatment system. The research objective is to be achieved by conducting the following using a phased approach: Phase I: evaluate pollutant concentrations and trends, and preliminary treatment of combined AMD, municipal wastewater and steel shaft discharge; phase II: conduct the treatment process utilizing anaerobic batch reactor analysis and study microbial sulfate reduction reaction kinetics to develop a conceptual design of the combined treatment process.

2. Materials and Methods

2.1 Site Description

The location of sampling points has been provided in supplementary Figure S1 and Table 1 shows values for pH, acidity, alkalinity, chloride, sulfate, TDS, TSS, BOD, and metals content (iron, Magnesium, Manganese, aluminum, sodium, calcium) in the sampled sites. Site 2A drainage comes from abandoned mines. Site 2B is very close to 2A, and the distance of the two is no more than 10 meters. The water is also from abandoned mines and has similar characteristics for parameters with 2A. Site 7A sample had a nearly neutral pH. However, it has higher acidity than 2A and 2B which can be explained by the Fe content (228 mg/L) compared to 2A and 2B (33 mg/L, 28 mg/L). Site 7B is further upstream and not far from 7A. It had significantly different characteristics from 7A. Site 8A has high acidity which is attributed to its Fe concentration. Site 8B is close to 8A. These two had similar chemical characteristics. Water coming out from Steele Shaft facility has been treated with alkaline materials to raise the pH of acid mine drainage. The discharges were high in sulfate, and sodium concentration. The primary influent, MWW(P), was collected at a location after the bar screen and the secondary influent, MWW(S), was at a location after the clarifier.

2.2 Field Sampling

Phase I: water samples were collected from ten (10) sites including mine drainages (2A, 2B, 7A, 7B, 8A, 8B), Steel Shaft discharges (two separate pipes for replicates analysis – SSD-A, SSD-B), and primary and secondary influents from the Bobtown wastewater treatment facility (MWW(P), MWW(S)). Steel shaft discharges refer to a mine drainage treatment plant by adding alkaline chemi-

Table 1. Acid mine drainage, municipal wastewater and steel shaft discharge characteristics summary in the Dunkard Creek Sampling Sites

Parameters	Unit	2A	2B	7A	7B	8A	8B	SSD-A	SSD-B	MWW(P)	MWW(S)
pH		2.7	2.7	5.9	6.9	5	4	7.8	8	7.3	7
Acidity	mg/L as $CaCO_3$	351	284	616	48	736	770	8.6	3.2	47.5	20.2
Alkalinity	mg/L as $CaCO_3$	0	0	156	360	48	11.7	153	187	237.2	84.5
Cl^-	mg/L	9.1	8.6	13.3	9.8	16.6	13.6	71	79	101.3	98
SO_4^{2-}	mg/L	1603	1335	1991	512	2463	2428	7057	5680	92.5	82.4
TDS	mg/L	2478	2032	3200	1144	3863	3828	10395	8390	340	290
TSS	mg/L	4.6	11.3	12.4	9.6	13.3	7.8	6.4	19.3	86.6	11.6
BOD	mg/L	6.7	7.9	25.7	10.9	12.2	24.6	7.8	8.9	>136.2	>26.1
Fe	mg/L	33	28	228	1.5	274	264	0.2	1.3	0.4	0.2
Mg	mg/L	121	111	117	50	131	135	217	156.5	7.3	7.5
Mn	mg/L	3.8	3.8	10	1.3	13	13	0.4	0.1	0	0
Al	mg/L	24	23.5	0.2	0.1	0.3	0.5	0.1	0.1	0.2	0
Na	mg/L	33	35	165	148	152	152	2508	3765	65.9	67.4
Ca	mg/L	238	226	257	131	270	279	565	355	163	159

 DOI: https://doi.org/10.30564/hsme.v2i2.2448

cals (limestone, sodium hydroxide, etc.) to neutralize the water turn it into alkaline mine drainage. Field measurements of pH, temperature, turbidity and electrical conductivity were taken. SSD, AMD and MWW samples were collected and transported under refrigeration to laboratories and were stored at 4˚C before analysis. Sample holding time for acidity, alkalinity, TSS, TDS, and nutrients was less than 24 hrs. Concentrations of Cl^-, SO_4^{2-}, COD, and metals were analyzed within 1 week of the sampling. AMD samples collected from the above-mentioned six (6) locations were mixed together in equal volumes to make a combined AMD solution for experiments with MWW sample and SSD sample.

In phase I (1) the AMD samples were mixed with MWW at different ratios to investigate the feasibility of co-treatment of the two waste streams. In phase I (2), mixing experiments were conducted using AMD, alkaline SSD, and MWW to evaluate the effects of combined mixing on removing metals, acidity, and other constituents in the mine drainage samples, since it is more closely simulate what actually will happen in real environment based on the location of the three streams.

Phase II: water samples were collected from AMD site 8A along Dunkard Creek, Pennsylvania, and wastewater samples (MWW (P)) from the Bobtown, Pennsylvania and Star City, West Virginia wastewater treatment plant. Field measurements of pH, temperature, turbidity and electrical conductivity were taken. SSD, AMD and MWW samples were collected and transported under refrigeration to laboratories and were stored at 4˚C before analysis. Sample holding time for acidity, alkalinity, TSS, TDS, and nutrients was less than 24 hrs. Concentrations of SO_4^{2-} and COD were analyzed within 1 week of the sampling.

2.3 Experimental Procedure

2.3.1 The Phase I Mainly Involves the Mixing of AMD, MWW, SSD to Promote Chemical Precipitation

(1) Mixing experiment 1

The first set of mixing experiments was performed using mixture of all the mine drainages from the six locations collected (1:1:1:1:1:1 volume ratios) and mixture of the primary and secondary influents (1:1 volume ratio). Two different mixing ratios between the mine drainage mixture and wastewater mixture were used: 200mL (AMD mixture) + 400 mL (sewage MWW mixture) (abbreviation:200A+400S), 300 mL (AMD mixture) + 300mL (sewage MWW mixture) (abbreviation:300A+300S). The results are summarized in Figure 1.

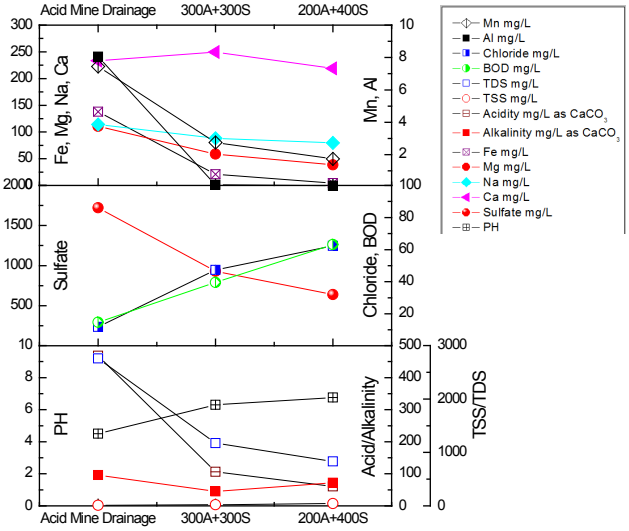

Figure 1. Results of mixing experiments 1

(2) Mixing experiment 2

The second set of mixing experiments was conducted using mixture of all the AMD collected (1:1:1:1:1:1 volume ratios), mixture of the primary and secondary influents (1:1 volume ratio), and the alkaline SSD. Two different ratios for the mixing of the mine drainage mixture, wastewater mixture and steel shaft mine drainage were used (the ratio is determined based on the in-situ flowrate of AMD and alkaline SSD: 200mL (AMD mixture) + 400 mL (MWW mixture) + 400 mL (alkaline SSD) (abbreviation:1+2+2), 100mL (AMD mixture) + 400 mL (MWW mixture)+ 400 mL (alkaline SSD) (abbreviation:1+4+4). The results are summarized in Figure 2.

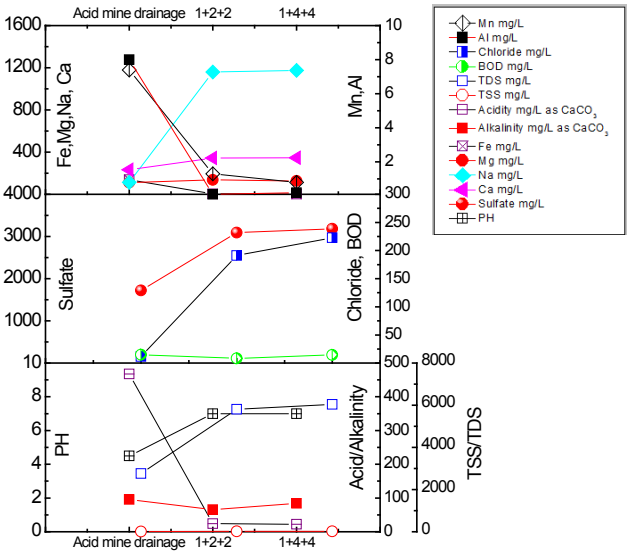

Figure 2. Results of mixing experiments 2

DOI: https://doi.org/10.30564/hsme.v2i2.2448

2.3.2 The Phase II Experiments Focus on Anaerobic Batch Reactor Treatment

The collected samples were mixed using different ratios and the mixture solutions (after settlement of particulate matters) were treated in anaerobic bioreactors for COD and sulfate removal in anaerobic conditions.

(1) Pre-setup mixing: a range of AMD: MWW mixing ratio was used to evaluate the chemical composition of the mixture solution.

(2) Reactor Series 1: Four different MWW: AMD mixing ratios (volume based): 1:1, 2.5:1, 2.5:1(with 20 g AMD soil addition to provide bacterial source for anaerobic degradation purposes, AMD soil refer to the soil sampled from AMD impacted sites), 5:1 were used. This resulted in a range of COD: sulfate ratios (0.2, 0.6, 0.8, and 5) and the mixture solutions were treated in four bioreactors respectively.

(3) Reactor Series 2: Another series of four bioreactors were set up to treat mixture solutions with lower COD: sulfate ratios (0.06, 0.04, 0.05, and 0.13) than those in Reactor Series 1. Probably because of the heavy rain season, organics content in municipal wastewater (Bobtown, PA) has been relatively low.

(4) Reactor Series 3: In order to achieve COD to sulfate ratios similar to Series 1, Star City Wastewater Treatment Plant was sampled instead of Bobtown Water Treatment Plant to obtain higher content of COD and acid mine drainage was sampled from the same place around Dunkard creek area. COD/sulfate ratios of 1.6, 2, 2.4, and 3.1 (This is COD to Sulfate ratio in terms of concentration) were obtained.

2.4 Chemical Analysis Procedures

All samples were analyzed after filtration with 0.45 μm filter paper. pH, TSS, TDS, and BOD were measured according to Standard Methods [31]. pH and conductivity were tested using pH/conductivity meter (YSI 63). COD and sulfate concentrations were analyzed using a UV-Vis spectrophotometer (Hach DR2800). Alkalinity and acidity were analyzed using autotitrators (Thermo Scientific Orion 950 and MettlerToledo DL50). Samples for metals analysis were digested by concentrated nitric acid (~70%, trace metal grade), and measured using an atomic adsorption spectroscopy (Perkin Elmer 3100). Duplicate sample has been analyzed to ensure accuracy of experiments.

3. Results and Discussion

3.1. Phase I Study

Mixing Experiments

From Figure 1 and 2, the two series of mixing experiments in phase I exhibit similar results in almost all the parameters, each AMD + MWW and AMD + MWW + SSD treatment produced substantial alkalinity and raised pH to around 6-7, which is neutral, so it does indicate an ideal environmental for microbial growth. Besides the added alkalinity and dilution of acidity that resulted from mixing MWW and AMD, significantly increased pH was observed. These results indicate that the full advantages of mixing AMD with MWW has been realized and further acidity can be buffered during anaerobic incubation phase. It is unknown if the primary mechanism for acid neutralization is abiotic (i.e., sorption to organic ligands) or biotic (i.e., biological sulfate reduction) because no control study has been performed in phase I. Additionally, based on the paper [5] substantial biological sulfate reduction is unlikely to happen due to the relatively short period of mixing time (24 hours) and the present metal concentrations (Fe) are much greater than those reported to be severely inhibitive to sulfate reducing bacteria [32]. Therefore, it is assumed that the majority of the acid neutralization and alkalinity generation observed when mixing AMD + MWW and AMD+MWW+SSD were via abiotic process. In the mixing experiment 2, the acid neutralization capacity provided by SSD (mainly composed of limestone chemicals) was sufficient to produce net-alkaline effluent. And this is highly promising for treatment purposes because it serves as alkaline addition to co-treat AMD and MWW, which could result in significant cost savings. In addition, further alkalinity may be generated by sulfate reducing bacteria in phase II using the substantial amount of biodegradable organic material in MWW.

As expected, dissolved concentrations of major metal elements (in the mg/L range) of interest in the mixed AMD decreased with MWW exposure (Figure 1). The AMD + MWW mixtures resulted in decreased dissolved Al, Fe, Mn, Mg and Na. The AMD + MWW + SSD exposures resulted in less removal of some metals (Mg, Na and Ca) due to the high concentration of these metals in SSD (Table 1). Overall, results indicate that passive mixing and incubation of AMD with WW can remove significant quantities of heavy metals (Mn, Al and Fe) from solution. The removal mechanisms are likely due to the increase in pH which promoted the formation of the insoluble $Al(OH)_3$. Besides, Al and Fe can combine with phosphate to form a stable solid, and they can also complex with organic materials to form ligands [23]. Additional studies are needed to evaluate more variation of ratio of AMD to MWW and mixing duration to optimize Al and Fe removal.

In general, Mixing experiment 1 and 2 both resulted in significant decreases in acidity, iron, manganese, alumi-

 DOI: https://doi.org/10.30564/hsme.v2i2.2448

num, and the rest of the parameters relatively remaining on the similar level with the mine mixture (mixing experiment 1) or those even higher than the mine mixture (mixing experiment 2), this is probably because of the municipal wastewater and Steel Shaft water (as the Table 1 showing) exhibits fairly much higher concentration on those parameters, like sodium, calcium, chloride, sulfate and TDS, so this has influenced the mixing results in sulfate, chloride, sodium, calcium. However, the elevated metals and sulfate concentration can be removed in later stage, the anaerobic treatment process. And above all, the preliminary goal of the mixing is to decrease acidity and Fe which has been achieved, and the pH is raised to around 7. It is perfect for microorganisms, which suggests a promising future for microbial growth and further removal of metals and sulfate.

3.2. Phase II Study

Phase II study followed the concept of preliminary study of combined treatment in phase I and investigate further into biological treatment processes. In this phase, combined treatment has been conducted through two-step: mixing and biological treatment.

3.2.1 Pre-setup Mixing

Mixing ratios of 1:5, 1:10, and 1:15 (AMD: MWW, volume based) were performed to determine proper mixing ratio for subsequent anaerobic biological treatment. The mixing water characteristics are provided in Table 2. In order to provide sufficient organics for anaerobic biological degradation process, AMD: MWW mixing ratios were chosen based on COD/sulfate concentrations. So AMD: MWW mixing ratios of 1:1, 1:2.5, 1:2.5S (20g AMD soil added) and 1:5 have been chosen.

Table 2. Chemical Composition of the mixture solutions from the Pre-Setup Mixing

Parameters	Unit	1:5	1:10	1:15
pH		6.5	6.7	6.7
Acidity	mg/L as $CaCO_3$	98.4	88.3	93.8
Alkalinity	mg/L as $CaCO_3$	208.9	232.7	248.2
Cl^-	mg/L	95.9	95.9	101.4
SO_4^{2-}	mg/L	516.3	369.6	333.5
TDS	mg/L	510	694	1701
TSS	mg/L	307	340	351
BOD	mg/L	200.3	226.2	290.1
Fe	mg/L	31.5	14.1	12.6
Mg	mg/L	23.6	17.1	14.1
Mn	mg/L	1.4	0.8	0.5
Al	mg/L	0.7	0.4	0.3
Na	mg/L	123	113	107.5
Ca	mg/L	85.5	72	66.5
Cu	mg/L	0	0	0
NO_2^-	µg/L	1.7	10.5	10.6
NH_3	mg/L	37.1	34.8	37.5
NO_3^-	mg/L	0.2	0.4	0
PO_4^{3-}	mg/L	0.1	0.3	0.8

3.2.2 Anaerobic Bioreactor Treatment

(1) Reactor Series 1

A series of four bioreactors (Series 1) were set up using Boston Round bottles. The bioreactors were used to treat mixture solutions of different AMD: MWW volume ratios – 1:1, 1:2.5, 1:2.5 and 1:5 with 20 g of AMD soil. The volume mixing ratios resulted in initial COD: sulfate ratios of 0.2, 0.8, 0.6, and 5, respectively. Each reactor contained solid surfaces for biofilm development (i.e., attached growth of microorganisms). The results show that all mixing ratios produced satisfactory sulfate and COD removal in the reactors (COD reduction of 67.1%-88.9% and sulfate reduction of 60.8%-93.6%) (Figure 3). COD was dramatically and significantly decreased in the bioreactors containing AMD+MWW mixtures (67.1%-88.9%). The activity of various heterotrophic microbes (i.e., sulfate reducing bacteria, nitrate reduction, fermenters, methanogenesis and iron reducing bacteria) likely served to decrease organics throughout the system and has reported in previous studies [33,34]. PCR and qPCR results indicated that sulfate-reducing bacteria were dominant in the microbial communities and the resulting dsr A gene concentrations ranged from 13.3-15.0 log gene copies/µL) which are significantly higher than the levels in the original of AMD (9.7 log gene copies/µL) and MWW (12.5 log gene copies/µL) [34]. Therefore, the authors concluded that the dsrA genes were enriched as a result of the biological treatment. It has been reported that there are 2 to 3.5 copies of dsrA gene per SRB cell [35], and the number of active sulfate reducing bacteria microorganisms can be reasonably estimated from the gene concentrations.

DOI: https://doi.org/10.30564/hsme.v2i2.2448

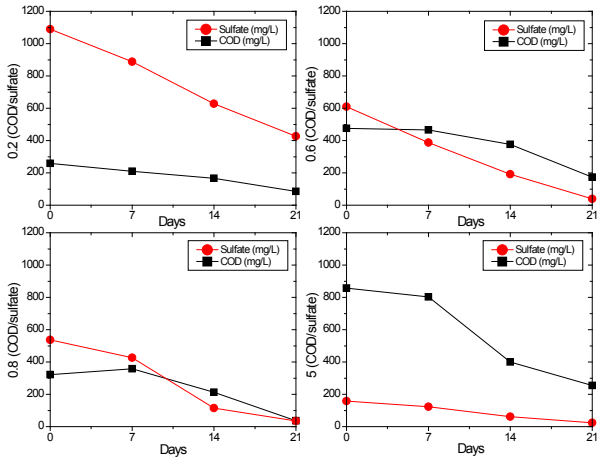

Figure 3. COD and sulfate concentrations in the reactor containing 0.2, 0.6, 0.8 and 5.0 (COD: sulfate) mixture solution ratio

(2) Reactor Series 2

Reactor series 2 refer to the second sampling trip taken to collect AMD and MWW water samples to test the treatability of the mixtures with the same volume mixing ratios of AMD and MWW but result in lower COD: sulfate concentration ratios (0.06, 0.04, 0.05 and 0.13). This could possibly be attributed to the rain season. The bioreactors (Figure 4) produced satisfactory reductions of both COD and sulfate as well (COD reduced 91.9%-100% and sulfate reduced 20.1%-73.2%). This indicates once the microbial community has been established, it can treat much lower COD/sulfate ratios and still achieve satisfying results. The limiting factor in the reactor series 2 is COD concentration since in all COD/sulfate ratios organics has been degraded to below detection level. And when the organics were below detection level, there would be no electron donors for sulfate reducing bacteria to continuously obtain electrons to reduce sulfate.

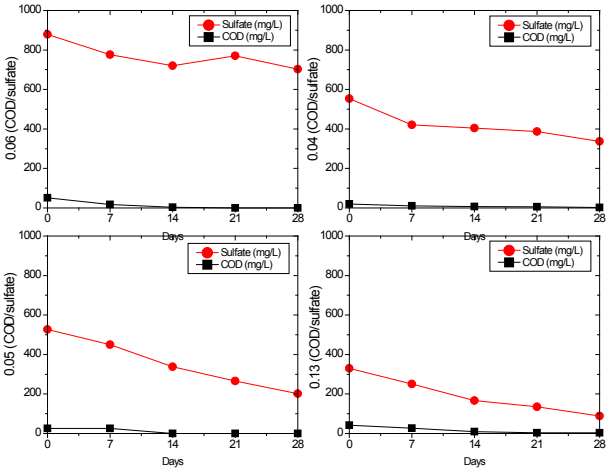

Figure 4. COD and sulfate concentrations in the reactor containing 0.06, 0.04, 0.05 and 0.13 (COD: sulfate) mixture solution ratio

(3) Reactor Series 3

In Reactor series 3, MWW was sampled from the Star City wastewater treatment plant in order to provide sufficient organics for biological sulfate reduction process which resulted in COD/sulfate concentration ratios of 1.6, 2, 2.4 and 3. COD reductions were observed in all four reactors. However, the bioreactors produced mixed results for sulfate reduction (Figure 5). There was a general trend of COD reduction in the bioreactors and for reactors containing COD/sulfate of 1.6, 2 and 3.1 the sulfate is also decreasing substantially. Possible reasons for the inconsistent sulfate concentration trends in reactor COD/sulfate of 2.4 include: a. Different source of wastewater: different composition of wastewater collected from Star City wastewater treatment plant may have caused different microbial responses due to carbon source, pH, and other potentially toxic chemicals. b. Increasing pH over the course of the treatment: pH 5-8 is favorable for microbial growth, and a pH above 8.0 is damaging to microbial community. Fromthe 2nd week, pHs in the bioreactors were higher than 8 which indicated unfavorable environment for the microbial community and resulted in unstable performance (Supplementary materials Figure S2).

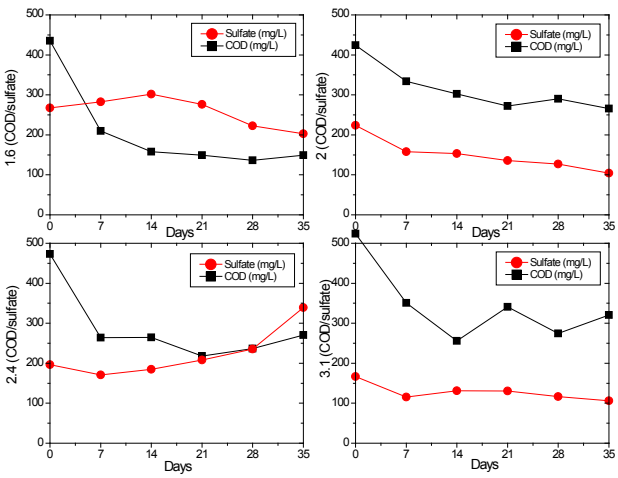

Figure 5. COD and sulfate concentrations in the reactor containing 1.6, 2, 2.4 and 3.1 (COD: sulfate) mixture solution ratio

Overall, the three series of reactors were conducted under a wide range of COD/sulfate ratios from 0.04-5.00. Almost all of the ratios (except COD/sulfate of 2.4) achieved promising results for COD/sulfate reduction, which indicate sulfate reduction related bacterial community has been established. The two step combined treatment process lead to pH increase, COD/sulfate reduction, metals reduced (Fe, Ca, Mg, Mn), and TDS/TSS removal (from Phase I and Phase II).

The full-scale AMD and MWW co-treatment systems

 DOI: https://doi.org/10.30564/hsme.v2i2.2448

may result in energy, chemicals, and cost savings. Aside from low energy and low-cost set-up, these systems could be operated using gravity flow without ongoing purchased energy inputs. A field-scale co-treatment system could be applied in commonly engineered structures, such as ponds, aerobic wetlands, clarifiers, and vertical flow bioreactors, which could decrease engineering costs. Significant cost savings would result from eliminating the need to purchase and transport organic substrate, often a major cost of passive AMD treatment. Cost savings would also result by using AMD as a coagulant/flocculant and disinfectant for MWW treatment. In addition, the use of MWW as no-cost organic substrates consumes an item considered as "waste" to relatively-costly organic substrate, such as the compost or refined carbon sources (e.g., ethanol, methanol) often used in AMD treatment [36]. Raw MWW and high-strength AMD are often not independently addressed with passive methods because of the limitations of conventional passive treatment technologies and/or the lack of locally available suitable carbon substrate [37].

3.3 Conceptual Design and Recommendations

The bioreactors used in this study simply demonstrated feasibility of such treatment sequence (i.e., mixing followed by anaerobic biological treatment). So a conceptual design of the proposed treatment method is recommended for combined treatment of the mine drainages and sewage from the Bobtown, PA (Supplementary materials Figure S4 and Figure S5).

Conceptually, collection lines upstream of the proposed treatment pond (Steel Shaft lines and AMD discharge) could be run combined based on the mixing results given. In addition, a pumped line would convey MWW to the treatment system. The treatment pond could be configured to optimize residence time and reactivity under a collection system that combines Steele Shaft discharge and AML (Acid Mine Leachaye) discharges to form chemical precipitates and settle solids. Then the effluent is then mixed with MWW flow which provides organic matters for biological activities. A large pond would provide much of the biological reactions and settle remaining solids. Effluent could be discharged to Dunkard Creek at the downstream end of the treatment or piped to the Monongahela River.

Use the data obtained from reactor 1:1 of AMD/ SWW volume ratio, series 1 (supplementary material Table S1), the influent concentration of sulfate from the mixture water is 1090.2 mg/L, and the effluent is 158.3 mg/L. This ratio has been picked since locally AMD and SWW were pumped at similar flow rate.

The detention time,

$$\theta = -\frac{\ln\left(\frac{Ceff}{Cinf}\right)}{\kappa}, \quad (1)\ [18]$$

Where

C_{inf} = pollutant concentration in influent (mg/L)

C_{eff} = pollutant concentration in effluent (mg/L)

k = apparent pollutant removal rate (day^{-1})

Since this equation is fit for first-order k, we calculate k value as follows (supplementary material Table S1 and S2, Figure S1): k=0.0247 day^{-1}

So $\theta = -\frac{\ln\left(\frac{427\ mg/l}{1090.2\ mg/L}\right)}{0.0247/d} = 37.9d$, assume void ratio □=0.7, flow rate Q=4.0 cfs = 9 786.3 m^3/d (medium value of flow rate from AML),

$$V = \frac{\theta Q}{\eta} = \frac{37.9d \times 9786.3m3/d}{0.7} = 5.31 \times 105m3, \quad (2)\ [18]$$

So the volume of the treatment pond is 5.31×10^5 m^3, or 1.87×10^7 ft^3.

4. Conclusions

In conclusion, the first set of mixing was effective for removing Fe, magnesium, manganese, aluminum, acidity, sulfate, and increasing pH to around 6. The second has significant removal rate on acidity, Fe and pH is reaching neutral. And at the same time, since the second set is a mixture of the three different sources of water, it more closely depicts what will really happen in the natural environment. But above all, the two set of mixing both reduced significant amount of acidity, Fe, aluminum, manganese, which is the main goal for our mixing experiments, and the pH is favorable for microbial growth which lays a good foundation for the later stage of the project, cultivating sulfate-reducing bacteria

This purpose of this study was to obtain better understanding of water quality along mining affected Dunkard Creek area and propose an optimum treatment method to improve water quality. Along the Dunkard Creek streamline, steel shaft alkaline drainage, AMD and municipal wastewater in Bobtown can be combined to treat the water more efficiently. Through aerobic mixing, metals, TSS and TDS can be reduced and mixture pH has been raised, and the following anaerobic biological treatment promote further organics and sulfate reduction, which would co-precipitate more metals when sulfide is generated and precipitated as metal sulfides.

The conceptual design of co-treatment system has been

DOI: https://doi.org/10.30564/hsme.v2i2.2448

proposed to achieve the purpose of the study. More details need to be considered since the water quality from AMD and municipal wastewater depend by the season and other variables, and more practical concerns need to be taken into account. For better understanding of the whole treatment performance, microbiological community analysis, fate of sulfate and metals needs to be further analyzed.

Supplementary Materials

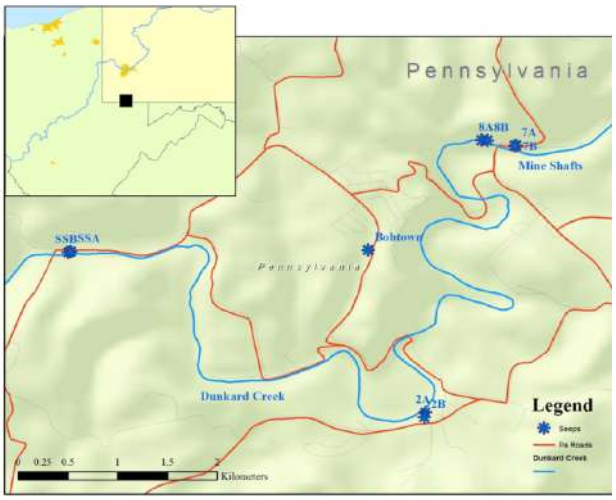

Figure S1. Sampling site locations of Acid Mine Drainage, Municipal Wastewater and Steel shaft discharge

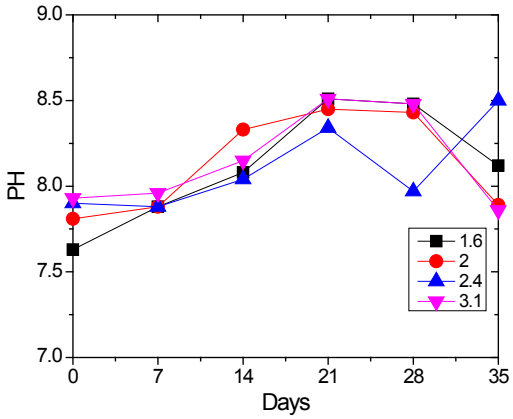

Figure S2. pH changes in the Reactor Series 3

Table S1. COD and Sulfate concentrations in 1:1 Reactors of Series 1

Time	Reactors	COD (mg/L)	Sulfate(mg/L)
1/24/2011	1:1	258.4	1090.2
2/4/2011	1:1	210.1	887.7
2/11/2011	1:1	166.6	627.8
2/18/2011	1:1	84.9	427

Table S2. $\ln C/C_0$ vs. Time in 1:1 Reactor of Series 1

$\ln(C/C_0)$	T(day)
1.00	0
0.81	11
0.58	18
0.39	25

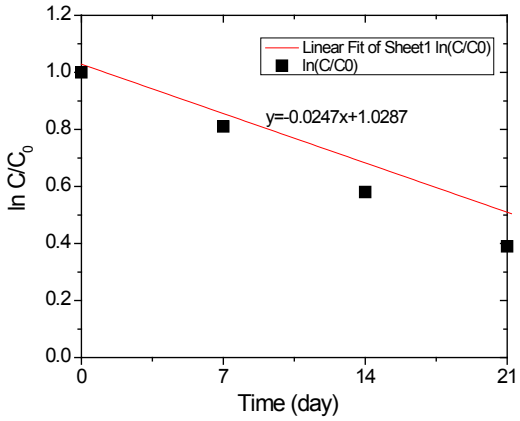

Figure S3. The linear relationship of $\ln C/C_0$ vs. time

Figure S4. Combined mine water and wastewater flow to treatment system

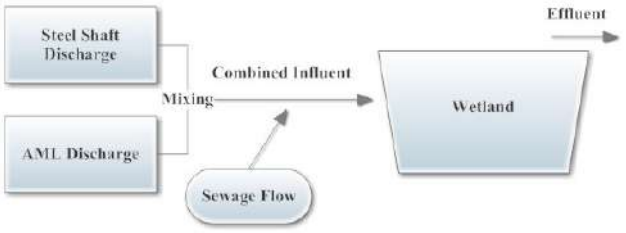

Figure S5. Conceptual Design of Treatment Process

Author Contributions

Conceptualization, D.D.Y., A.N.O-B. and L.-S.L..; methodology, D.D.Y. and L.-S.L..; validation, D.D.Y.. and L.-S.L..; formal analysis, D.D.Y.; investigation, D.D.Y. and L.-S.L..; resources, L.-S.L; writing—original draft preparation, D.D.Y. and L.-S.L.; writing—review and editing, D.D.Y., A.N.O-B. and L.-S.L..

DOI: https://doi.org/10.30564/hsme.v2i2.2448

Conflicts of Interest

The authors declare no conflict of interest.

References

[1] Blowes, D., Ptacek, C., Jambor, J., Weisener, C.,Paktunc, D., Gould, W., Johnson, D. J. E. g. The geochemistry of acid mine drainage. 2003, 9: 149-204.

[2] Johnson, D. B., Hallberg, K. B. J. S. o. t. t. e. Acid mine drainage remediation options: a review, 2005, 338:3-14.

[3] Mining, O. o. S. Office of Surface Mining Annual Report: 2006. . Report No. Report No.: Washington, D.C., USA: U.S. Department of Interior, 2006.

[4] Sengupta, M. Environmental impacts of mining monitoring, restoration, and control. CRC Press, 1993.

[5] Neculita, C. M., Zagury, G. J., Bussière, B. J. J. o. E. Q. Passive treatment of acid mine drainage in bioreactors using sulfate-reducing bacteria: Critical review and research needs. 2007, 36: 1-16.

[6] Lewis, A. E. J. H. Review of metal sulphide precipitation, 2010, 104: 222-234.

[7] Waybrant, K., Blowes, D., Ptacek, C. J. E. S. Technology. Selection of reactive mixtures for use in permeable reactive walls for treatment of mine drainage. 1998, 32: 1972-1979.

[8] Benner, S., Blowes, D., Ptacek, C., Mayer, K. J. A. G. Rates of sulfate reduction and metal sulfide precipitation in a permeable reactive barrier, 2002, 17: 301-320.

[9] Dvorak, D. H., Hedin, R. S., Edenborn, H. M., McIntire, P. E. J. B., bioengineering. Treatment of metal-contaminated water using bacterial sulfate reduction: Results from pilot-scale reactors, 1992, 40: 609-616.

[10] Johnson, K. L., Younger, P. L. J. E. G. The co-treatment of sewage and mine waters in aerobic wetlands, 2006, 85: 53-61.

[11] Jong, T., Parry, D. L. J. W. r. Removal of sulfate and heavy metals by sulfate reducing bacteria in short-term bench scale upflow anaerobic packed bed reactor runs. 2003, 37: 3379-3389.

[12] Strosnider, W., Winfrey, B., Nairn, R. J. M. W., Environment, t. Alkalinity generation in a novel multi-stage high-strength acid mine drainage and municipal wastewater passive co-treatment system. 2011, 30: 47-53.

[13] Tuttle, J. H., Dugan, P. R., Randles, C. I. J. A. M. Microbial sulfate reduction and its potential utility as an acid mine water pollution abatement procedure. 1969, 17: 297-302.

[14] Strosnider, W., Winfrey, B., Nairn, R. J. w. r. Biochemical oxygen demand and nutrient processing in a novel multi-stage raw municipal wastewater and acid mine drainage passive co-treatment system. 2011, 45: 1079-1086.

[15] Skousen, J., Rose, A., Geidel, G., Foreman, J., Evans, R., Hellier, W. Handbook of technologies for avoidance and remediation of acid mine drainage. National Mine Land Reclamation Center, Morgantown, 1998, 131.

[16] Chang, I. S., Shin, P. K., Kim, B. H. J. W. r. Biological treatment of acid mine drainage under sulphate-reducing conditions with solid waste materials as substrate. 2000, 34: 1269-1277.

[17] Henze, M., van Loosdrecht, M. C., Ekama, G. A., Brdjanovic, D. Biological wastewater treatment. IWA publishing, 2008.

[18] Metcalf, L., Eddy, H. Wastewater engineering–treatment and reuse, 4th edn. Handbook. McGraw-Hill, New York, 2003.

[19] Mannino, I., Franco, D., Piccioni, E., Favero, L., Mattiuzzo, E., Zanetto, G. J. E. M. A cost-effectiveness analysis of seminatural wetlands and activated sludge wastewater-treatment systems, 2008, 41: 118-129.

[20] Muga, H. E., Mihelcic, J. R. J. J. o. e. m. Sustainability of wastewater treatment technologies, 2008, 88: 437-447.

[21] Martin M., A. G. Energy audits of WWTPs. Report No. Report No.: Internal reports Suez Environment, 2011.

[22] Cooper, N. B., Marshall, J. W., Hunt, K., Reidy, J. G. J. W. e., technology. Less power, great performance, 2007, 19: 63-66.

[23] Omoike, A. J. W. R. Removal of phosphorus and organic matter removal by alum during wastewater treatment, 1999, 33: 3617-3627.

[24] Jarvis, L. J. C. M. R. PAC Faces Renewed Pressure From Tight Supplies, Rising Costs. 2000, 257: 29-29.

[25] Ouellette, J. J. C. M. R. Coagulants and flocculants rise, 1996, 250, SR18-SR18.

[26] Menezes, J., Silva, R., Arce, I., Schneider, I. J. M. E. Production of a poly-alumino-iron sulphate coagulant by chemical precipitation of a coal mining acid drainage, 2010, 23: 249-251.

[27] Kaksonen, A. H., Puhakka, J. J. E. i. L. S. Sulfate reduction based bioprocesses for the treatment of acid mine drainage and the recovery of metals, 2007, 7: 541-564.

[28] Roetman, E. T. The sterilization of sewage by acid mine water. West Virginia University, 1932.

[29] Joseph, J. M., Shay, D. E. J. A. J. o. P. H.; Health, t. N. Viability of Escherichia coli in acid mine waters,

DOI: https://doi.org/10.30564/hsme.v2i2.2448

1952, 42: 795-800.

[30] Rogers, T. O., Wilson, H. J. J. PH as a selecting mechanism of the microbial flora in wastewater-polluted acid mine drainage, 1966: 990-995.

[31] Eaton, A. D., Clesceri, L. S., Greenberg, A. E., Franson, M. A. H. Standard methods for the examination of water and wastewater. American public health association, 2005, 21: 1600.

[32] Kumar, N., Omoregie, E. O., Rose, J., Masion, A., Lloyd, J. R., Diels, L., Bastiaens, L. J. W. R. Inhibition of sulfate reducing bacteria in aquifer sediment by iron nanoparticles. 2014, 51: 64-72.

[33] Deng, D., Lin, L.-S. J. W. r. Continuous sulfidogenic wastewater treatment with iron sulfide sludge oxidation and recycle. 2017, 114: 210-217.

[34] Deng, D., Weidhaas, J. L., Lin, L.-S. J. J. o. H. m. Kinetics and microbial ecology of batch sulfidogenic bioreactors for co-treatment of municipal wastewater and acid mine drainage. 2016, 305: 200-208.

[35] Dar, S. A., Bijmans, M. F., Dinkla, I. J., Geurkink, B., Lens, P. N., Dopson, M. J. M. e. Population dynamics of a single-stage sulfidogenic bioreactor treating synthetic zinc-containing waste streams. 2009, 58: 529.

[36] Younger, P. L., Banwart, S. A., Hedin, R. S. Mine water: hydrology, pollution, remediation. Springer Science & Business Media, 2002.

[37] Kadlec, R., Wallace, S. J. B. R., London, New York. Treatment wetlands. CRC Press Taylor & Francis Group. 2009: 267-347.

 DOI: https://doi.org/10.30564/hsme.v2i2.2448

About the Publisher

Bilingual Publishing Co. (BPC) is an international publisher of online, open access and scholarly peer-reviewed journals covering a wide range of academic disciplines including science, technology, medicine, engineering, education and social science. Reflecting the latest research from a broad sweep of subjects, our content is accessible world-wide——both in print and online.

BPC aims to provide an analytics as well as platform for information exchange and discussion that help organizations and professionals in advancing society for the betterment of mankind. BPC hopes to be indexed by well-known databases in order to expand its reach to the science community, and eventually grow to be a reputable publisher recognized by scholars and researchers around the world.

BPC adopts the Open Journal Systems, see on ojs.bilpublishing.com

Database Inclusion

Asia & Pacific Science Citation Index

Creative Commons

China National Knowledge Infrastructure

Google Scholar

Crossref

MyScienceWork

BILINGUAL
PUBLISHING CO.
Pioneer of Global Academics Since 1984

Tel:+65 65881289
E-mail:contact@bilpublishing.com
Website:www.bilpublishing.com

ISSN 2661-331X
02
9 772661 331205
Price: S$30.00